ISSN en trámite

Geofísica Internacional

Revista Trimestral Publicada por el Instituto de Geofísica de la Universidad Nacional Autónoma de México

México
Volume 59 Number 4
October - December
2020

— Geofísica Internacional —

GEOFÍSICA INTERNACIONAL, Año 59, Vol. 59, Núm. 4, octubre - diciembre de 2020 es una publicación trimestral, editada por la Universidad Nacional Autónoma de México, Ciudad Universitaria, Alcaldía Coyoacán, C.P. 04150, Ciudad de México, a través del Instituto de Geofísica, Circuito de la Investigación Científica s/n, Ciudad Universitaria, Alcaldía Coyoacán, C.P. 04150, Ciudad de México, Tel. (55)56 22 41 15. URL: http://revistagi.geofisica.unam.mx, correo electrónico: revistagi@igeofisica.unam.mx. Editora responsable: Andrea Rostan Robledo. Certificado de Reserva de Derechos al uso Exclusivo del Título: 04-2022-081610251200-102, ISSN: en trámite, otorgados por el Instituto Nacional del Derecho de Autor (INDAUTOR). Responsable de la última actualización Saúl Armendáriz Sánchez, Editor Técnico. Fecha de la última modificación: 30 de septiembre 2020, Circuito de la Investigación Científica s/n, Ciudad Universitaria, Alcaldía Coyoacán, C.P. 04150, Ciudad de México.

Geofísica Internacional
Vol. 59, Núm. 4, octubre-diciembre de 2020

Contents

Original paper

Subsoil Characteristics of Mexico City, Aceleration and Hysteretic Energy Spectra for the Mexico Earthquake of September 19, 2017

Pablo Quinde*[1] and Eduardo Reinoso[1]

Received: August 31, 2019, accepted: July 1, 2020; online publication: October 1, 2020

Resumen

El terremoto intraplaca del 19 de septiembre de 2017 (Mw7.1), cuyo epicentro se localizó cerca de los límites entre los estados de Puebla y Morelos, aproximadamente a 120 km de Ciudad de México, causó daños severos en estas regiones. Este artículo analiza los cocientes espectrales de estaciones acelerométricas en el lecho lacustre de la Ciudad de México con respecto al espectro promedio de Fourier en sitios de la zona de suelo firme para estudiar y comparar los cambios, en el tiempo, con el comportamiento de los efectos de sitio y su relación con el daño presentado durante este terremoto; estas cocientes también exhiben el problema de asentamiento en algunos lugares de la ciudad debido a la sobreexplotación del acuífero para el suministro de agua, en donde se ha visto cambios en el periodo del suelo, inclusos cercanos al 40 por ciento. Finalmente, se presentan mapas de pseudoaceleración y energía histerética para la Ciudad de México con una discusión de una posible correlación con los daños reportados.

Palabras clave: cocientes espectrales, pseudoaceleración, energía histerética, espectro de Fourier, terremoto de México, amplificaciones espectrales.

Abstract

The September 19, 2017, intraslab earthquake (Mw7.1), whose epicenter was located near the limits between the states of Puebla and Morelos at approximately 120km from Mexico City, caused severe damage in these regions. This article analyzes the spectral ratios of accelerometric stations in the lake-bed of Mexico City with respect to the average Fourier spectra at hill zone sites in order to study and compare over time the changes in the behavior of local effects and their relationship with the damage presented during this earthquake. These ratios also exhibit the settlement problem in some places in the city due to overexploiting the aquifer for water supply purposes, where changes in soil periods, even larger than 40%, are seen. Finally, pseudoacceleration and hysteretic energy maps for Mexico City with a discussion with a possible correlation with reported damages are presented.

Key words: Spectra ratios, pseudoacceleration demands, hysteretic energy demands, Fourier spectra, Mexico earthquake, spectral amplifications.

*Pablo Quinde
PQuindeM@iingen.unam.mx

1Instituto de Ingeniería de la Universidad Nacional Autónoma de México, Cd. Universitaria, Coyoacán, CP: 04510, México

INTRODUCTION

Mexico is located in the so-called Pacific Fire Belt, so the main source of seismic hazard is associated with the interslab earthquakes located in the subduction zone formed by Cocos and North-American plates. Mexico City is more than 300 km away from the subduction zone. Despite this, historically, the damage caused by interslab earthquakes is considerable, mainly because the local soil effects yield significant amplification in a large part of the city. These local effects are because a large area of Mexico City is located over the ancient Texcoco, Xochimilco and Tlahuac lakes. The September 19, 1985 earthquake (Mw8.1), whose epicenter was 315km away, is the leading example of this type of subduction earthquakes.

Normal fault earthquakes, with depths between 40 to 80km, are also crucial for the seismicity in Mexico City, especially for lakebed zones with dominant soil periods between 1.0 and 1.8s (S. K. Singh *et al.* 2018). The September 19, 2017, intraslab earthquake (Mw7.1), whose epicenter was located near the limits between the states of Puebla and Morelos at approximately 120km from Mexico City, caused severe damage in Mexico City, Morelos, Puebla and the State of Mexico. In Mexico City, more than 40 collapsed buildings were reported, and hundreds had moderate and severe damage. The intensities reordered in some areas of the city, especially in zones with periods between 0.5s and 1.8s, were relatively high, even surpassing values of 1.0g, and the vertical component, due to the proximity of the earthquake, was unusually high for Mexico City.

The main seismic problem of Mexico City is the large amplification that occurs due to the clay deposits of the ancient Texcoco Lake. Singh *et al.*, 1988 and Reinoso, 1991 reported spectral amplifications close to 500 times to what typical strong ground motion equations predict at similar epicentral distances. The site effects of the lakebed zone of the city strongly modify the seismic responses of the soil, which may vary considerably within a few hundred meters.

There are several proposals to estimate the site effects of the Valley of Mexico. Some authors such as Pérez-Rocha et al. 1991, Reinoso *et al.* 1997, Baena-Rivera *et al.* 2017 and Cruz-Atienza *et al.* 2016 used numerical implementations to analyze the wave propagation within basins.. Other works are based on the use of data from weak motion to study the vibrating soil period (Ordaz *et al.* 1988, Lermo and Chavez-Garcia 1994), combined methodologies through Bayesian models (Perez-Rocha 1998) or using Fourier spectral ratios to compute the lakebed amplifications with respect to the hill zone (Reinoso and Ordaz 1999).

Mexico City is one of the largest and most populated cities in the world, which house approximately 20 million people. One of the main problems to deal with is the water supply, around 60m3/s a day, of which more than 60% (≈40m3/s) is extracted from underground aquifers located below the city (Arroyo *et al.* 2013). There is a recharge problem because, annually, only 75% of these aquifers are replenished naturally. This intensive water pumping has contributed to the consolidation of the soft soils of the Valley of Mexico, causing exceptional levels of subsidence of the soil and changing the characteristics of the soil and its response to earthquakes.

This article analyzes the spectral ratios of accelerometric stations in the lakebed of Mexico City, with respect to the average Fourier spectrum at firm soil sites, so that changes in the behavior of local effects and their relationship with the damage presented during the earthquake of September 19, 2017, is discussed. Also, pseudoacceleration maps and the hysteretic energy demands that could be associated with the reported damages are presented and analyzed.

ACCELEROMETRIC STATIONS AND EARTHQUAKES

Figure 1 shows the 77 accelerometric stations of Mexico City analyzed in this study. A large portion of the Valley of Mexico is located over the ancient Texcoco Lake. The lakebed has a dominant soil period larger than 0.5s and even reaching periods over 5.0s near the international airport zone (stations 02 and 31).

The information and data of the accelerometric stations was obtained from the "Centro de Investigación y Registro Sísmico (CIRES)" and the Institute of Geophysics of the UNAM. The CIRES accelerometric network began in 1987, and has 80 devices, 66 accelerometers at surface registration stations, 6 accelerometers installed in two structures and 8 underground registration sensors. In this article, only records at surface stations were considered. These accelerometers record the information on a PCMCIA card with the capacity to store 34 minutes of data. They have adjustable pre-event memory to record up to 56 seconds before the earthquake and post-event up to 64 seconds after the moment when the earthquake acceleration is less than the selected trigger level (CIRES, n.d.).

Due to the wide range of soil periods, the lakebed zone can be characterized by the dominant period of the site, which can be seen in Figure 1. The zone with the period limit in 0.5s is called the Hill zone. Likewise, in the lakebed zone, the subsoil can reach periods ranging from 0.5s to even more than 5.0s in zones with very deep clay soil-layers.

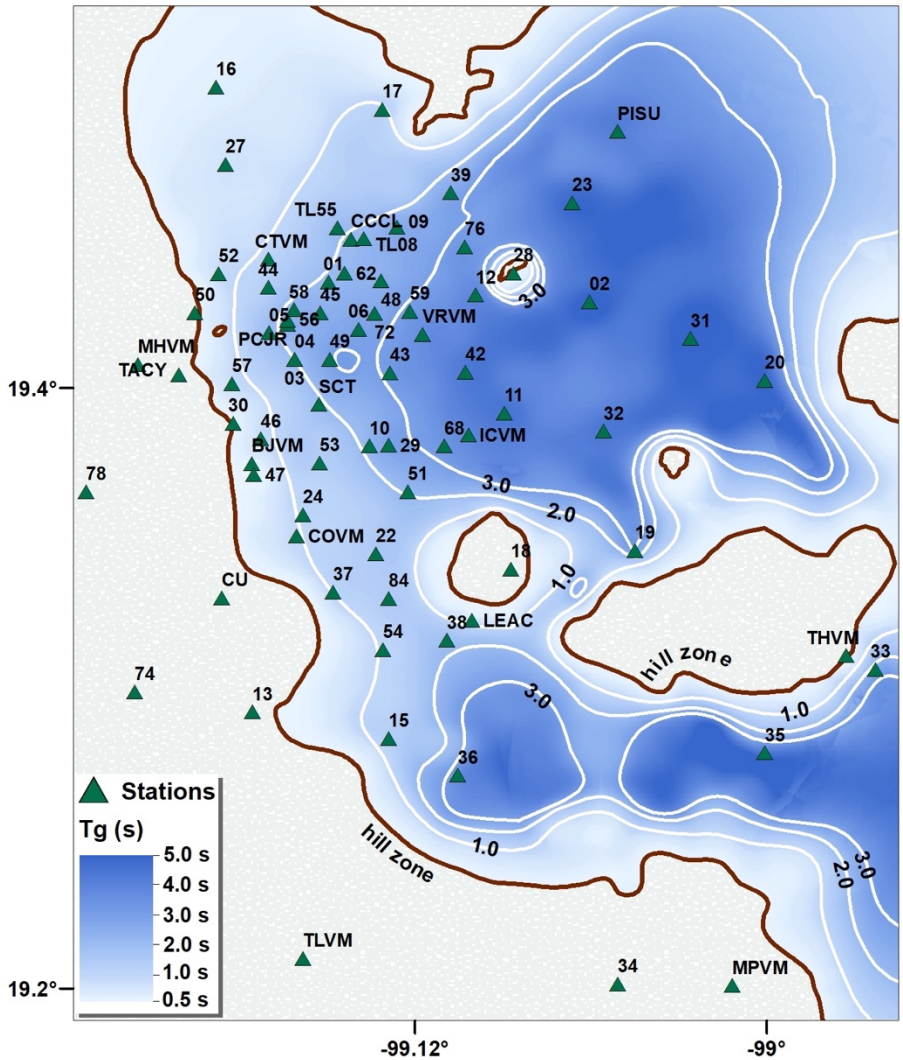

Figure 1. Accelerometric stations of Mexico City and soil dominant periods.

For this study, the seismic events reported in were used. These events correspond to the most representative earthquakes that occurred in Mexico since the Michoacán earthquake of 1985. The seismic network of the Valley of Mexico, before the September 19, 1985 earthquake, was very small, so the records used for this particular earthquake correspond only to stations CU01, TACY, and SCT.

Table 1. Earthquakes used in the study

ID	Event	Magnitude (M_w)	Fault type	Epicental distance (km)
E1	19/09/1985	8.0	Subduction	394
E2	25/04/1989	6.9	Subduction	303
E3	24/10/1993	6.6	Subduction	299
E4	10/12/1994	6.4	Subduction	288
E5	23/05/1994	6.2	Normal	206
E6	14/09/1995	7.3	Subduction	320
E7	15/06/1999	6.9	Normal	218
E8	21/06/1999	6.3	Normal	295
E9	30/09/1999	7.4	Subduction	420
E10	21/07/2000	5.8	Normal	136
E11	22/05/2009	5.6	Subduction	157
E12	20/03/2012	7.4	Subduction	335
E13	19/09/2017	7.1	Normal	130

The epicenters of the events mentioned in are shown in Figure 2.

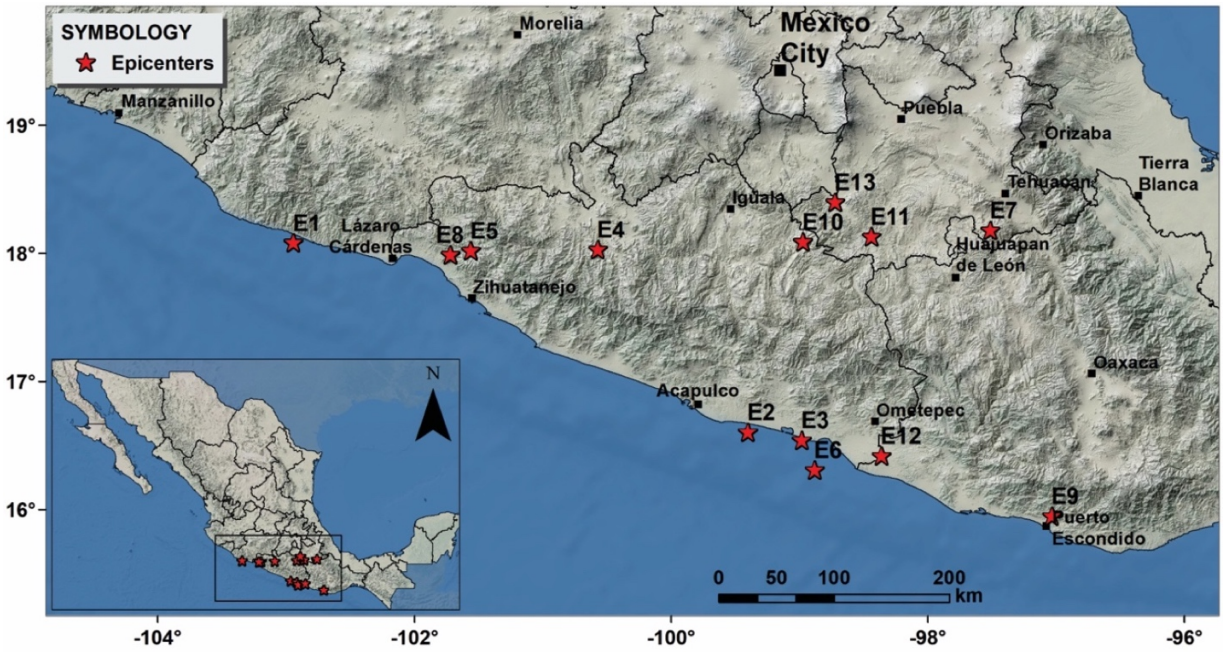

Figure 2. Earthquakes location.

SITE AMPLIFICATIONS USING FOURIER SPECTRAL RATIOS

There are several ways of obtaining the site amplification (Field, *et al.*; Sakaff, 1991, Reinoso and Ordaz 1999), some of which use inversion techniques (E. H. Field and Jacob 1995) although this type of techniques is does not work for the Mexico City valley (Gutiérrez and Singh 1992). Due to the almost linear behavior of the lakebed sites in Mexico City, the technique used in this article is the Fourier spectral ratios, which has been used in soft soils such as those in Mexico City with favorable results (Shri Krishna Singh *et al.* 1988) (Reinoso and Ordaz 1999). The Fourier spectral rates presented in this section help us to understand the dominant period and amplification of the soil, as well as their variation over time

1 HILL ZONE AMPLITUDE FOURIER SPECTRA

Site response using spectral ratios for only one hill zone site should be avoided (E. Field, *et al.*, 1992) because minor differences among hill zone sites could yield significant lakebed amplifications challenging to explain in terms of physical reasons. As Reinoso and Ordaz (1999) suggested, an average Fourier spectrum for hill-zone stations must be used. Likewise, in the same article there is a discussion of the smoothing of the Fourier spectra and recommendations for their use for spectral quotient purposes. Figure 3 shows, with grey lines, the smoothed amplitude Fourier spectra of hill zone accelerometric stations for different earthquakes and, with a dark line, the mean spectra of the EW component. As shown in Figure 3, amplitude differences are relatively small, but there are peak values, due to very local site conditions, that can affect the spectral ratios, so using the average spectra softens the hill zone response and, therefore, the spectral ratio. The stations chosen to compute the hill zone mean spectra (Reinoso and Ordaz 1999) are those which are located in the South-West zone of Mexico City: 78, 74, 50, 34, 07, 13, TACY and CU (Figure 1)

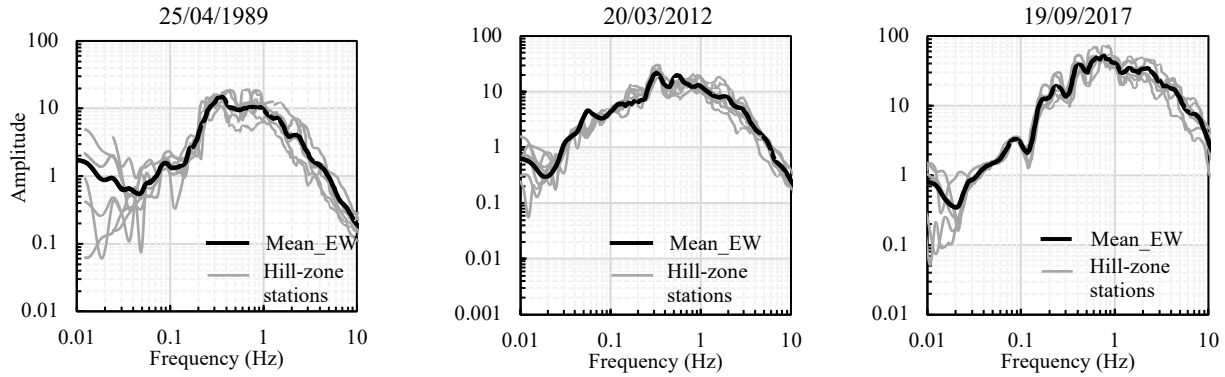

a) interslab earthquake b) interslab earthquake c) intraslab earthquake

Figure 3. Smoothed amplitude Fourier spectra of hill zone accelerometric stations for different earthquakes and mean Fourier amplitude spectra at hill zone

Figure 4 shows the average Fourier spectra for hill zone stations and all thirteen earthquakes presented in Table 1. Two groups of seismic events that follow similar behavior are noticed: interslab and intraslab earthquakes, shown in Figure 4a and Figure 4b, respectively. Figure 4c shows a comparison of the two most important and intense earthquakes of each kind; both occurred in September 19, the inslab one in 1985, and the intraslab one in 2017. Both earthquakes show different amplitudes, the 19/09/2017 earthquake presents peak values for frequencies larger than 1.0 Hz, while the 09/19/1985 one shows larger amplitudes for frequencies smaller than 1.0 Hz.

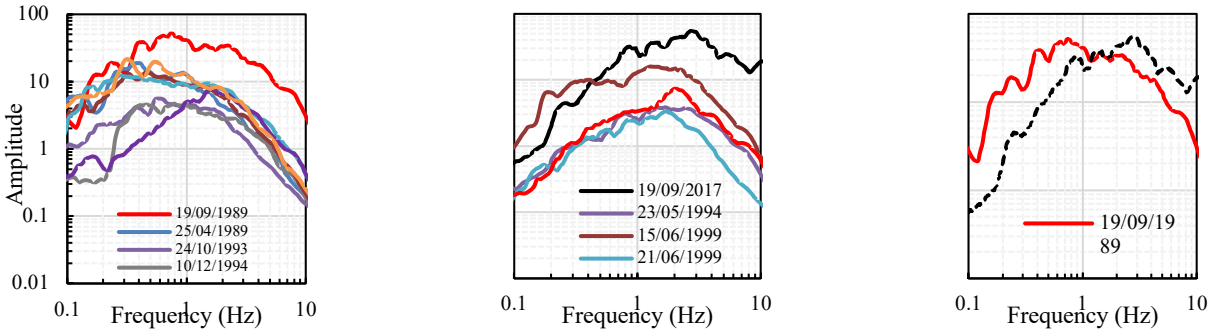

a) interslab earthquakes b) intraslab earthquakes c) Comaprison between 1985 and 2017 earthquakes

Figure 4. Average Fourier spectra for hill zone accelerometric stations and for the thirteen events reported in Table 1 (EW direction): a) Interslab earthquakes, b) intraslab earthquakes and c) comparison between average Fourier spectra of both events occurred in September 19 (1985, inslab, and 2017, intraslab).

2 LAKEBED ZONE SPECTRAL RATIOS

Mexico City has some of the most pronounced site effects known. For some frequencies, the amplification can be up 500 times to epicentral sites, and up to 100 times the observed at hill zone. As stated by Ordaz *et al.* 1988, Singh *et al.* 1988 and Reinoso and Ordaz 1999, the lakebed zone soil responds approximately as the one-dimensional theory predicts, however, there are some sites where evidence of 2D or 3D behavior, or at least a non 1D one has been captured by spectral ratios (Reinoso and Ordaz 1999). Spectral ratios have been computed since the 1985 earthquake and have shown to be relatively constant for different sources, epicentral distances, and magnitudes. The spectral ratios theoretically remove most of the effects from the source and path, and only leaves the site effect. However, there is evidence that in recent years, the soft-soil response in some regions of the lakebed zone has changed, mostly due to anthropogenic conditions, in particular, ground subsidence produced by groundwater withdrawal (Avilés and Pérez-Rocha 2010, Arroyo *et al.* 2013).

In order to present the main changes and observations, we have selected five accelerometric stations that are considered as representative of the site amplification: SCT, 37, 12, 20, and 84. The Fourier spectral ratios were computed for each one of these stations, considering the mean spectrum for the hill zone, as explained above.

STATION SCT

This site is located where severe damage was observed during both September 19 earthquakes. Accelerometric data obtained in station SCT is extremely valuable to study site effects due to clay deposits shows the 1D model for station SCT and the spectral ratios computed for this site, for ten events, and both orthogonal directions. As shown in this figure, the amplification pattern between both orthogonal components is similar (with the exception of 25/04/1989 earthquake) with a peak amplitude between 10 and 15 times. The peak amplitude almost matches the predicted by the 1D theory; however, there are differences in amplitudes among periods longer and shorter than the dominant soil period. Its behavior remains similar to that reported by Reinoso and Ordaz 1999.

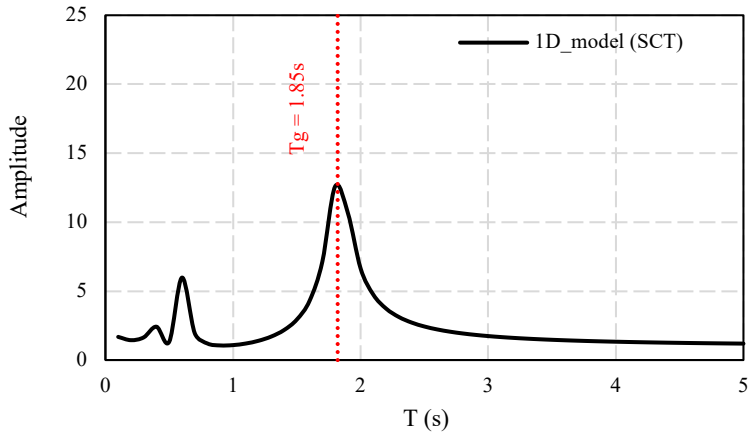

Figure 5. Amplitude for 1D model of station SCT

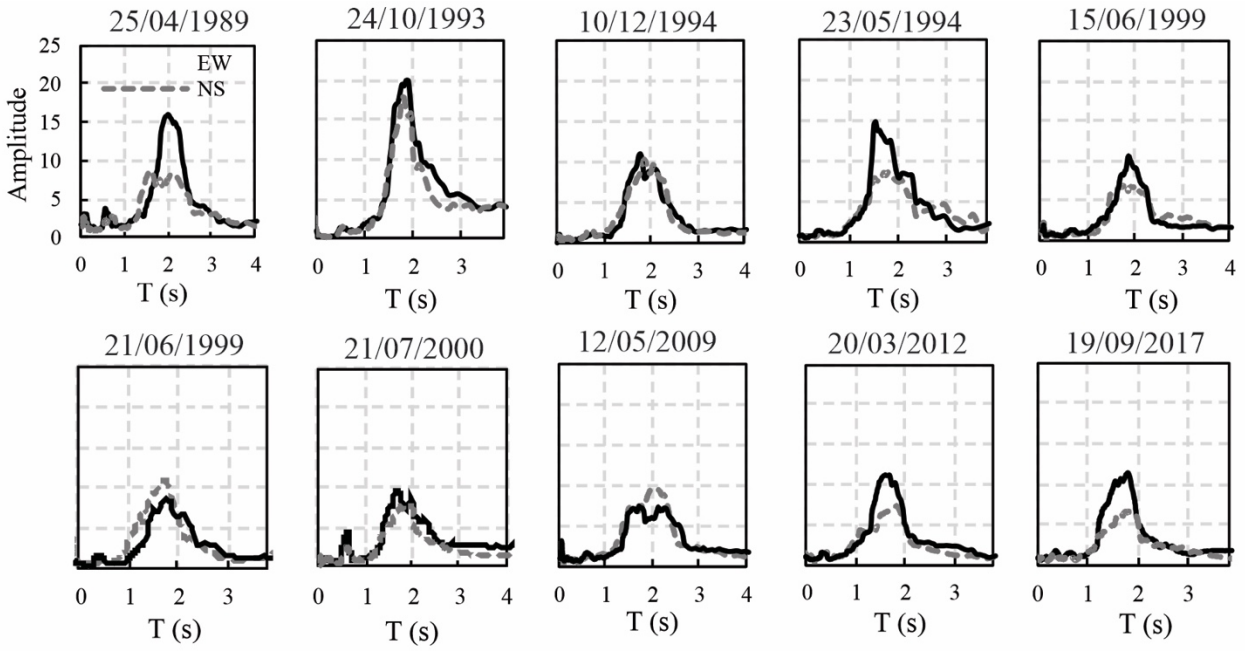

Figure 6. Spectral ratios for SCT station

STATION 37

This site is over the less thick soil deposits, also known as transition zone, with peak amplification between 5 and 10 for a site period of 1s. This station represents all stations located in similar lakebed zone sites where amplification has been very similar for all earthquakes, and no significant variation of spectral ratios (amplification and dominant period) has been observed due to epicentral distance, magnitude or fault type. This station is located in a highly-populated area where damage was severe during the September 19, 2017 earthquake. Figure 7 shows the spectral ratios computed for this site, for nine events and both orthogonal components of motion.

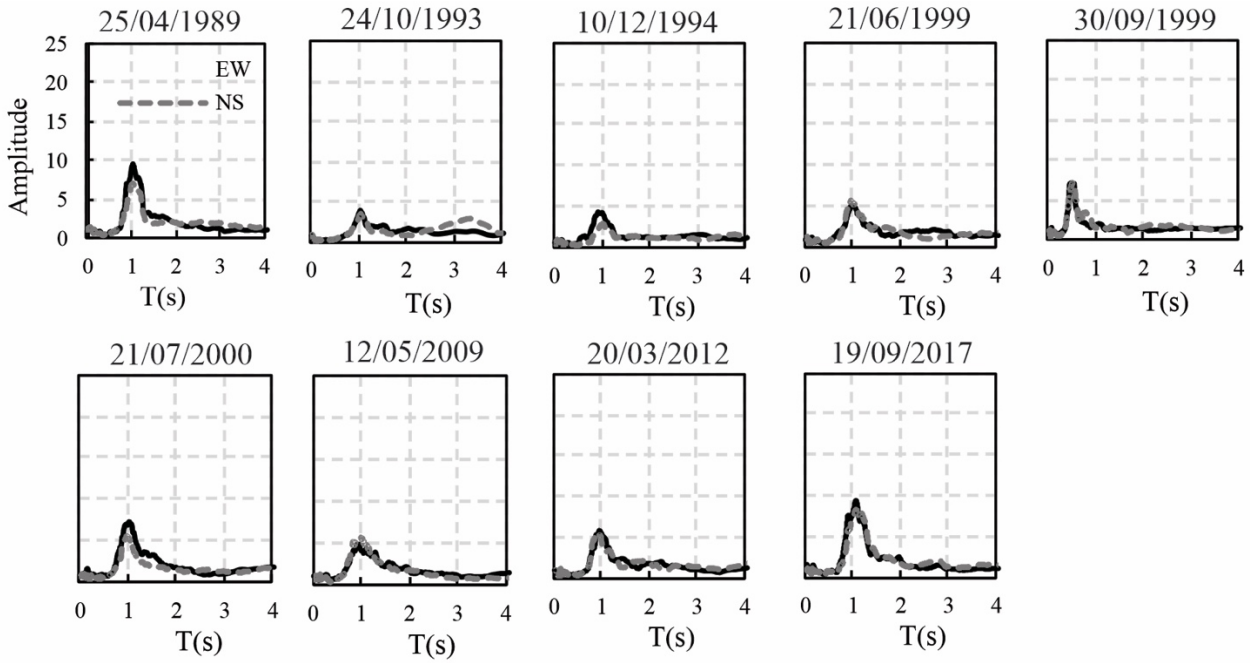

Figure 7. Spectral ratios for station 37.

STATION 12

This site is located in a zone with clay deposits 40-50m deep, next to a hill zone near the Mexico City airport. Very little damage was reported there during both September 19 earthquakes.

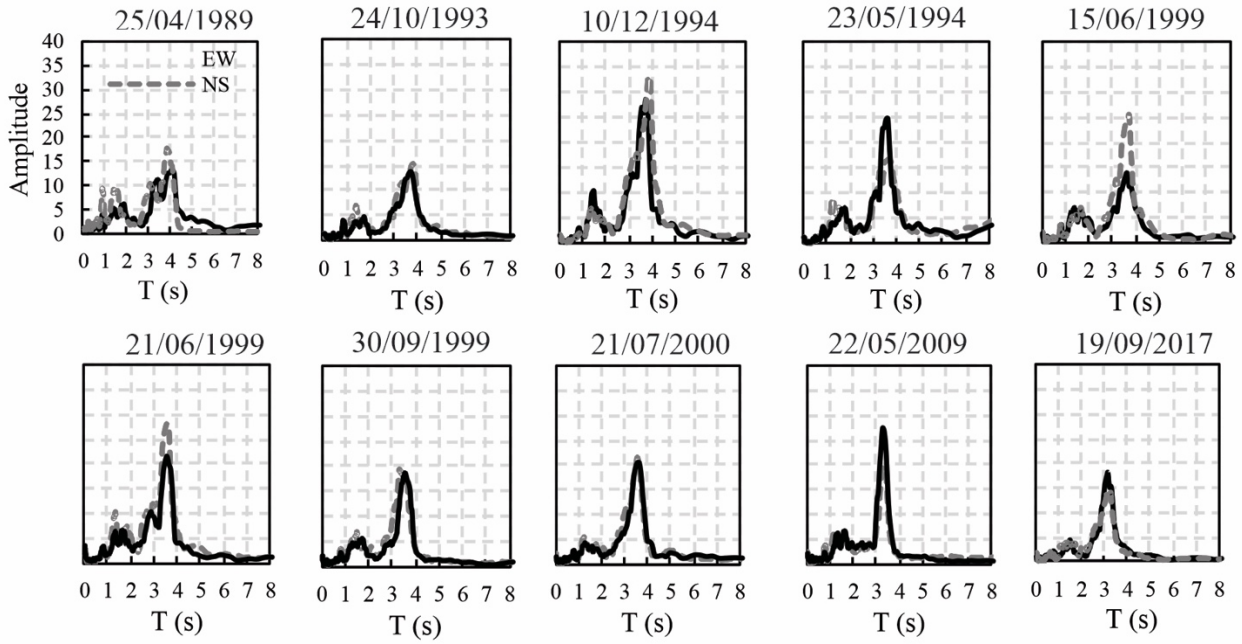

Figure 8. Spectral ratios for station 12.

Figure 8 shows the spectral ratios computed for this site, for ten events, and both horizontal components. The amplitude of the NS direction shows more considerable amplification for the 15/06/1999, 10/12/1994, and 21/06/1999 earthquakes, reaching amplitudes differences up to 80%.

These differences may be caused by basin-edge effects due to its proximity to a hill zone. On the other hand, apart from differences in amplitude, a decrease in the dominant soil period close to 25% can be observed, with values from 4.10s measured during the 1989 event, to 3.15s, during the 2017, one. This variation will be discussed later in this work.

STATION 20

This site is over the deepest soil deposits of the ancient Texcoco Lake. No damage has been reported around this station after any earthquake since few structures could vibrate with the very large dominant periods of this site; however, second to third vibration modes of the site, with periods around 1s, may present amplifications up to 10 times, similar to those observed at other lakebed zone sites where damage and even collapses were reported. Figure 9 shows the spectral ratios computed for this site, for nine events, and for both orthogonal directions. We observe that amplifications are up to 40 times the hill-zone response and that there is a complex amplification pattern. Similar to station 12, the decrease in the dominant soil period for this station along 28 years is about 12%, with values ranging from 4.8s during the 1989 event, to 4.25s, for 2017 one.

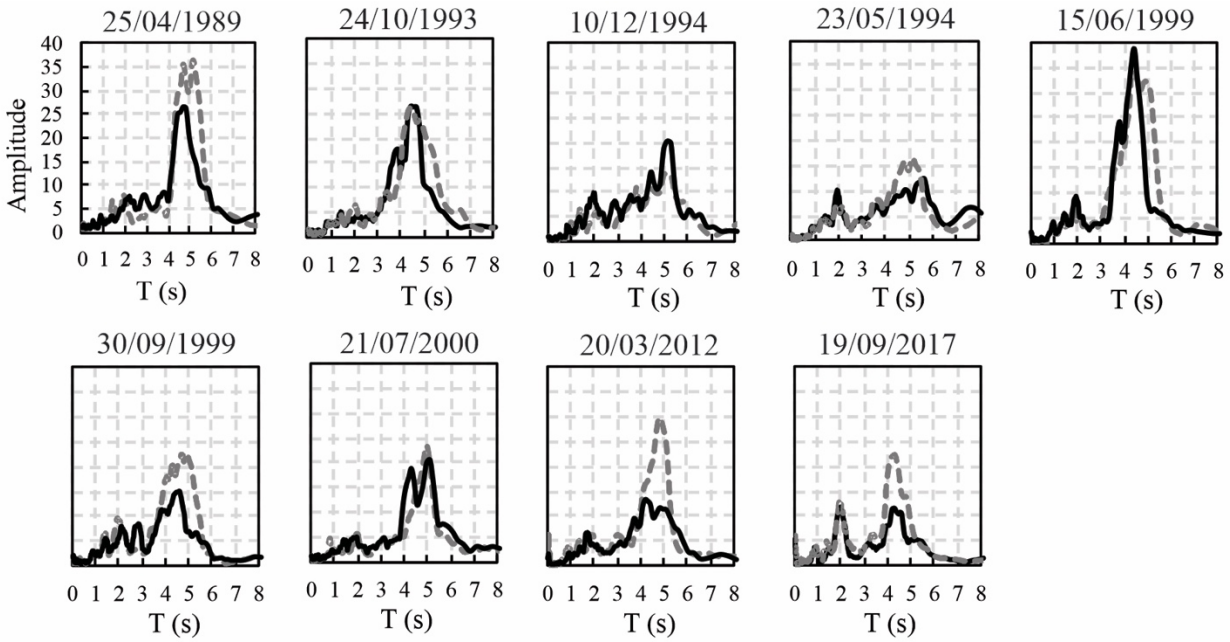

Figure 9. Spectral ratios for station 20 station

STATION 84

This site is also located in a dense residential area, between two relatively close (5-6 km) hill zones (see Figure 1): the "Cerro de la Estrella" and the western hill zone. During the September 19, 2017 earthquake, this station recorded the highest intensity in the history of the Mexico City accelerometric network. Table 2 shows the accelerometric stations that have recorded the largest PGA in Mexico City during the last 40 years and the ten most intense computed peak spectral acceleration for some of the earthquakes of Table 1 (and Figure 2) and other historical ones.

Table 2. Largest intensities recorded in the Mexico City accelerometric network; station 84 shows the maximum values during the September 19, 2017 earthquake

Event	Station	Tg	PGA (cm/s^2)	Peak spectral acceleration (cm/s^2)
19/09/2017	84	1.4	227.9	1531.2
19/09/1985	SCT	1.9	121.4	912.5
14/09/1995	35	5	66.68	314.5
20/03/2012	35	5	62.61	404.4
25/04/1989	35	5	62.54	316.7
14/03/1979	TXSO	0.6	53.37	289.5
24/10/1980	SXVI	0.5	46.6	120.6
30/09/1999	35	5	43.18	184.2
15/06/1999	36	3.6	40.92	180.3
22/05/2009	54	1.1	33	82.9

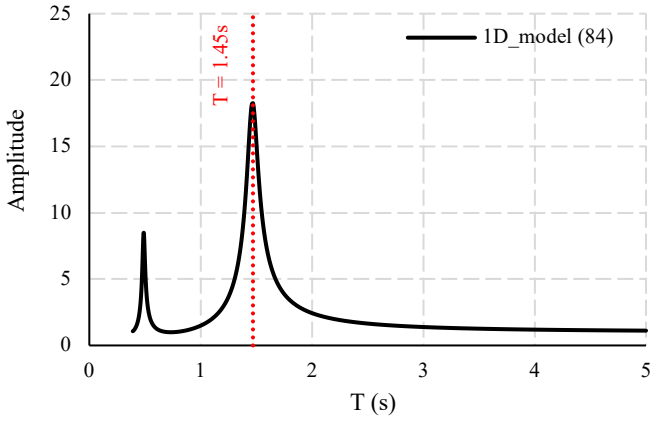

Figure 10. Amplitude for 1D model of station 84.

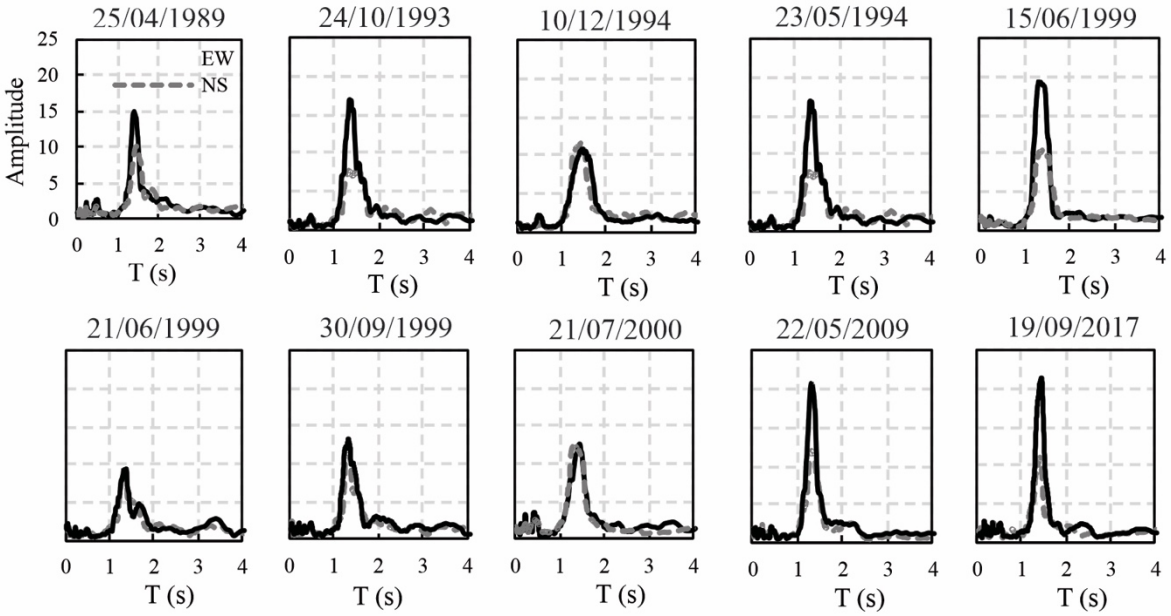

Figure 11. Spectral ratios for station 84.

The proximity of station 84 to the hill "Cerro de la Estrella" and western lakebed borders suggests an amplification pattern that cannot be explained by the 1D theory. Reinoso and Ordaz 1999 have reported observations of 3D amplification patterns for other sites in the lakebed zone. Figure 10 shows the 1D model for station 84 and Figure 11 the spectral ratios computed for this site, for ten events and for both orthogonal components, where it can be seen that the amplitudes for the NS direction remain relatively constant regardless of the earthquake. However, the NS direction shows an amplification pattern that is very different from those predicted by the one-dimensional model. Higher amplifications were computed for intraslab events 23/05/1994, 15/06/1999, 22/05/2009, and 19/09/2017. The amplification change, only observed in the EW direction, could be due to basin-edge effects (Reinoso and Ordaz 1999).

To analyze this behavior, an attempt has been made to correlate parameters, such as azimuth, magnitude and fault mechanism. However, the strongest correlation that was found is the following. Figure 12 shows the peak amplitude at the dominant period of site 84 (T=1.4 s) and the hypocentral distance of the earthquake, together with the expected amplification value given by a 1D model considering rough information of the site (dashed line). Figure 12 shows the variation of the amplitude to the hypocentral distance of different interslab and intraslab earthquakes. Figure 12a shows that the computed amplitude for the NS direction is very similar and around the prediction by the 1D theory. Moreover, Figure 12b shows, for the EW direction, a trend that can be correlated with the hypocentral distance showing twice

the amplification for shorter distances. Whatever the type of site effect, it is something that it is present only with close events and has only been observed for this station.

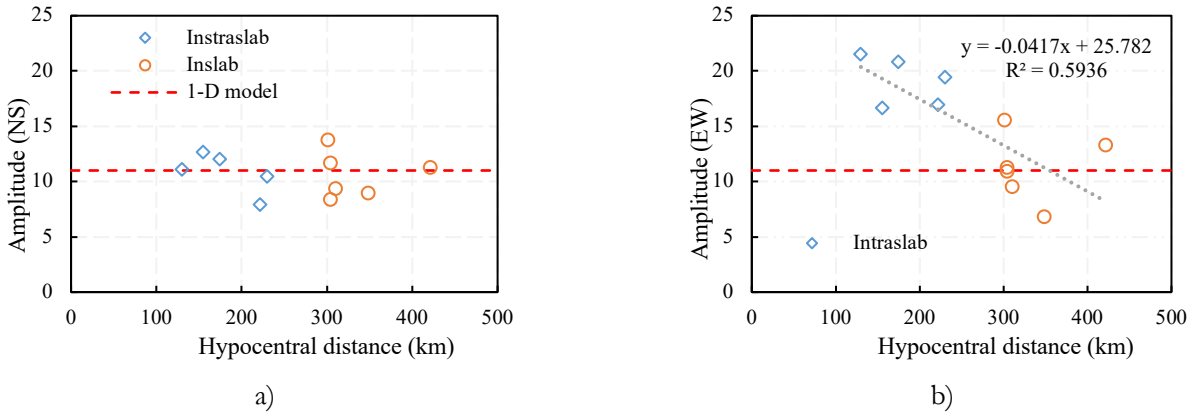

Figure 12. Correlation between peak amplitude with hypocentral distance: a) NS direction and b) EW direction. Dashed line represents the one-dimensional amplitude.

3 SOIL DOMINANT VIBRATION PERIOD BEHAVIOR

Estimating the soil vibration period (Tg) with the smallest uncertainty is important since it is directly correlated to the seismic response of structures. The Mexico City Building Code takes this into account as the design spectra are based on Tg. The code contains a very detailed map of Tg, built a few years ago with information from spectral ratios, geotechnical studies, and weak motions. However, some evidence proves that this Tg has changed over time (Avilés and Pérez-Rocha 2010, Arroyo *et al.* 2013). The variation of Tg was examined for all earthquakes of Table 1 and Figure 2, and all accelerometric stations of the lake-bed zone (Figure 1). Figure 13 shows for the most representative twenty-five accelerometric stations the variation of the dominant soil period as a function of time, with an open circle, and the corresponding trend with dotted-line. It can be seen that there are sites with a clear trend of shortening the soil period over time. The rates of period-change vary from site to site being almost null for some stations, to up to 20% for others.

A map with the dominant soil period decreases is shown in Figure 14. This figure shows the decrease (in percentage) of the dominant soil periods between those computed during the April 25, 1989, and September 19, 2017 earthquakes, using the spectral ratios shown in this article. The results shown in Figure 14 do not correspond to any approximate model and are based on real data and earthquakes recorded by the accelerometric network of Mexico City. However, it should be considered that results could have minor changes if a special interpolation were used, similar to those proposed by Perez-Rocha (1998) and Worden *et al.* (2018).

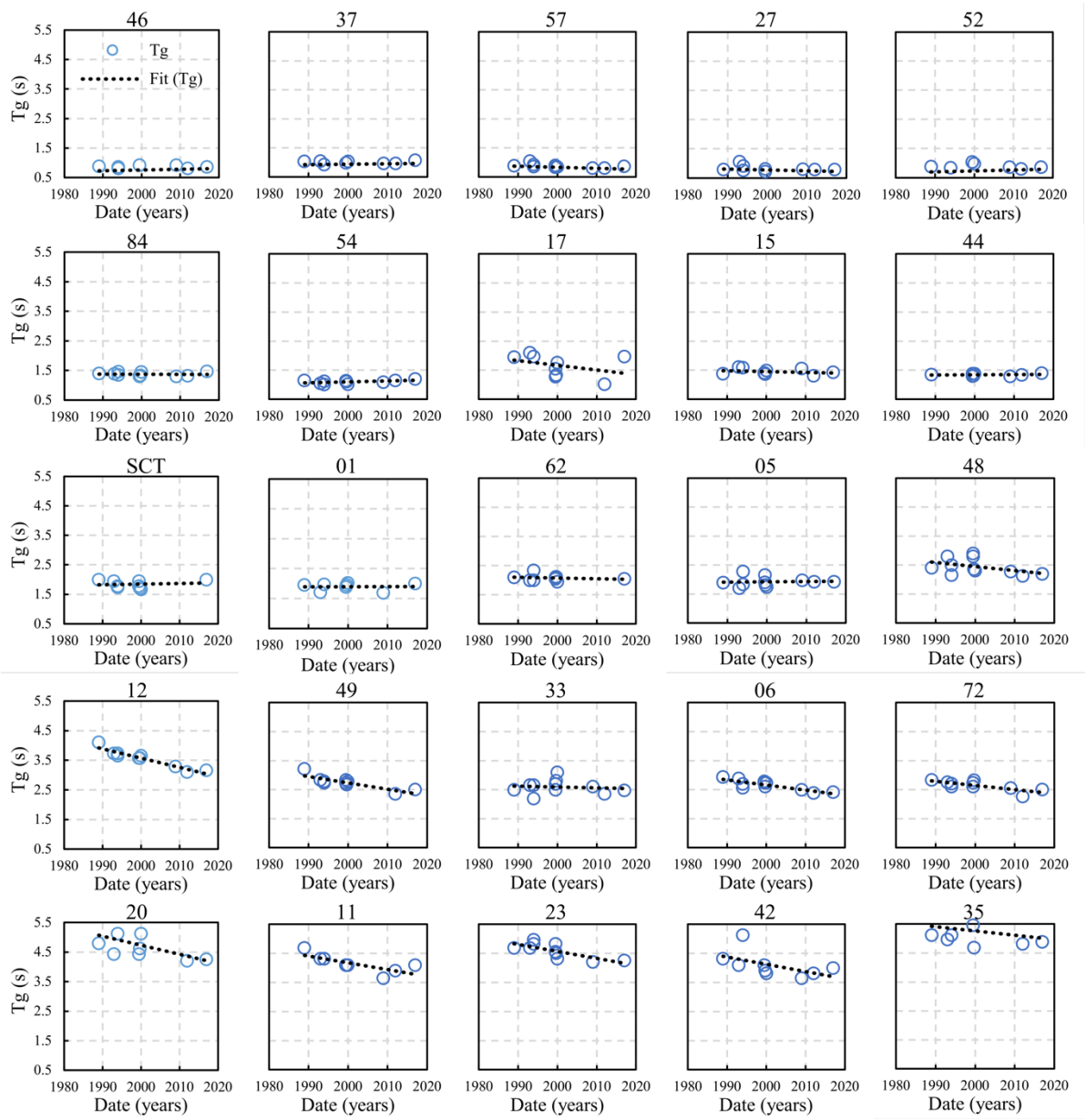

Figure 13. Variation of the soil dominant period over time for 25 selected accelerometric stations in Mexico City

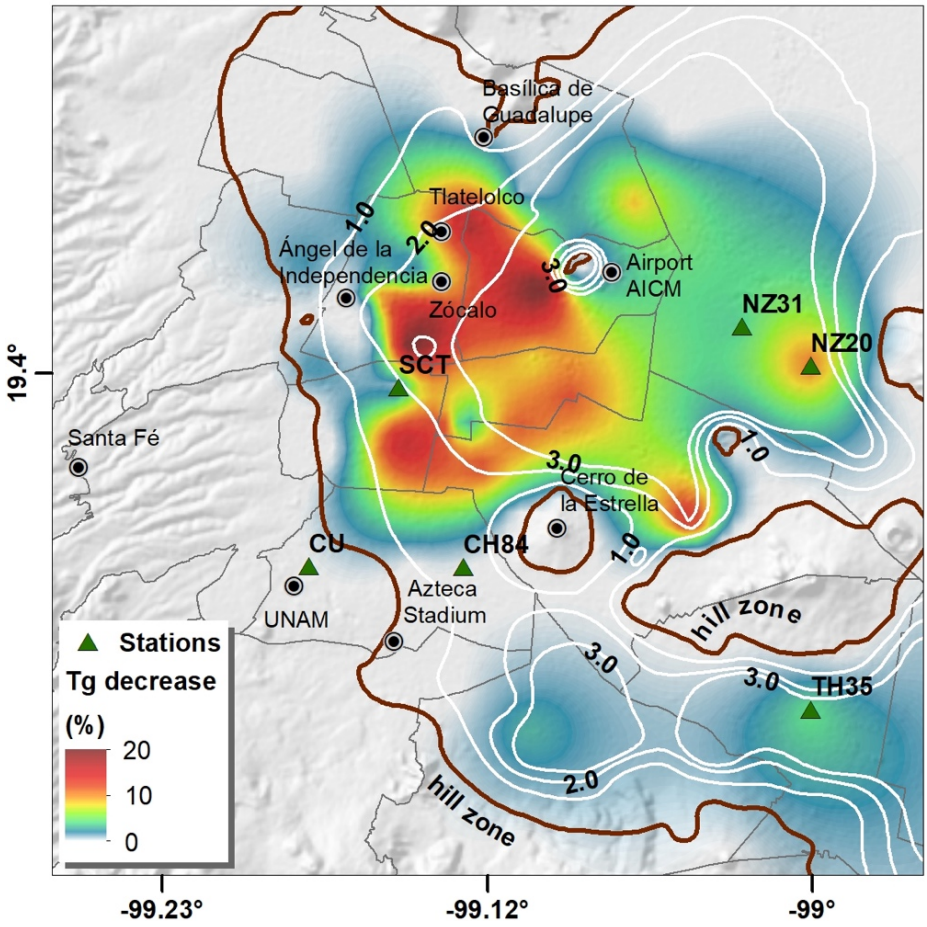

Figure 14. Decrease in percent of soil dominant periods in the lake area of Mexico City

4 Fourier spectral amplifications

A similar analysis was performed for the maximum spectral amplification of each station at the lakebed zone. That is, if, according to the previous section, the dominant period at a given station changed, maximum amplification is the observed for this changed period. Figure 15 shows the time-variations maximum spectral amplitude for 25 accelerometric stations. This amplification is the maximum computed in the spectral ratio, no matter at which period, for each station and earthquake, and both orthogonal components (EW amplification, open circles, NS component, filled triangles); trends are plotted with dotted lines. The observed variations as a function of time are different for both orthogonal components, and no overall trend is observed.

In most cases, the amplitude has decreased over time, however stations 37 (NS), 84 (EW), 15 (EW) and 12 (NS) show an increase in their amplitude. Similar to what was observed above about station 84, stations 37 and 15 are located very close to it (Figure 1), so similar conclusions of 3D effects could explain this amplification. However, station 54, also within the area, does not exhibit any amplification over time. Station 12 has been one of the most affected by the settlement of the city, and it is also located very close to a hill zone so that similar 3D effects could be present there.

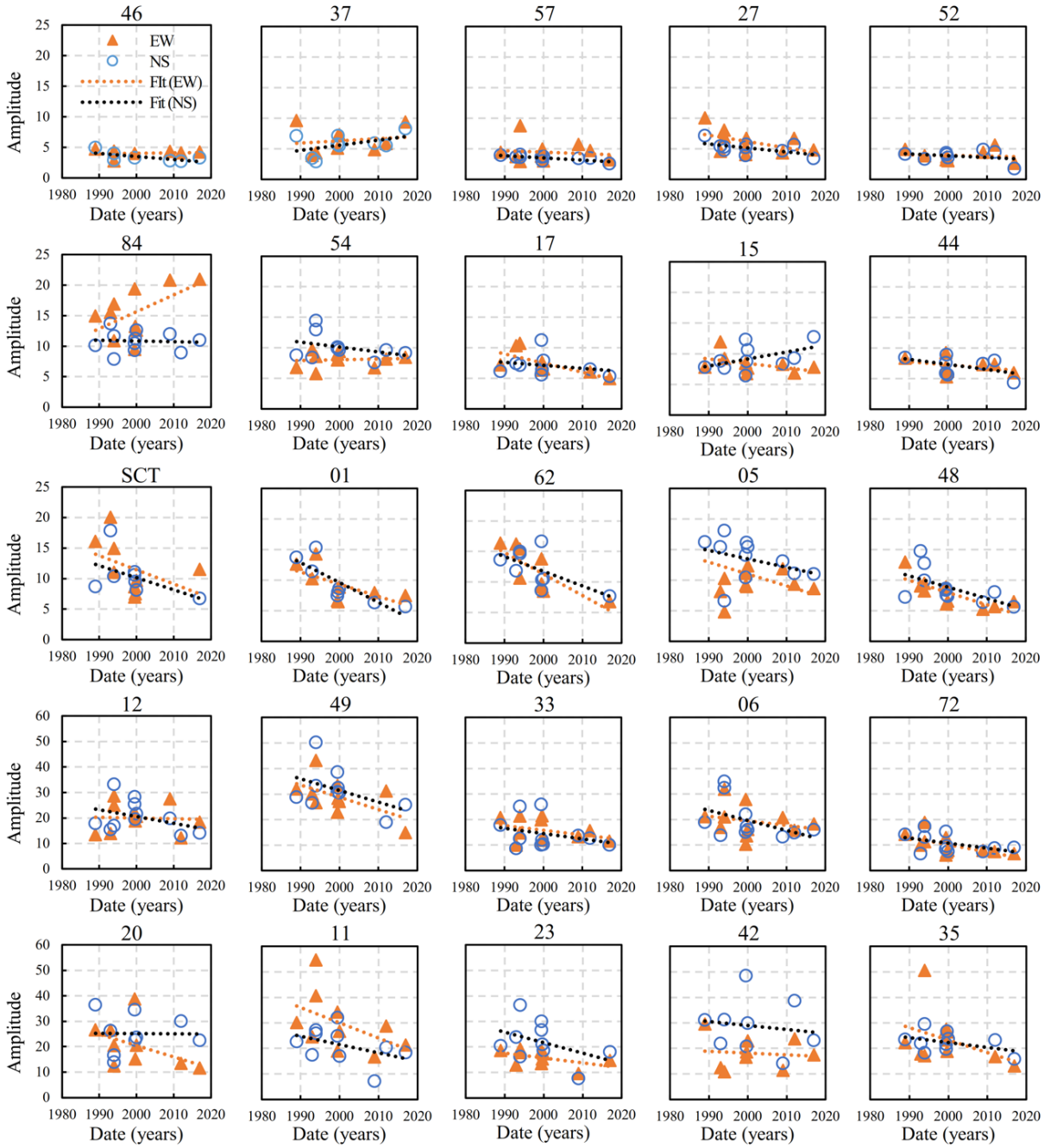

Figure 15. Fourier spectral maximum amplitude for several accelerometric stations and for both orthogonal directions

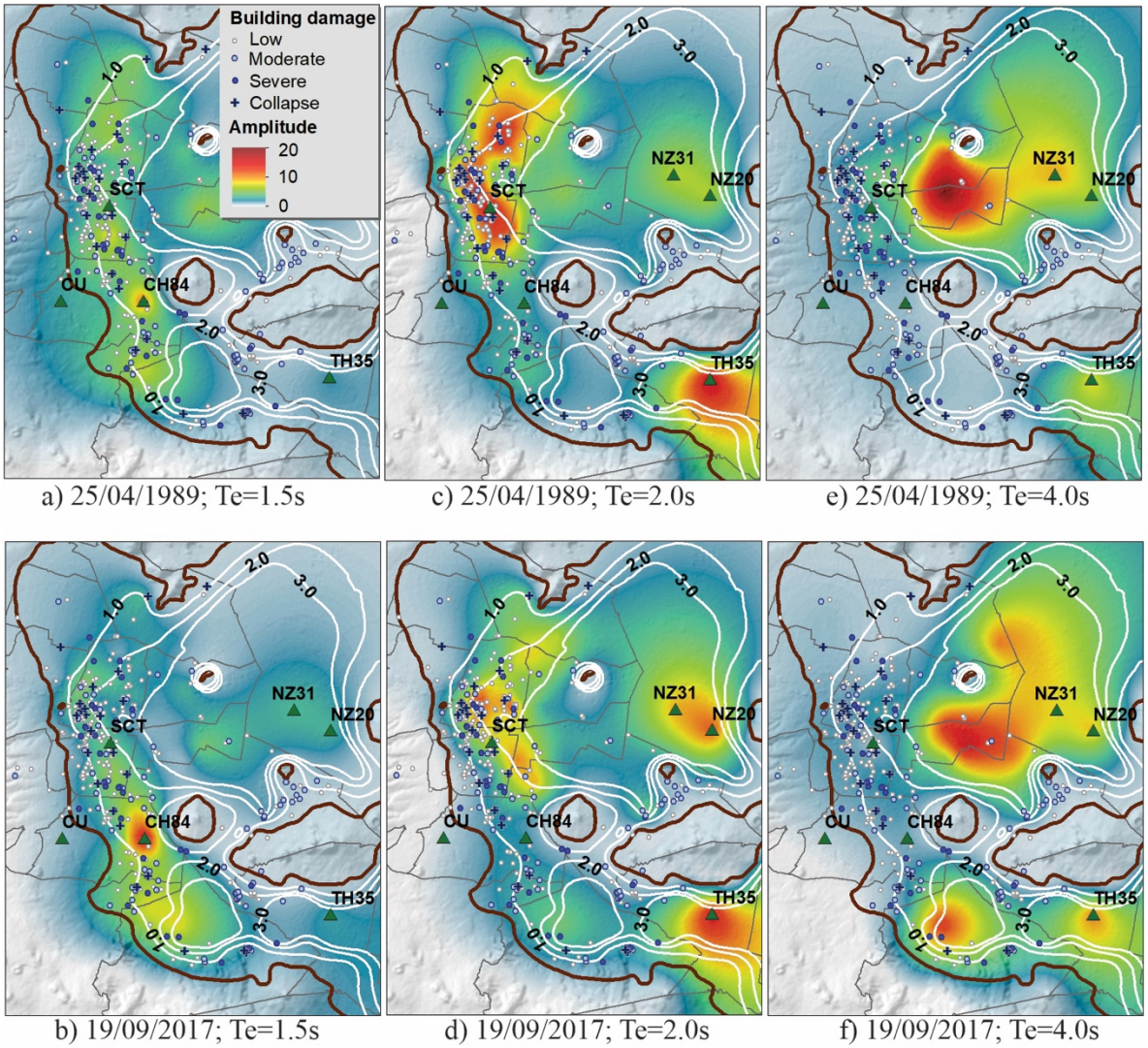

Figure 16. Maximum spectral amplification maps for the EW direction. a) 25/04/1989 and Te=1.5s, b) 19/09/2017 and Te=1.5s, c) 25/04/1989 and Te=2.0s, d) 19/09/2017 and Te=2.0s, e) 25/04/1989 and Te=4.0s, f) 19/09/2017 and Te=4.0s.

Figure 16 shows the maximum amplification maps for the EW component of April 25, 1989 (top row), and the September 19, 2017 (bottom row) earthquakes. The amplification shown is for vibration periods of 1.5, 2.0, and 4.0s. Figures 16a and 16b show the peak amplifications maps for a period of 1.5s. When comparing these figures, similar amplifications (less than 10) are observed for the zone with soil periods between 0.5 and 1.8s, except for station 84 that shows the largest amplification for both earthquakes, with values up to 20 times for the 2017 earthquake. On the other hand, a decrease is observed close to "Basilica de Guadalupe" (north of the city), as well as in the deepest clay deposits (stations 20, 31, and 35). The amplification for periods of 2.0s (Figure 16c and Figure 16d) are larger for the 1989 earthquake, especially in sites located close to the Condesa and Roma colonies, where severe damage was observed during both September 19 earthquakes. Finally, for sites in zones with the deepest soil deposits of lakebed with periods around 4.0s (Figure 16e and Figure 16f), there is a decrease in the amplification, as can be seen in the "Xochimilco" area and around the Mexico City airport (31 and 35 stations). For other periods not shown in Figure 16, the trend indicates that there is a decrease in the peak amplification, except for station 84 for the EW component, where there is an increase close to 50% for the 2017 earthquake. As mentioned previously, this station has a particular behavior due to possible basin-edge effects that increase its response in only one direction.

Figure 17 shows the amplification decrease, in percentage, between the 1989 and 2017 earthquakes for both orthogonal components and the amplitude corresponding to the dominant soil period of each

accelerometric station. As can be seen in Figure 17, there is a considerable decrease in amplification in many stations, especially in the area with soil periods between 1 and 3s, coinciding, for most sites, with the soil dominant period changes shown in Figure 14.

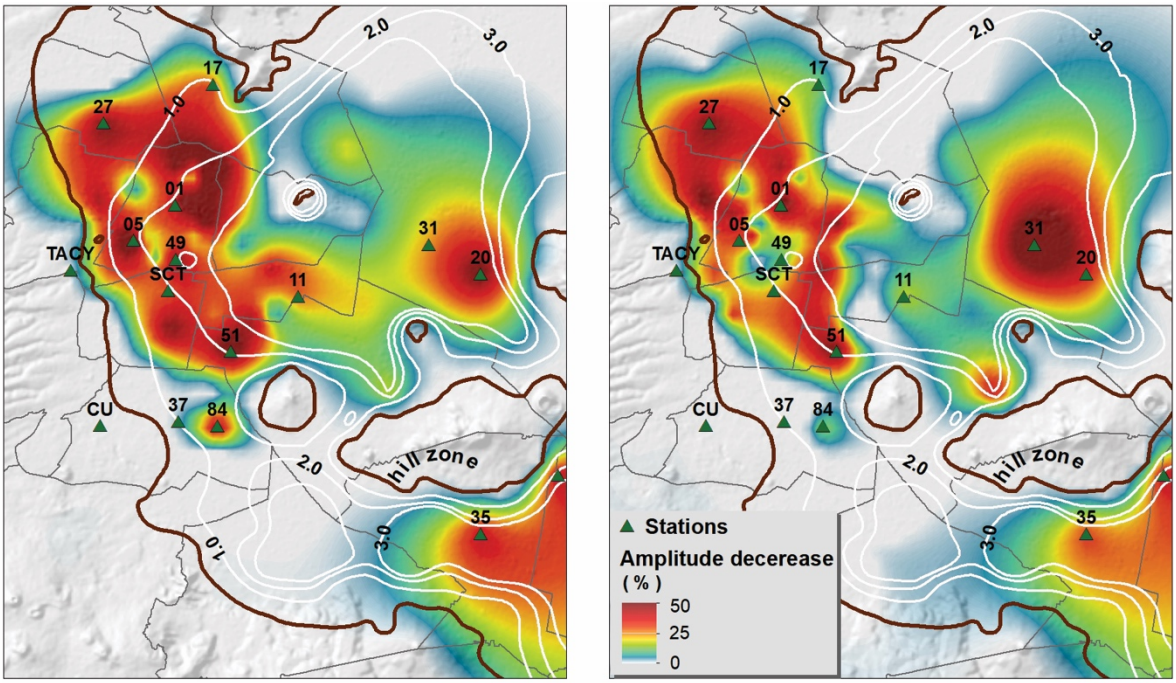

a) EW direction b) NS direction

Figure 17. Map of amplification differences between the 1989 and 2017 earthquakes (in percentage).

From the analyses presented above, it can be noticed, since 1989, a change in the behavior of the local soil effects in large part of the lakebed of Mexico City. As other authors have shown (Arroyo *et al.* 2013, Avilés and Pérez-Rocha 2010), this is associated with the groundwater pumping that has contributed to the consolidation of the aquitards underlying the Valley of Mexico causing exceptional ground subsidence levels.

Seismic demands of Mexico City structures due to September 19, 2017 earthquake

The seismic demands analyzed in this study (pseudoacceleration, hysteretic energy, and normalized hysteretic energy) were computed using the 77 accelerometric stations presented in Figure 1.

1 Pseudoacceleration demands

Figure 18 shows the pseudoacceleration demands in terms of response spectra (Sa) for selected accelerometric stations, each one plotted with the official design spectra of the Mexico City code (NTCD-2004). The design spectra are different for most stations since these spectra are computed from the dominant period at each site. Also shown are the buildings that collapsed during the earthquake (Figure 18, red dots). As can be seen in the spectra, the highest demands were computed where the dominant soil period is between 1.0s and 1.8s, coinciding roughly with the severely damaged area. Note that station 84 exhibits very large Sa demand, exceeding for one horizontal component the design spectrum by approximately 30%, while the SCT spectra remain below 50% of its corresponding design spectrum. Likewise, the spectra in other sites of the hill zone (30, 47, 74) also exceeded the design values. Station 35 is over the deepest soil deposits of lakebed zone, and the demands for the second and third vibration modes are large, reaching intensities that exceeded the design spectrum in periods lower than 1.0s. As has been stated, some of the spectra exceeded the design one but only by one horizontal component of motion. If the average horizontal spectra are computed, the resulting spectra never exceeded, in any station, the design one.

The maximum computed demands and reported damage during the September 19, 2017 earthquake, occurred in areas considerably different from those traditionally observed with inslab earthquakes, such as that of

September 19, 1985. This because the intraslab earthquakes at R<250 km from Mexico City have shown to have more energy for shorter frequencies than those of the inslab events. In particular, the 1985 earthquake had peaks around 2s while de 2017 ones had them in 1-1.5s.

Figure 19 shows Sa maps for the September 19, 2017 earthquake for SDOF systems with periods of 1.0, 1.5, 2.0, and 3.0s, and for the geometric mean spectra of both orthogonal components, together with the accelerometric stations, damage buildings and some reference sites. There are intensity differences in areas with largest demands as well as in the spatial distribution of the damage. All the maps where computed using a bilinear interpolation without considering additional soil characteristics to interpolate the intensities.

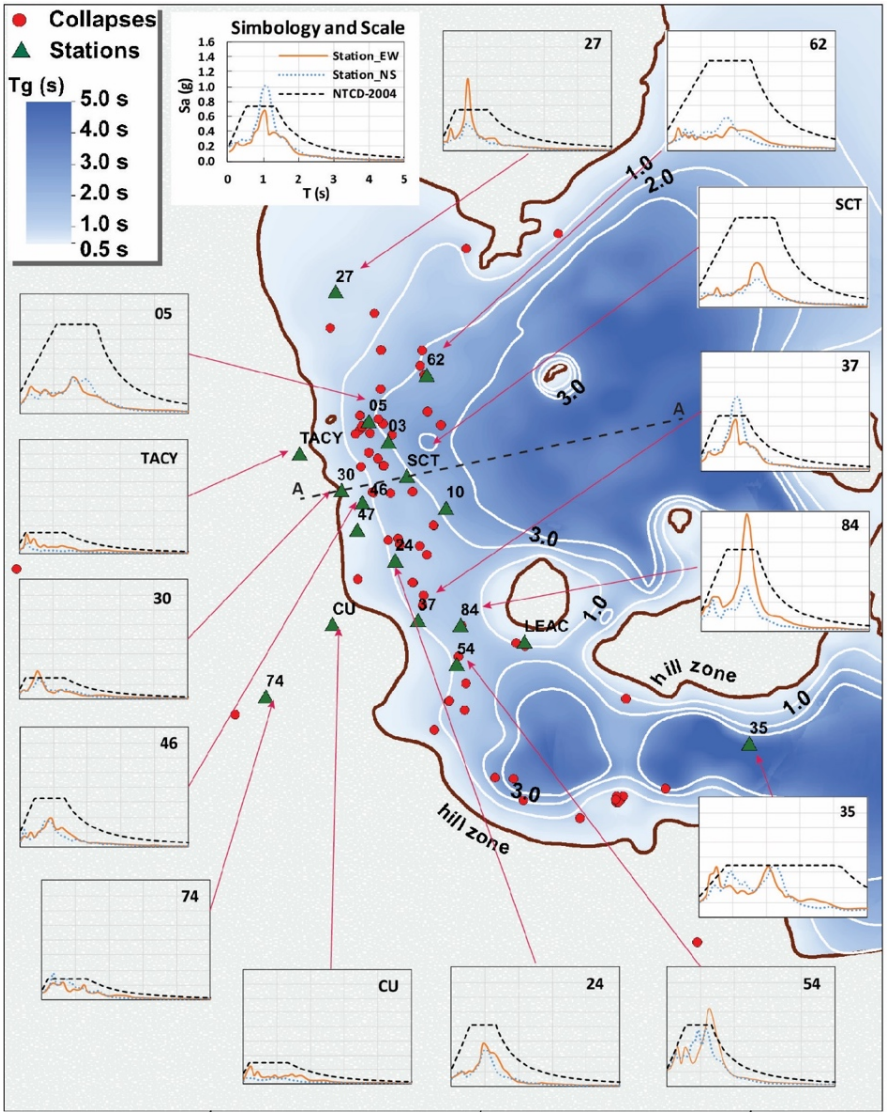

Figure 18. Pseudoacceleration spectra for the September 19, 2017 earthquake for both orthogonal directions and compared with the design spectra included in the seismic regulations in 2017 (NTCD-2004).

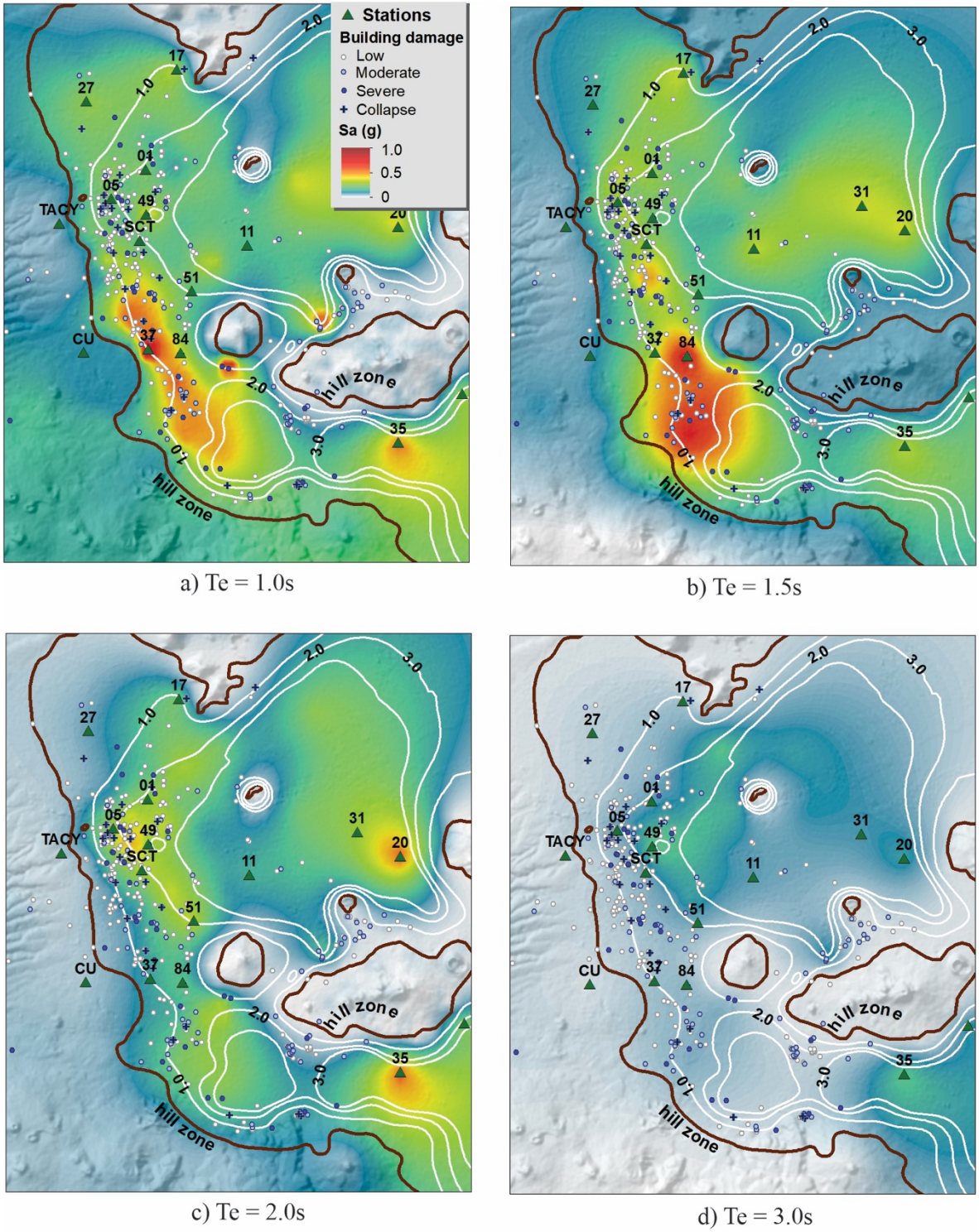

Figure 19. Pseudoacceleration maps for the September 19, 2017 earthquake for different periods. a) 1.0s, b) 1.5s, c) 2.0s, and d) 3.0s

From Figure 19, it can be observed that the lakebed zones with periods between 1 and 1.5 had the most significant intensities, coinciding roughly with the zones where damage to buildings was present (Figure 19a and Figure 19b). The map shown in Figure 19c, which corresponds to the maximum intensity for 2s, shows a better correlation to damage in the downtown area. Figure 19d exhibit that, despite large soil dominant periods in Mexico City, the intensity for periods larger than 2.5 s is not large, and slight damage is expected in those areas; however, second and third vibration modes, with periods around 1s, may present relatively high intensities. What these maps show is that there is a strong correlation between the dominant period, soil amplification and damage, but is not strong enough to explain all damage patterns and, also, no damage

patterns. This apparent complexity arises from many aspects such as 1) most of the damaged structures were built before 1985. Therefore, the seismic regulations at that time did not represent the real seismic hazard of the area, 2) although there is a considerable density of accelerometric stations in that area, the soft-soil behavior in Mexico City varies significantly within dozens of meters due to the clay depth, so important intensity information was simply not captured by the array. A special interpolation scheme (Perez-Rocha 1998, Worden *et al.* 2018) should be used to obtain a reliable and definite intensity map.

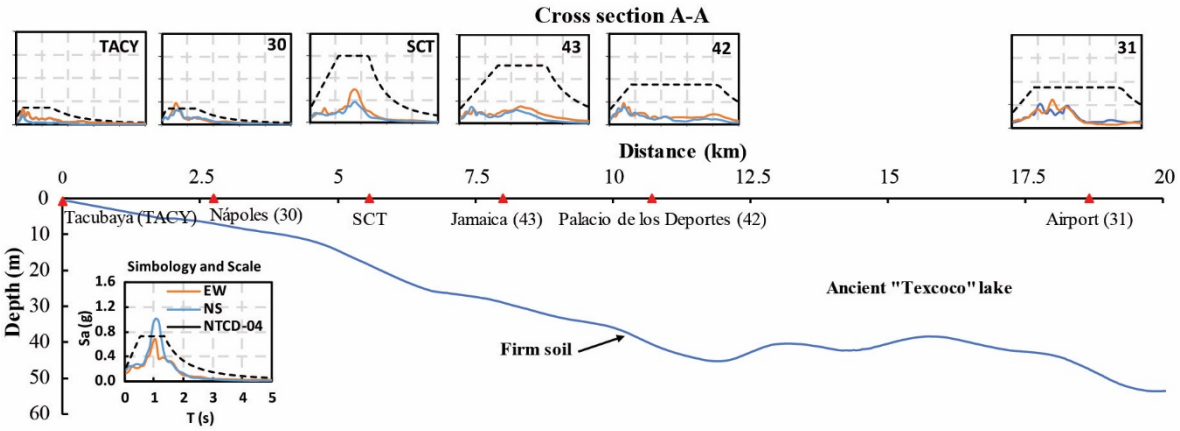

Figure 20. Behavior of seismic demands in relation with clay depth of lake-bed zone

Figure 20 illustrates the variation of the pseudoacceleration spectra for this earthquake and the design spectra for the lakebed clay depth of the ancient "Texcoco" lake for the cross-section A-A shown in Figure 18. For most sites in the valley, the soil vibration period is directly correlated to the depth of the clay strata shown in Figure 20 and, consequently, to the intensities recorded at ground level.

2 HYSTERETIC ENERGY DEMANDS

The damage suffered by the structures over the soft-soil in Mexico City depends not only on the acceleration demands and the frequency content but also on the very long duration of the strong ground motion. In the case of lakebed zone of Mexico City, where the structures are subjected to long-duration earthquakes, the disadvantage of using spectral acceleration as structural design parameter is that the potential damage due to cumulative damage effects is not considered (Fajfar, 1992; (Kunnath and Chai, 2004) Quinde *et al.* 2019). The explicit consideration of cumulative damage (low-cycle fatigue) during seismic design is usually based on energy concepts (Housner, 1956; Kuwamura and Akiyama, 1994).

Structural damage is associated with the plastic behavior of the system, which could be studied from the hysteretic energy dissipated by a structure during an earthquake ($E_{H\mu}$). This energy corresponds to the total area of hysteretic cycles that a structure develops during an intense earthquake, and for its calculation, the entire duration of the seismic record is considered. Figure 21 shows the hysteretic energy ($E_{H\mu}$) demands from the September 19, 2017 earthquake, for SDOF systems with elasto-perfectly-plastic behavior. The maps represent the $E_{H\mu}$ for periods of 1.5s as well as those associated with the peak energy of each site no matter at which period (maximum envelope demands).

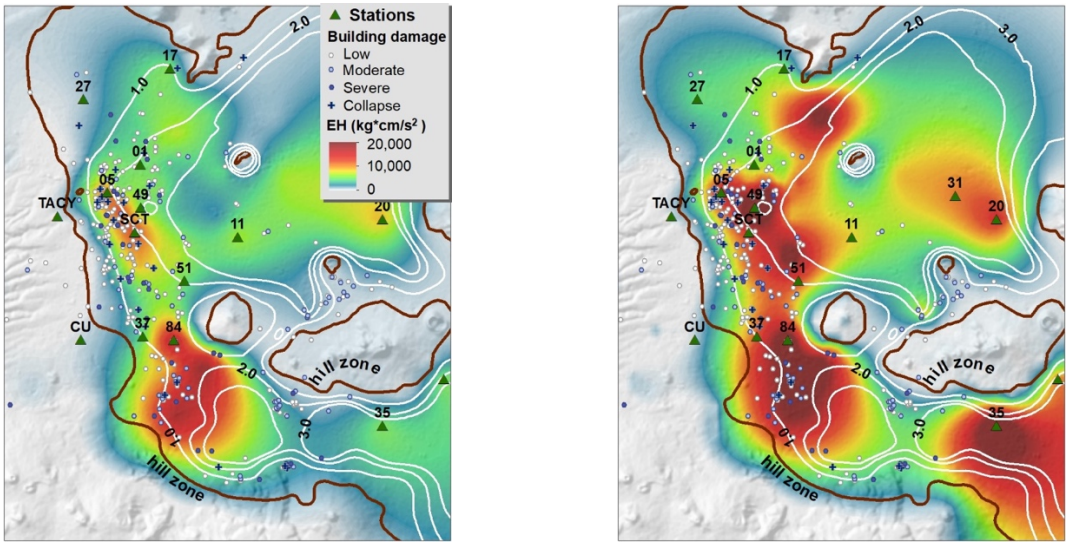

Figure 21. Hysteretic energy maps for the September 19, 2017 earthquake: $E_{H\mu}$ for a SDOF of 1.50s, left, and $E_{H\mu}$ for the maximum demands envelope, right.

As shown in Figure 21, the $E_{H\mu}$ demands are large for site with soil period close to 1.5s, with station 84 (Tg = 1.4s) being the one with the largest demands. In the map of the envelope of maximum demands, it is shown that the $E_{H\mu}$ is reasonably associated with damage area.

From the hysteretic energy, the accumulated plastic demands could be known. However, this energy does not contain enough information to associate it with structural damage, since the total dissipated energy could be similar for two different structural responses. Due to this, it is convenient to use the normalize hysteretic energy (Darwin and Nmai 1986); (Krawinkler, H. and Nassar 1992):

$$NE_{H\mu} = \frac{E_{H\mu}}{F_y x_y} \tag{1}$$

where F_y and x_y are the yielding strength and displacement, respectively.

This normalized hysteretic energy, $NE_{H\mu}$ is related to the number of times the accumulated elastic energy must be dissipated and, therefore, can be associated with structural damage. As shown in Figure 22, the largest $NE_{H\mu}$ (maximum) match with part of the area with reported damage. These $NE_{H\mu}$ demands were computed for an elasto-perfectly-plastic model using Mexican regulations to calculate the single-degree-of-freedom (SDOF) lateral strength. The maps correspond to a value of relatively large ductility of the structure (Q = 3.0 from the NTCD-2004). The damage reported in areas near downtown is associated with the structural performance of the buildings rather than the intensity of the seismic demands.

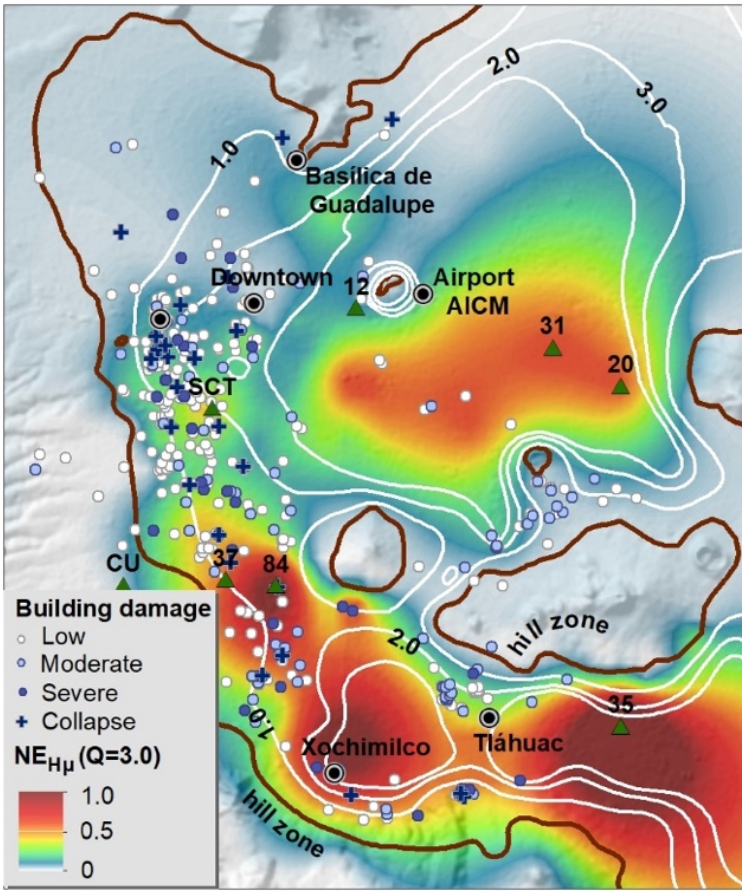

Figure 22. Normalized hysteretic energy maps for the September 19, 2017 earthquake, for the maximum demands envelope

The largest $NE_{H\mu}$ intensities are concentrated to the south of the lakebed area (Xochimilco, Tlahuac) and near the international airport. However, the downtown area, where severe damage was observed, shows relatively low demands (less than 10). This is because the maps have been computed with data from stations, but the interpolation did not accounted for soil characteristics at sites without recorded data, where larger amplifications (not recorded) could have been present.

Changes in the dominant soil period may have implications for the structural performance of buildings since the initial design conditions would be different by changing the soil-foundation behavior. This change of period has been considered in the update of the construction standards of Mexico City, with predictive models (Arroyo *et al.* 2013). However, continuous monitoring of this period change should be taken, since it is no related to a natural phenomenon.

On the other hand, in soft soil sites similar to those in Mexico City, where every 10 to 20 years are subjected to intense long-duration and narrow-banded earthquakes, it is not enough to analyze the intensities associated with peak values, such as pseudoacceleration and spectral displacement. In such sites, it is necessary to analyze the seismic demands that consider the accumulated damage and dissipated energy. As can be seen in Figures 21 and 22, damage to sites with soil periods similar to Tg=1.5s may be explained from the high plastic demands, although in areas near downtown and Roma-Condesa neighborhoods, the damage is related to structural characteristics, such as the year of construction, structural pathologies or even accumulated damage over time.

CONCLUSIONS

In this article, a study of the soil behavior of the lakebed of Mexico City was presented, based on the analysis of the Fourier amplification ratios computed from acceleration records of thirteen strong earthquakes that occurred in Mexico from 1985 to 2017. There is evidence of the change over time in Tg and peak amplification at several sites. These changes over time are mostly due to anthropogenic conditions, in particular, ground subsidence produced by groundwater pumping.

With the soil periods computed from the Fourier spectral ratios for the September 19, 2017 earthquake, the demands of pseudoacceleration and hysteretic seismic energy were obtained for the two orthogonal components and the 77 stations shown in Figure 1. The spectral accelerations (Sa) reached very high values, especially for station 84, with a maximum Sa close to 1.6g, the largest ever recorded in the city. This station also showed evidence of local wave effects that increased its response in only one direction. The Sa maps show a good correlation with the damage reported during the 2017 earthquake, especially in the zone with Tg<1.8s, wherein certain sites the demands exceeded the design spectra of the Mexico City regulations.

The hysteretic energy and the normalized hysteretic energy showed a relationship with the damage reported for sites with Tg<1.5s. However, in the downtown area, where severe damage was concentrated, no correlation between intensities and damage was observed. As mentioned in this study, this is because the maps have been computed with data from stations, but no accelerometric stations are located in the western part of the city over soils with Tg=1.5s, so no large intensities were recorded but undoubtedly present. On the other hand, for sites over deeper clay deposits, high hysteretic energy demands were observed. However, no damage has occurred, mainly because in this area, there are no structures that can vibrate with periods similar to those of the soil (Tg> 3.5s). For sites of the deepest lakebed zone, it was observed that the second and third modes of soil vibration were excited considerably, reaching demands like those reported for sites with Tg<1.5s.

ACKNOWLEDGEMENT

The authors thank CIRES, the Seismic Instrumentation Unit of the Institute of Engineering and the Institute of Geophysics of the UNAM, who provided the accelerographic records used in this study, and SaLvador Ramos for the support in the development of this article. Also, the first author thanks CONACYT for the scholarship given to carry out this research

REFERENCES

Arroyo, Danny, Mario Ordaz, Efrain Ovando-Shelley, Juan C. Guasch, Javier Lermo, Citlali Perez, Leonardo Alcantara, and Mario S. Ramírez-Centeno. 2013. "Evaluation of the Change in Dominant Periods in the Lake-Bed Zone of Mexico City Produced by Ground Subsidence through the Use of Site Amplification Factors." *Soil Dynamics and Earthquake Engineering* 44: 54–66. https://doi.org/10.1016/j.soildyn.2012.08.009.

Avilés, Javier, and Luis Eduardo Pérez-Rocha. 2010. "Regional Subsidence of Mexico City and Its Effects on Seismic Response." *Soil Dynamics and Earthquake Engineering* 30 (10): 981–89. https://doi.org/10.1016/j.soildyn.2010.04.009.

Baena-Rivera, Marcela, L Eduardo Perez-Rocha, and Francisco J Sanchez-Sesma. 2017. "Frecuency Wavenumber Analysis of Strong Ground Motion in Mexico City." *Geofisica Internacional* 56 (1): 103–16. https://doi.org/10.19155/geofint.2017.056.1.8.

CIRES. n.d. "Red Acelerométrica de Ciudad de México." http://www.cires.org.mx.

Cruz-Atienza, V. M., J. Tago, J. D. Sanabria-Gómez, E. Chaljub, V. Etienne, J. Virieux, and L. Quintanar. 2016. "Long Duration of Ground Motion in the Paradigmatic Valley of Mexico." *Scientific Reports* 6 (June): 1–9. https://doi.org/10.1038/srep38807.

Darwin, D, and Ck Nmai. 1986. "Energy Dissipation in RC Beams under Cyclic Load." *ASCE Journal of Structural Engineering* 112 (8): 1829–46. https://doi.org/10.1061/(ASCE)0733-9445(1986)112:8(1829).

Fajfar, Peter. 1992. "Equivalent Ductility Factors, Taking into Account Low-Cycle Fatigue." *Earthquake Engineering & Structural Dynamics* 21 (10): 837–848. https://doi.org/10.1002/eqe.4290211001.

Field, E. H., and K. H. Jacob. 1995. "A Comparison and Test of Various Site-Response Estimation Techniques, Including Three That Are Not Reference-Site Dependent." *Bulletin - Seismological Society of America* 85 (4): 1127–43.

Field, E, K Jacob, and S Hough. 1992. "Earthquake Site Response Estimation: A Weak-Motion Case Study." *Bulletin of the Seismological Society of America* 82 (6): 2283–2306. https://doi.org/10.1785/0120160029.

Gutierrez, C., and S. K. Singh. 1992. "A Site Effect Study in Acapulco, Guerrero, Mexico: Comparison of Results from Strong-Motion and Microtremor Data." *Bulletin - Seismological Society of America* 82 (2): 642–59.

Housner, George. 1956. "Limit Design of Structures to Resist Earthquakes." In *First World Conference on Earthquake Engineering*, 1–13.

Krawinkler, H. and Nassar, A. 1992. "Seismic Design Based on Ductility and Cumulative Damage Demands and Capacities." In *Nonlinear Seismic Analysis and Design of Reinforced Concrete Buildings*, edited by Elsevier Applied Science, 95–104. Bled, Slovenia.

Kunnath, S. K., and Y. H. Chai. 2004. "Cumulative Damage-Based Inelastic Cyclic Demand Spectrum." *Earthquake Engineering & Structural Dynamics* 33 (4): 499–520. https://doi.org/10.1002/eqe.363.

Kuwamura, Hitoshi, and Hiroshi Akiyama. 1994. "Prediction of Earthquake Energy Input from Smoothed Fourier Amplitude Spectrum." *Earthquake Engineering & Structural Dynamics* 23 (November 1993): 1125–37.

Lermo, J, and F J Chavez-Garcia. 1994. "Are Microtremors Useful in Site Response Evaluation?" *Bulletin of the Seismological Society of America* 84 (5): 1350–64. https://doi.org/10.1306/080700710318.

Ordaz, Mario, Shri Krishna Singh, J Lermo, Marco Espinosa-Johnson, and T Dominguez. 1988. "The Mexico Eartjquake of September 19, 1985: Estimation of REsponse Spectra in the Lake Bed Zone of the VAlley of Mexico." *Earthquake Spectra* 4 (4).

Perez-Rocha, Luis. 1998. "Respuesta Sísmica Estructural: Efectos de Sitio e Interacción Suelo-Estructura." UNAM, Mexico.

Pérez-Rocha, Luis Eduardo, Francisco J Sanchez-Sesma, and Eduardo Reinoso. 1991. "Three-Dimensional Site Effects in Mexico City: Evidences for Accelerometric Network, Observations and Theoretical Results." In *IV International Conference Seismic Zonification*, 2:327–34.

Quinde, Pablo, Amador Terán-gilmore, and Eduardo Reinoso. 2019. "Cumulative Structural Damage Due to Low Cycle Fatigue : An Energy-Based Approximation." *Journal of Earthquake Engineering* (in press) (00): 1–30. https://doi.org/10.1080/13632469.2019.1692736.

Reinoso, Eduardo. 1991. "Efectos Sísmicos Locales En El Valle de México: Amplificación En La Zona Lacustre." In *IX NAtional Conference Earthquake Engineering*, 2:224–36.

Reinoso, Eduardo, and Mario Ordaz. 1999. "Spectral Ratios for Mexico City from Free-Field Recordings." *Earthquake Spectra*. https://doi.org/10.1193/1.1586041.

Reinoso, Eduardo, L Wrobel, and H Power. 1997. "Two-Dimensional Scattering of P, Sv and Rayleigh Waves: Preliminary Results for the Valley of Mexico." *Earthquake Engineering & Structural Dynamics* 26 (October 1996): 595–616.

Safak, E. 1991. "Problems with Using Spectral Ratios to Estimate Site Amplifications." In *IV International Conference on Seismic Zonification*, 227–34. Stanford, CA.

Singh, S. K., E. Reinoso, D. Arroyo, M. Ordaz, V. Cruz-Atienza, X. Pérez-Campos, A. Iglesias, and V. Hjörleifsdóttir. 2018. "Deadly Intraslab Mexico Earthquake of 19 September 2017 (Mw 7.1): Ground Motion and Damage Pattern in Mexico City." *Seismological Research Letters* 89 (6): 2193–2203. https://doi.org/10.1785/0220180159.

Singh, Shri Krishna, J Lermo, T Dominguez, Mario Ordaz, Marco Espinosa-Johnson, E Mena, and R Quaas. 1988. "The Mexico Eartjquake of September 19, 1985: A Study of Amplification Of Seismic Waves in the Valley of Mexico with REspect to a Hill Zone Site." *Earthquake Spectra* 4 (4).

Worden, B., Eric M. Thompson, Jack W. Baker, Brendon A. Bradley, Nicolas Luco, and David J. Wald. 2018. "Spatial and Spectral Interpolation of Ground-Motion Intensity Measure Observations." *Bulletin of the Seismological Society of America* 108 (2): 866–75. https://doi.org/10.1785/0120170201.

Original paper

GROUND MOTION PREDICTION MODEL FOR SOUTHEASTERN MEXICO REMOVING SITE EFFECTS USING THE EARTHQUAKE HORIZONTAL-TO-VERTICAL SPECTRAL RATIO (EHVSR)

Javier F. Lermo-Samaniego*[1], Miguel A. Jaimes[1], Francisco J. Sánchez-Sesma[1], Cristian Campuzano-Sánchez[1], Hugo Cruz-Jiménez[1,3] and José Oscar Campos-Enriquez[2]

Received: September 23, 2019; accepted: April 22, 2020; published online: October 1, 2020

RESUMEN

Se propone un modelo de atenuación del movimiento del terreno (GMPE, por sus siglas en inglés) para el sureste de México. El modelo de atenuación es una función de la magnitud y distancia. Se utilizan 86 sismos con magnitudes $5.0 \leq M_w \leq 8.2$ (se incluyen registros del terremoto de Tehuantepec del 7/09/2017, Mw 8.2) y distancias epicentrales entre $52 \leq R \leq 618$ km. Los eventos se registraron en nueve estaciones de la red acelerométrica del Instituto de Ingeniería de la Universidad Nacional Autónoma de México (II-UNAM) instaladas en los estados de Chiapas, Oaxaca, Tabasco y Veracruz. Se estima el efecto de sitio de los registros sísmicos de estas estaciones mediante el cociente espectral promedio de los movimientos horizontales y el vertical de sismos (EHVSR, pos sus siglas en inglés).Se señala la necesidad de remover el efecto de sitio en los modelos actuales de atenuación del movimiento fuerte debido a que inducen sobreestimación de los sismos.

PALABRAS CLAVE: GMPE para el Sureste de México, efecto de sitio, EHVSR.

ABSTRACT

A ground motion attenuation model (ground motion prediction equation, GMPE) for southeastern Mexico is proposed. The attenuation model was built as a function of magnitude, and distance. A number of 86 earthquakes were used with $5.0 \leq Mw \leq 8.2$ (including the recordings of the 9/7/2017, Mw8.2 Tehuantepec earthquake), and distances between $52 \leq R \leq 618$ km. They were recorded in nine stations of the Engineering Institute of the National Autonomous University of Mexico (II-UNAM) accelerometric network installed in the states of Chiapas, Oaxaca, Tabasco and Veracruz. From all recordings of each of these stations, we removed site effects, which were estimated using the average Earthquake Horizontal to Vertical Spectral Ratio (EHVSR). This work points out the need to remove site effect in the current GMPEs, which tends to overestimate this effect.

KEY WORDS: Ground-Motion Prediction Equation (GMPE) for Southeast Mexico, site effect, EHVSR (Earthquake Horizontal to Vertical Spectral Ratio).

**Corresponding author: jlermos@iingen.unam.mx*

1 Instituto de Ingeniería, Universidad Nacional Autónoma de México. Circuito Interior, Ciudad Universitaria, Coyoacán, 04510, CDMX, México

2 Instituto de Geofísica, Universidad Nacional Autónoma de México. Circuito Interior, Ciudad Universitaria, Coyoacán, 04510, CDMX, México.

3 Instituto de Ingeniería, Universidad Veracruzana, Boca del Río, Veracruz, México

INTRODUCTION

On September 7, 2017, a Mw8.2 earthquake took place in the Tehuantepec Gulf, 133 km to the southwest of Pijijiapan, Chiapas. This earthquake occurred at 23:49:18, local time (September 08, 2017; 04:49 UTM), localized by the National Seismological Service (SSN for Servicio Sismológico Nacional, in Spanish) at 14.85° N and 94.11° W, at a depth of 58 km (Figure 1). It caused major damage in southeastern Mexico, in particular in the states of Chiapas and Oaxaca (Special Report, SSN, 2017). Specific different conditions are associated with these two states. While in Oaxaca the damages are concentrated almost in the isthmus region municipalities, in Chiapas the effects are scattered, affecting 82 out of the 122 municipalities of this state, amounting more than a million people (HIC-AL, 2017).

In the last years, major progresses have been achieved in understanding the origin of the subduction and intraplate seismicity in central Mexico (i.e., García, 2007). For example, the advance in the knowledge of wave propagation from these events, as well as our capacity to estimate the ground motions due to such events. In contrast, the study of seismic events from the southeastern Mexico has been rather limited, in particular the region of the Tehuantepec Isthmus and the Chiapas State.

Southeastern Mexico is featured as a tectonically active zone associated with the interaction of the North American, Caribbean and Cocos tectonic plates. The first two plates are in lateral contact along the Polochic-Motagua Fault System. The Central America Volcanic Arc (AVCA; from the initials in Spanish) is due to the subduction of the Cocos plate beneath the North America to the north, and beneath the Caribbean plate to the south (Figure 1). This volcanic arc stretches more than 1,300 km from the Tacana active volcano, at the Mexico-Guatemala border, up to the Turrialba volcano in eastern Costa Rica. This subduction process in Mexico has given rise to the Chiapas Volcanic Arc (AVC; from the initials in Spanish) that irregularly extends in Chiapas up to El Chichón Volcano.

Pre-Mezosoic basement rocks are present in Central America (in Chiapas, Guatemala, Belice and Honduras). These rocks crop out south of the Yucatan-Chiapas block. The coast parallel Upper Precambrian-Lower Paleozoic Chiapas Massif covers a surface of more than 20,000 km^2, and constitutes the largest Permian crystalline complex in Mexico, comprising plutonic and metamorphic deformations (Weber *et al.*, 2006).

Three seismogenic sources feature this region. The first one is associated with the subduction of the Cocos plate beneath the North American plate (Figure 1). In this study it is considered that the contact between these two plates reaches a depth of 80 km (Figure 1, right panel). Kostoglodov and Pacheco (1999) analyzed six events from this source. They occurred on April 19, 1902 (M7.5), September 23, 1902 (M7.7), January 14, 1903 (M7.6), August 6, 1942 (M7.9), October 23, 1950 (M7.2), and April 29, 1970 (M7.3). For the September 23, 1902, and April 29, 1970 events, focal depths of 100 km beneath the Chiapas depression were reported by Figueroa (1973), which seems too large and probably related to scarce recordings. In the meantime, three major seismic events that took place in this region have been accurately localized by the SSN. These earthquakes are: September 19, 1993 (M_w 7.2) localized near Huixtla, Chiapas, with a focal depth of 34 km, November 7, 2012 (M_w 7.3), 68 km southwest of Ciudad Hidalgo, Chiapas, with a focal depth of 16 km and a reverse fault mechanism (severe damages affected San Marcos, Guatemala), and the Tehuantepec isthmus zone, September 7, 2017 (M_w 8.2), which constitutes the strongest historical earthquake recorded in Mexico, localized at 133 km southwest of Pijijiapan, Chiapas at a depth of 58 km. Its normal faulting focal mechanism adds to the controversy on the earthquakes of this region (an inverse faulting mechanism was expected). Also noteworthy is the number of aftershocks that amounted to 4,075 in 15 days, forming distributed

clusters in all the Tehuantepec Gulf (special Report, SSN, Nov. 2017). Also contrasting are the observed peak accelerations. Even more, the peak accelerations at the horizontal components observed at the coast (NILT ~ 500 gals) contrast with the maximum values observed in stations located in the Chiapas depression (at stations TGBT and SCCB, values of ~ 300 ~ 100 gals, respectively). These contrasting values might be due to the Chiapas Massif that attenuates waves coming from the subduction zone. The second seismogenic source comprises the internal deformation of the subducted plate, and generates seismic events in a depth range between 80 and 250 km. An example is the October 21, 1995 (M_w 7.2) earthquake, localized 57 km from Tuxtla, Chiapas, at a depth of 165 km, which also shows variations in the peak accelerations observed at the recordings of this zone (Rebollar *et al.*, 1999). Another deep seismic event occurred on June 14, 2017 (M_w 7.0), located 74 km to the northeast of Ciudad Hidalgo, Chiapas, with a focal depth of 113 km. The third seismogenic source corresponds to a less than 50 km depth crustal deformation that comprises shallow faults. Approximately 15 faults produce the observed seismicity. The associated seismic events are of moderate magnitudes that cause local damages, as reported by Figueroa (1973). Examples from this third source are the swarms with peak M_c 5.5, that occurred in Chiapa de Corzo during July-October, 1975 (Figueroa *et al.*, 1975).

Considering the past seismic activity, here summarized, and the recent Tehuantepec earthquake (September 7, 2017, Mw8.2), it is of interest to analyze these seismic events to develop an attenuation model for the strong motion for southeastern Mexico (GMPE). In this study, based on the one stage maximum likelihood technique (Joyner and Boore, 1993), we developed empirical expressions to estimate the response spectra for the 5 per cent critical damping, peak ground acceleration (PGA), and peak ground velocity (PGV) for 86 seismic events.

As it is customary accepted, seismic ground motion can be roughly represented by three main factors: source, path, and site effects. This convolutional model is a crude approximation of reality, yet it is useful to assess significant characteristics of ground motion. The effects of surface geology, usually called site effects, can give rise to large amplifications and enhanced damage (see Sánchez-Sesma, 1987). In principle, transfer functions associated to sundry incoming waves with various incidence angles and polarizations can describe site effects. However, the various transfer functions are often very different partially explaining why the search for a simple factor to account for site effects has been futile so far. With the advent of the diffuse field theory (see Weaver, 1982; 1985; Campillo and Paul, 2003; Sánchez-Sesma *et al.*, 2011a), it is established the great resolving power of average energy densities within a seismic diffuse field. The coda of earthquakes is the paradigmatic example of a diffuse field produced by multiple scattering (see Hennino *et al.*, 2001; Margerin *et al.*, 2009). In a broad sense, this is the case of seismic noise (Shapiro and Campillo, 2004) and ensembles of earthquakes (Kawase *et al.*, 2011; Nagashima *et al.*, 2014; Baena-Rivera *et al.*, 2016). Therefore, according to Kawase *et al.* (2011) the EHVSR in a layered medium is proportional to the ratio of transfer functions associated to vertically incoming P and SV waves, without surface waves. Uniform and equipartitioned illumination give rise to diffuse fields (Sánchez-Sesma *et al.*, 2006). In irregular settings, multiple diffraction tends to favor equipartition of energy in the diverse states: P and S waves and sundry surface (Love and Rayleigh) waves. Sánchez-Sesma *et al.* (2011b) showed that by assuming a diffuse wave field, the NHVSR can be modeled in the frequency domain in terms of the ratio of the imaginary part of the trace components of Green's function at the source. This approach includes naturally the contributions from Rayleigh, Love and body waves.

In seismic zones, it seems reasonable to use recorded ground motions to compute the average energy densities of earthquake ground motions and assess by their ratios approximate average spectral realizations of site effects (Carpenter *et al.*, 2018). Therefore, the use of a binary variable is clearly very rough and does not account for the presence of dominant frequencies excited during earthquake shaking. The average EHVSR approximately accounts for this. The GMPE has a regional use and they should be free of site effects in order to avoid bias in the model. This research aim is to approximately remove this effect.

In order to evaluate seismic hazard, site effects have to be incorporated back correcting the GMPE using HVSR with the appropriate corrections as proposed by Kawase *et al.* (2018). Note that HVSR is a proxy of empirical transfer functions in low frequencies with obvious underestimations in higher frequencies. In fact, several authors have stated that, the noise HVSR spectral ratio (NHVSR) provides a reasonable estimate of the site dominant frequency (see Nakamura, 1989). However, its amplitude is subject of controversy (i.e., Finn, 1991; Gutiérrez and Singh, 1992; Lachet and Bard, 1994). In very soft sedimentary environments the NHVSR, the EHVSR and the theoretical transfer functions are in reasonable agreement in low and moderate frequencies (Lermo and Chávez-García, 1994b).

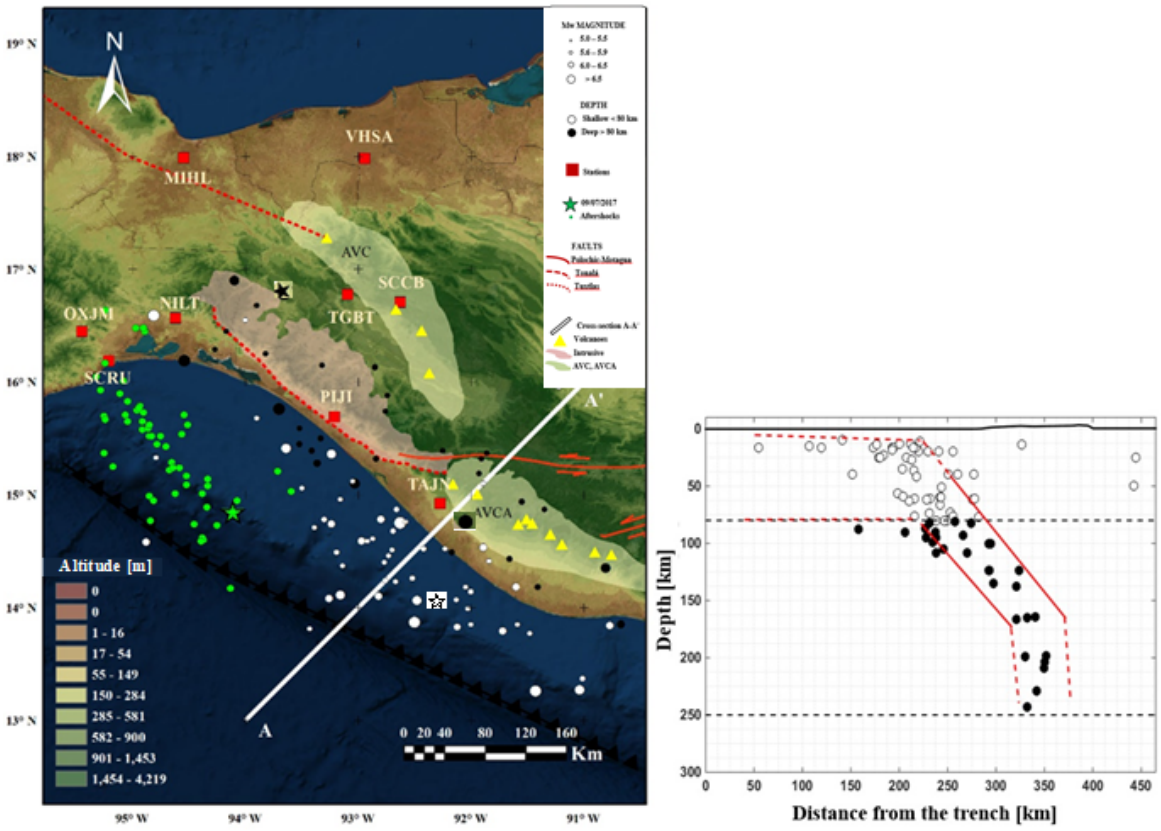

Figure 1. Left panel shows a map of the southeastern Mexico indicating the epicenters of earthquakes analyzed in this study (white and black circles), aftershocks of the September 8, 2017 earthquake (green circles), stations (red squares), volcanoes (yellow triangles) faults, an intrusive, as well as the Central America Volcanic Arc (AVCA; from the name in Spanish) and Chiapas Volcanic Arc (AVC; from the name in Spanish). The cross-section A-A' is also indicated. Right panel shows hypocenters projected on the A-A' cross-section. We separate hypocenters with depths shallower and deeper than 80 km (white and black circles, respectively).

DATA

From the SSN database we selected 86 earthquakes (of various focal mechanism) located between 90.5° W and 96.5° W and between 13° and 17° N, and which occurred between 1995 and 2017. From this database, we present a wide range of magnitudes ($5.0 \leq Mw \leq 8.2$), distances ($52 \leq R \leq 618$ km; hipocentral distances for Mw<=7.0 and rupture distances for Mw> 7.0) and depths ($10 \leq H \leq 243$ km) as shown in Figure 1 and Table 1. We obtained 261 three-components accelerograms for those events recorded at 9 stations located in Chiapas, Oaxaca, Tabasco and Veracruz. The respective stations are OXJM, SCRU, NILT, MIHL, PIJI, TGBT, VHSA, SCCB and TAJN and belong to the Seismic Network of Institute of Engineering-UNAM (Pérez-Yáñez *et al.*, 2010). Date, depth, moment magnitude (Mw) and distance for each recording are indicated in Table 1. The farthest away stations (VHSA and MIHL) have less recordings, in contrast with those sited in the central part of the study area (PIJI, NILT, SCCB, OXJM, TAJN, TGBT and SCRU) where the Chiapas State capital city (Tuxtla Gutierrez) and the hidroelectric dams are located.

The spatial distribution of the 9 accelerometric stations (red squares), and of the 86 epicenters (white and black circles) is shown in Figure 1. Also indicated are the locations of the Chiapas (AVC) and Guatemala (AVCA) volcanic arcs. The Chiapas Massif is depicted in pink. Figure 1 also shows the Polochic-Motagua (continuous red line), Tonalá and Los Tuxtlas (discontinuous red line) fault systems. The epicenter of the Tehuantepec, September 7, 2017 (Mw8.2) earthquake is indicated with a green star. Green small dots represent aftershocks with magnitudes lower than 5. A comparison of the area covered by the aftershocks of the Tehuantepec earthquake with the localized seismicity of the last 17 years indicates that the Tehuantepec aftershocks cover that portion of the Tehuantepec Gulf that had been inactive.

In the right panel of Figure 1. The 261 hypocenters analyzed in this study were projected to the A-A´ cross-section (right panel of Figure 1), whose location is indicated with a white line. A dipping angle of the slab of about 45 degrees, as well as a plate thinning at 80 km depth can be observed.

Stars indicate the epicenters of the three earthquakes with $Mw > 7.0$ (see Table 1). For these events, the minimum distance to the rupture was considered. For the October 21, 1995 earthquake (Mw 7.2), according to the rupture model proposed by Rebollar *et al.* (1999), the rupture depth (htop) lies at 80 km. For the September 8, 2017 event (Mw 8.2), we used the rupture model obtained by Ye *et al.* (2017), which has a htop = 30 km. Finally, for the November 7, 2012 (Mw 7.3) event, for which there is no rupture model, we assumed a rupture model with a htop = 10 km, with its closest edge point (northwestern edge of the fault plane) at latitude 14º N and longitude 92º W.

Figure 2 shows the distribution of magnitudes ($5.0 \leq Mw \leq 8.2$) versus distance ($52 \leq R \leq 618$ km) of the analyzed records. A concentration of events with magnitudes in the range from 5.0 to 5.5 for distances between 52 and 300 km is observed.

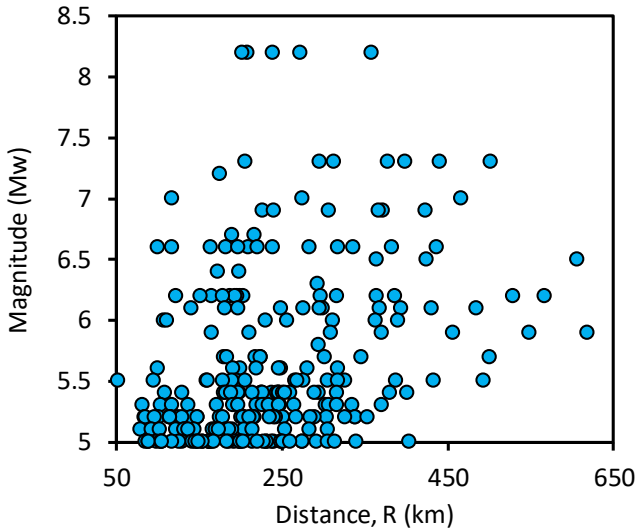

Figure 2.- Moment magnitude (Mw) distribution against distance of the analyzed seismic events.

DATA PROCESSING AND ANALYSIS

For each of the three components of the 261 recordings associated to the 86 selected seismic events, both shear waves and surface waves (also known as coda) were selected. Data processing included homogenization of the signal sampling of all extracted signals. Subsequently, for each selected record, the Fourier amplitude spectrum (FAS) was computed and the spectral ratio of horizontal components with respect to the vertical one obtained. After that, the quadratic means were obtained from both ratios. These are the directional earthquake horizontal to vertical spectral ratios (EHVSR), which were computed for a frequency band between 0.1 and 10 Hz. In Figure 3 we show the 261 ratios (thin of colors continuous lines) distributed in the 9 stations. Averages are depicted as continuous red lines (dashed red lines: average ± one standard deviation). We assume that this average of directional EHVSR´s is an estimate of the spectral amplification, a kind of empirical transfer function (ETF) of average horizontal components with respect to the vertical component. The source effect is approximately removed. In a recent paper, Kawase *et al.* (2018) suggested to consider the amplification due to vertical motion to avoid over-reduction of FAS. However, this requires recordings both in soil and rock sites.

It has been proposed that the site effect is significant for ETF larger than two (SESAME, 2015) as it is the case of scalar amplification in a half-space. However, under the assumption of a diffuse field, Sánchez-Sesma *et al.* (2011a) found theoretically that the MHVSR at the surface of a half-space is approximately given by

$$H/V \approx 1.245 + 0.348 \cdot v \qquad (1)$$

where v=Poisson ratio. If v =0.25 then the H/V is about 1.332.

Thus, according to criteria from SESAME (continuous line in Figure 3), and to that of Sánchez-Sesma *et al.* (2011) (discontinuous line in Figure 3), the 9 accelerometric stations present site effects in the analyzed frequency band. Stations NILT and PIJI reach amplifications of more than ten times at 6 and 4 Hz, respectively. Stations OXJM, SCRU and TGBT present lower amplifications.

Table 1. Earthquakes from southeastern Mexico analyzed in this study.

No.	Date (dd/mm/yy)	Lat (° N)	Lon (° W)	H* (km)	Mw	Distances of the records (km)* MIHL	NILT	OXUM	PLUI	SCCB	SCRU	TAUN	TGBT	VHSA	No.	Date (dd/mm/yy)	Lat (° N)	Lon (° W)	H* (km)	Mw	Distances of the records (km)* MIHL	NILT	OXUM	PLUI	SCCB	SCRU	TAUN	TGBT	VHSA
1	21/10/1995	16.92	93.64	165	7.2								92		47	13/03/2012	14.96	-93.16	16	5.2		242	304	83	204	266	100	203	338
2	03/06/2000	15.76	-94.66	88	5		126				117				48	01/05/2012	14.11	-93.16	40	6.1				181	298		140		
3	12/03/2000	14.59	-92.97	35	5.9		165				308				49	26/06/2012	15.39	-92.25	166	5.2		338		200		174			
4	17/10/2000	15.38	-92.51	168	5.5		317								50	29/06/2012	14.78	-93.3	18	5.3			303	103	228		117		
5	09/01/2001	15.36	-93.24	66	6.1					248					51	12/07/2012	14.87	-91.35	204	5.1				305					
6	19/01/2001	15.1	-93.03	108	6.3					292					52	29/07/2012	14.1	-92.82	14	5.7				183					
7	28/11/2001	15.41	-93.64	36	6.4		172			198					53	01/09/2012	16.13	-92.85	243	5.4		316	379	251	253				
8	16/01/2002	16.59	-94.81	76	6.7		189			217					54	14/10/2012	14.46	-92.73	13	5.2				148	251				
9	14/02/2002	14.78	-92.8	74	5.8		293								55	15/10/2012	13.77	-91.48	20	5.2				288					
10	06/06/2006	15.37	-91.86	209	5				260			220			56	27/10/2012	14.4	-92.77	59	5				163					
11	13/06/2007	13.26	-91.43	20	6.6				336			208			57	07/11/2012	14.03	-92.32	16	7.3	519	400		230	309	422		330	453
12	06/07/2007	16.9	-94.1	100	6.2	165	121	187	195	193	178	316	151	203	58	11/11/2012	14.06	-92.48	13	6.2				199	296				
13	23/07/2007	14.18	-91.41	124	5.4				289						59	16/12/2012	14.43	-91.66	100	5.4				244					
14	30/08/2007	15.68	-93.9	61	5		141		98	192					60	30/12/2012	14.49	-93.19	25	5.3				136					
15	26/11/2007	15.28	-93.36	87	5.6		218	280	100	199	245		190	317	61	31/12/2012	15.21	-92.67	82	5.2				115					
16	05/01/2008	13.83	-92.12	63	5.6				248						62	11/01/2013	14.61	-92.87	27	5.4		293		129	237				
17	06/01/2008	13.99	-92.03	20	5				231						63	11/01/2013	15.32	-91.91	229	5		403		273					
18	12/02/2008	16.19	-94.54	90	6.6	220	100		182	238	117		196	282	64	25/03/2013	14.35	-90.81	198	6.2		529		364	386	567			
19	04/04/2008	13.85	-91.59	73	5.1				282						65	10/05/2013	14.87	-92.66	35	5.3				247					
20	15/04/2008	13.27	-91.04	40	6.5			606	364	424					66	30/07/2013	15.5	-93.33	105	5.4		214		108	189	246		246	246
21	17/04/2008	15.45	-93.52	95	5.4		198	259		196	226		182		67	06/08/2013	14.18	-91.6	61	5.7			501						
22	20/09/2008	14.23	-92.67	14	5		339								68	07/09/2013	14.34	-92.26	69	6.1	484	367	431	196	276	394		295	
23	16/10/2008	13.87	-92.5	23	6.6		382	436		317					69	07/09/2013	14.14	-92	51	5.4		401		225					
24	17/01/2009	15.74	-92.76	171	5.2		284	353	178	203	326		210		70	10/01/2014	14.52	-92.23	76	5									
25	22/01/2009	15.19	-91.93	199	5				251						71	11/01/2014	14.49	-92.17	81	5.5			432	194	265		95		
26	03/05/2009	14.53	-91.89	77	5.9			456	210						72	02/03/2014	14.08	-93.26	10	5.7				180	301				
27	07/06/2009	16.15	-93.32	135	5		203	274	145	168	250		154	248	73	16/06/2014	15.1	-91.89	14	5				161	197				
28	18/01/2010	13.85	-90.67	124	5.9		548	618	370						74	07/07/2014	14.75	-92.63	60	6.9	423	305	371		226			239	367
29	23/02/2010	15.96	-91.22	25	5.4				225	180					75	20/07/2014	14.76	-92.58	80	5		313			231				
30	20/03/2010	16.03	-91.32	50	5.3				219	171					76	29/07/2014	14.68	-92.69	61	5.3		306	369		234		81	245	
31	19/08/2010	14.41	-91.84	40	5.2				212			85			77	28/08/2014	14.18	-92.05	60	5							105		
32	15/09/2010	15.59	-93.52	95	5.1		189	253	102	186			170		78	15/10/2014	14.51	-92.7	42	5.1							78		
33	01/11/2010	16.68	-93.9	124	5		148	214	183		199		154		79	19/11/2014	14.71	-93.39	25	5.2					240		129		
34	20/01/2011	16.55	-94	62	5.1	182	93	173	144	166			121		80	04/01/2015	16.29	-94.27	99	5.1					213			173	
35	27/03/2011	14.24	-92.76	16	5.5			387		276					81	12/01/2015	15.39	-93.41	82	5.5	326	205	268		190		160	178	305
36	26/04/2011	15.88	-92.74	138	5				149						82	20/01/2015	14.94	-91.55	164	5.5			493						
37	07/06/2011	15.06	-93.5	56	5.2		216		96	215	235				83	01/03/2015	13.37	-91.01	40	5.3							226		
38	13/08/2011	14.58	-94.88	16	5.7		224	218	224	346			137		84	01/05/2015	15.73	93.71	90	5		164	227		186			163	
39	06/09/2011	16.25	-93.82	93	5.1		133	205	131	170					85	15/05/2015	13.85	-92	11	5.2							124		
40	19/10/2011	15.12	-93.05	80	5		237	305	104	200					86	18/05/2015	14.07	-92.13	62	5.2							114		
41	17/11/2011	14.52	-92.42	20	5.5				158			52			87	01/09/2015	15.32	-92.84	108	5.3		265	334		190			197	316
42	10/12/2011	15.33	-94.79	16	5.2		140								88	17/12/2015	15.76	-93.7	90	6.6		163							
43	20/12/2011	13.81	-93.43	15	5.1				211						89	14/06/2017	14.77	-92.08	113	7	465						116	274	
44	21/01/2012	14.74	-93.24	16	6	390	255	311	107	230		111		363	90	07/09/2017	14.85	-94.11	58	8.2	273	121	112		272	77			
45	16/02/2012	14.59	-92.92	25	5		291		129	239		85			Total records						10	44	30	57	43	20	24	22	11
46	20/02/2012	14.37	-93.14	16	5.2				148			116																	

* H represents focal depth.

Finally, to suppress site effects from the 261 records, with the ETF computed previously (red continuous line, Figure 3) and the estimated FAS for each record, we compute the deconvolution between the FAS for the nine sites and ETF in the frequency domain for this site, subtracting their respective site effect. The corresponding intensities (spectral acceleration and peak values) are estimated using random vibration theory (RVT) (i.e., Arciniega-Ceballos 1990; Reinoso and Ordaz 1999), which comprises the following steps: (1) de-amplifying the FAS by dividing them by the EHVSR obtaining a proxy of ETF; (2) multiplication of the spectrum by the oscillator transfer function or by one if PGA is seek; (3) calculation of the moments m_0 and m_2 of the power density which are given by $m_k = \int_0^\infty \omega^k \, |A(\omega)|.^2 \, d\omega$; (4) estimate the root mean square in terms of m_0 and the strong motion

duration, D, for each event; (5) computation of the peak factor F_p, according to RVT, in terms of the number of extrema N occurring during the duration D and from the moments by means of $N=(D/\pi)(m_2/m_0)^{0.5}$, and get the expected peak by multiplying the FAS by F_p. The peak factor is asymptotically given by $F_p = (2\ln N)^{0.5} + 0.577(2\ln N)^{-0.5}$. Regarding D, we use the expression developed by Herrmann (1985), $D = f_c^{-1} + 0.05R$ where f_c= corner frequency (in Hz) and the R=distance (in km). As for response spectral ordinates, both the oscillator transfer function and the additional duration have to be accounted for (see e.g. Boore, 1983).

In this way, the estimated ground motion intensities (e.g. acceleration response spectra) for each event and site will be essentially free of site effect. In Figure 4 this reduction is illustrated for the July 6th, 2007 (M_w=6.2) event. The complex Fourier spectra were deconvolved by the corresponding average EHVSR (ETF) and then transformed back to time domain. The N-S accelerograms of the nine stations are displayed in the left panel. The corresponding distance and PGA are indicated. In the right panel the recordings with suppressed site effect are displayed (as if the corresponding stations were located in hard rock). This suppression gives significantly lower PGA values (for TAJN a factor of 7.5 was obtained). We claim that the use of average EHVSR may be adequate to correct GMPE for site effects, leading to a more realistic attenuation model.

Peak ground accelerations (PGA) are obtained from these corrected records. Also, response spectra with 5 % critical damping are obtained for 24 structural periods ranging between 0.3 and 40 Hz. Finally, peak ground velocities are obtained by integrating these recordings after correcting them for base line (Boore, 2005) and band-pass filtering between 0.3 and 40 Hz.

Each parameter (i.e., PGA, PGV, or the spectral ordinates) is separately calculated for both horizontal components, then the quadratic mean is obtained from both ortogonal components (Boore, 2005). Other alternatives would include the geometric mean, or other no geometrical means (Boore, 2010). We used the quadratic vector mean as it is a common practice in the development of attenuation models, since from the physics point of view it is more rational than other means. All recordings were processed in the same form.

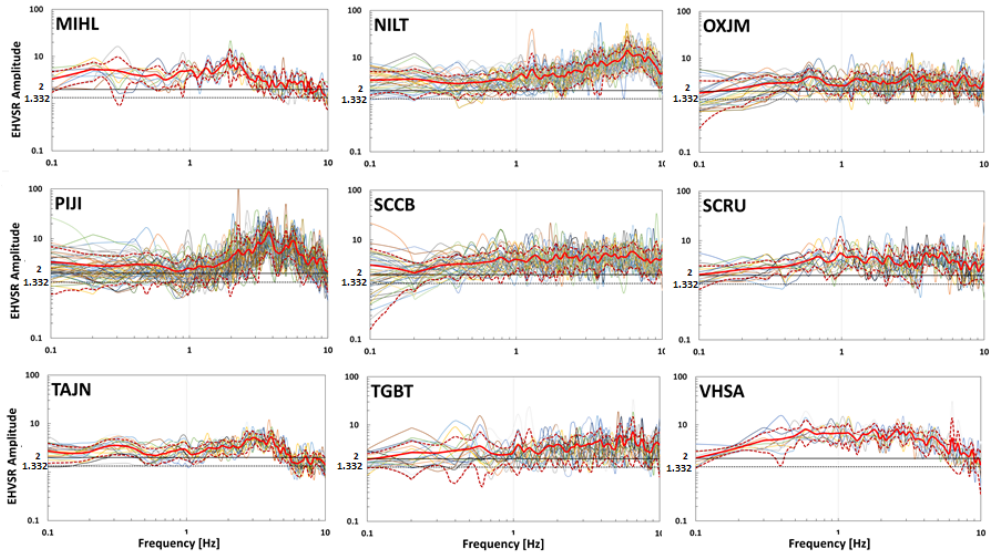

Figure 3. Earthquake horizontal to vertical spectral ratios EHVSR at the nine studied stations. In thin of colours continuous lines, the quadratic mean spectral ratios (continuous red lines) of each earthquake are plotted in log-log scale (dashed red lines: average ± one standard deviation). The trends are clear and the averages at each station, depicted in red, are assumed to represent the site effect. The value of two suggested by SESAME (2000), continuous line, and the theoretical H/V in a Poissonian half-space are given as reference (discontinuous line).

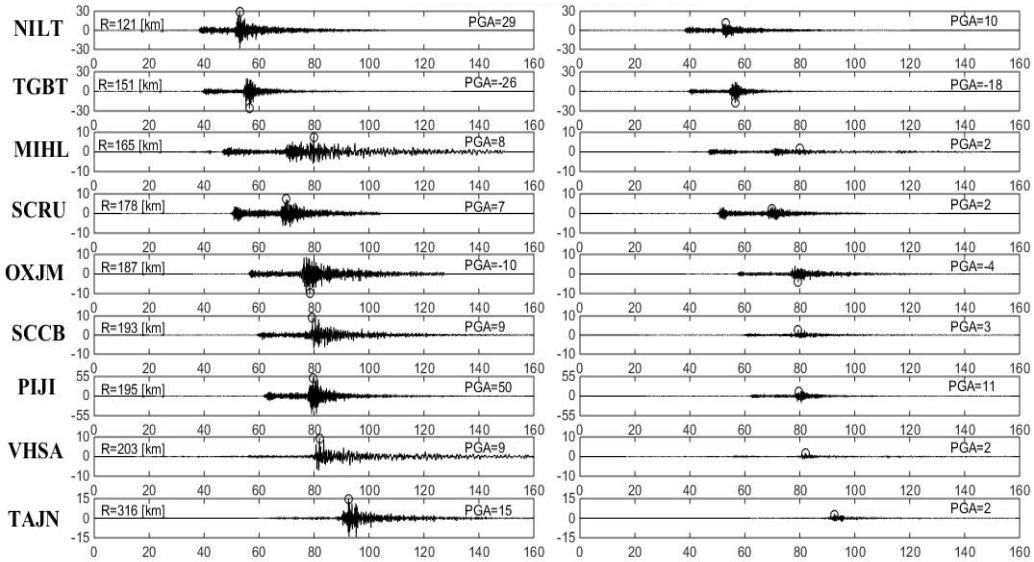

Figure 4. Example of site effects correction for a Mw=6.2 event of July 6th , 2007 for the studied stations. Left panel depicts the N-S accelerations indicating the epicentral distance and the PGA in gals (cm/s2). The right panel shows the time series with the site effects removed with the procedure described herein.

REGRESSION ANALYSIS

To estimate the spectral accelerations with a damping of 5 %, as well as the PGA and PGV, the regression analysis of the data set was made using the maximal verisimilitude method of one stage proposed by Boore (1993), which constitutes the most direct form to predict the response spectra of observed data. We use a simpler functional form proposed by Ordaz *et al.* (1989), and García-Soto and Jaimes (2017) to estimate the spectral ordinates, PGA, and PGV for seismic events from southeastern Mexico.

$$lnY(T) = \alpha_1(T) + \alpha_2(T) \cdot M_w + \alpha_3(T) \cdot lnR + \alpha_4(T)R + \varepsilon_1(T) \qquad (2)$$

where $Y(T)$ represents the horizontal spectral ordinate based on a quadratic mean of the horizontal components, T in seconds is the period of the single degree of freedom system, Mw is the moment magnitude, *R* is the closest distance from site to fault surface for larger events (Mw > 6.5) or the hypocentral distance for the rest, both in km, α_i are the coefficients estimated by the regression analysis, and ε_1 is the error estimation by assuming a normal distribution.

Noteworthy is that in previous studies (i.e., Arroyo, 2010; García-Soto and Jaimes, 2017) no important dependence with the focal depth was found, consequently it was not considered in excluded from this study. Even more, the quadratic mean was used since the use of the geometric mean and was the development of the attenuation relationship is slightly less conservative than the use of the quadratic mean to evaluate seismic risk (i.e., Hong and Goda, 2007). The horizontal geometric dispersion can be obtained as $G(R) = R^{\alpha_3(T)}$, where $\alpha_3(T)$ is the geometric attenuation coefficient, which controls the amplitude decay with the distance, R. By applying the natural logarithm to both sides of the last expression, it can be linearized as $ln\big(G(R)\big) = \alpha_3(T) \cdot lnR$, which corresponds to the third term of equation (2). In this study, it was considered that $\alpha_3(T)$ is very well constrained by seismic observations in intraplate events (i.e., Ordaz *et al.* 1994; Reyes, 1999; Jaimes *et al.* 2006; Garcia-

Soto and Jaimes, 2017). Further, by fixing the geometric dispersion coefficient at -0.5 for all the ordinates in both components (i.e., Ordaz *et al.*, 1994; Reyes, 1999; Jaimes *et al.*, 2006), unrealistic values are avoided (i.e., non-negative values of $\alpha_3(T)$,) that physically have no sense (Ordaz *et al.* 1994).

Results and Discussion

Regression Coefficients and Residuals

Regression coefficients, $\alpha_i(T)$, and the standard deviation $\sigma_i(T)$, were estimated for periods T between 0.1 and 10 s, for recordings of 4 groups: Group 1, considers all recordings without site effects; Group 2, includes the recordings with site effects; Group 3, comprises recordings of earthquakes with depths less than 80 km but without site effects; while Group 4, is constituted by recordings of earthquakes with depths less than 250 km and no corrected for site effects. Figure 5 shows, in a logarithmic scale, the values of the regression coefficients $\alpha_1(T)$, $\alpha_2(T)$ and $\alpha_4(T)$ for period values between 0.1 and 10 s. No differences significant are found between coefficients α_2 and α_4 among the 4 groups. However, coefficient α_1 of group 2 (which includes site effects) shows an evident divergence, from the others groups. Confirmation of the validity of the attenuation model is indicated by the standard deviation $\sigma_i(T)$obtained for the cases with and without site effects. Table 2 summarizes the regression coefficients $\alpha_i(T)$ and the standard deviation obtained from the analyzed recordings by considering the quadratic mean of the horizontal components.

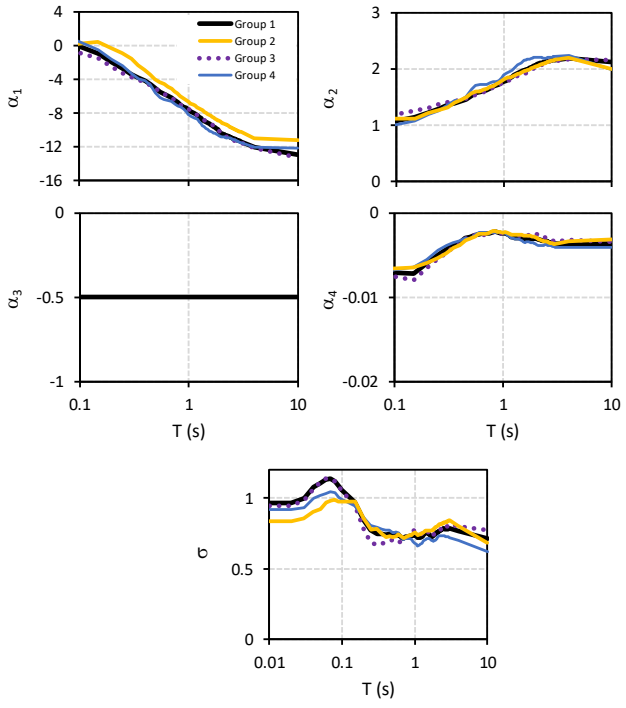

Figure 5.- Regression coefficients and natural logarithmic standard deviation logarithmic for horizontal components in the sites of Chiapas State, Mexico. a) Group 1: all records without site effects. B) Group 2 all records presenting

site effects, c) Group 3 including records with depths less than 80 km, and d) Group 4 with records with depths less than 250 km and no site effect.

For the purpose of this analysis, the residual is defined as:

$$\delta_i = ln(Y_i) - ln(\bar{Y}) \tag{3}$$

where $ln(Y_i)$ is the natural logarithm of i-eth observed value $Y_i$and $ln(\bar{Y})$ is the corresponding predicted value. The attenuation model in order to non-biased estimations, the residual must have a zero mean, and do not present any correlation with the regression model parameters, i.e., the magnitude (Mw) and distance R. Figure 6 shows the residuals δ_i obtained from the regression of the horizontal components as functions of magnitude (upper panel), and of the distance (lower panel) for PGA and spectral ordinates for T= 0.06, 0.5, and 1 s. These figures consider a) all recordings without site effects, b) all recordings with site effects, c) recordings from earthquakes with depths less than 80 km and without site effect, and d) recordings from earthquakes with depths less than 250 km and without site effects. These figures shows that the regression model is not biased neither towards magnitude nor distance. The tendency lines are shown with a thick line.

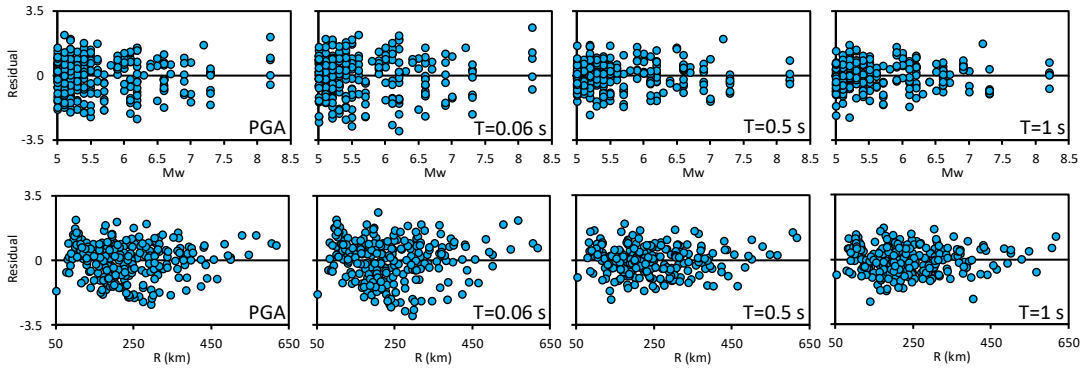

a)

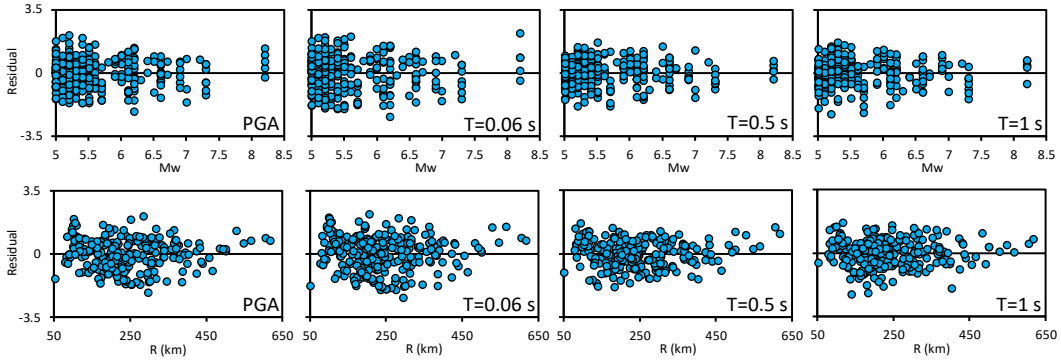

b)

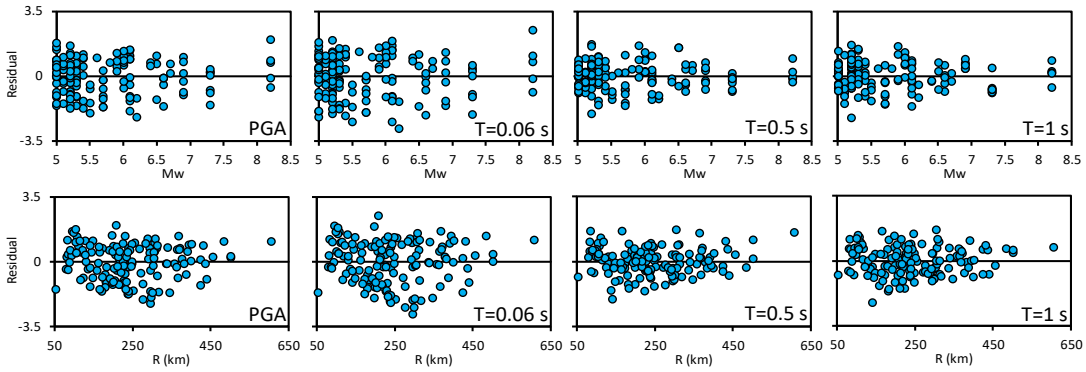

Figure 6. Residual values obtained from the regression of the horizontal components according to magnitude (upper part of panel), and with respect to distance (lower part of each panel) for peak ground acceleration (PGA) and spectral pseudoaceleration, Sa, at T values of 0.06, 0.5, and 1 s. Panel a comprises all records without site effect, panel b includes all records with site effect, panel c considers records with depths less than 80 km and without site effect. Finally, panel d corresponds to records with depth less than 250 without site effect.

Table 2.- Regression coefficients obtained for the horizontal components.

	Group 1				Group 2			
T (s)	α_1	α_2	α_4	α	α_1	α_2	α_4	α
0.01	-1.5508	1.1515	-0.0066	0.96	-1.1789	1.2033	-0.0057	0.84
0.02	-1.5518	1.1516	-0.0066	0.96	-1.1802	1.2036	-0.0057	0.84
0.04	-0.9102	1.1402	-0.0070	1.08	-0.8432	1.2014	-0.0062	0.90
0.06	0.0273	1.0727	-0.0077	1.13	-0.2829	1.1604	-0.0067	0.97
0.08	0.1705	1.0758	-0.0074	1.12	0.0004	1.1415	-0.0067	0.99
0.1	-0.0772	1.0803	-0.0071	1.06	0.2687	1.1119	-0.0065	0.98
0.2	-1.8836	1.2276	-0.0060	0.84	-0.3723	1.2176	-0.0060	0.85
0.3	-3.3412	1.3582	-0.0043	0.75	-1.5325	1.3277	-0.0048	0.78
0.4	-4.1157	1.4207	-0.0036	0.74	-2.8650	1.4583	-0.0039	0.72
0.5	-5.0784	1.5269	-0.0029	0.74	-3.9424	1.5641	-0.0031	0.72
0.6	-5.7386	1.5918	-0.0025	0.74	-4.5830	1.6097	-0.0025	0.74
0.7	-6.1632	1.6285	-0.0025	0.71	-5.0980	1.6559	-0.0025	0.72
0.8	-6.7363	1.6862	-0.0023	0.73	-5.6886	1.7072	-0.0022	0.73
0.9	-7.2001	1.7347	-0.0023	0.74	-6.1589	1.7580	-0.0022	0.74
1	-7.5814	1.7794	-0.0024	0.74	-6.6258	1.8121	-0.0023	0.76
1.1	-7.9202	1.8218	-0.0026	0.72	-6.9805	1.8454	-0.0024	0.74
1.2	-8.2500	1.8662	-0.0029	0.72	-7.2676	1.8767	-0.0026	0.74
1.3	-8.6025	1.9053	-0.0029	0.74	-7.5384	1.9029	-0.0027	0.76
1.4	-8.9040	1.9359	-0.0029	0.75	-7.8037	1.9253	-0.0026	0.77
1.5	-9.1855	1.9686	-0.0030	0.75	-8.0682	1.9535	-0.0026	0.77
1.6	-9.3861	1.9875	-0.0031	0.74	-8.2767	1.9731	-0.0027	0.77
1.7	-9.6182	2.0066	-0.0030	0.73	-8.5064	1.9932	-0.0027	0.77
1.8	-9.8511	2.0287	-0.0030	0.73	-8.7205	2.0161	-0.0028	0.78
1.9	-10.0840	2.0525	-0.0031	0.74	-8.8946	2.0317	-0.0028	0.79
2	-10.3230	2.0783	-0.0030	0.75	-9.0643	2.0470	-0.0029	0.80
2.1	-10.5020	2.1001	-0.0031	0.76	-9.2065	2.0651	-0.0031	0.81
2.2	-10.6030	2.1060	-0.0032	0.77	-9.3423	2.0806	-0.0032	0.81
2.3	-10.6940	2.1132	-0.0033	0.77	-9.4559	2.0931	-0.0033	0.82
2.4	-10.8300	2.1258	-0.0033	0.78	-9.5928	2.1075	-0.0033	0.82
2.5	-10.9520	2.1373	-0.0033	0.78	-9.7241	2.1211	-0.0034	0.83
2.6	-11.0450	2.1454	-0.0034	0.78	-9.8505	2.1347	-0.0035	0.83
2.7	-11.1190	2.1487	-0.0035	0.78	-9.9396	2.1407	-0.0035	0.83
2.8	-11.2020	2.1547	-0.0036	0.78	-10.0500	2.1501	-0.0036	0.83
2.9	-11.2640	2.1582	-0.0036	0.78	-10.1420	2.1582	-0.0036	0.84
3	-11.3170	2.1597	-0.0037	0.78	-10.2080	2.1620	-0.0037	0.84
4	-12.0000	2.1999	-0.0036	0.76	-11.0170	2.2074	-0.0034	0.80
10	-12.9230	2.1268	-0.0037	0.71	-11.2190	2.0019	-0.0031	0.68
PGA	-1.5528	1.1517	-0.0066	0.96	-1.1804	1.2035	-0.0057	0.84
PGV	-7.9782	1.5989	-0.0045	0.69	-5.2675	1.3045	-0.0015	0.72

*Coefficient α_3 was fixed at -0.50 for the horizontal components.

Table 2 (continuation)

	Group 3				Group 4			
T (s)	α_1	α_2	α_4	α	α_1	α_2	α_4	α
0.01	-2.4021	1.2740	-0.0068	0.94	-0.6243	1.0278	-0.0066	0.92
0.02	-2.4032	1.2741	-0.0068	0.94	-0.6255	1.0280	-0.0066	0.92
0.04	-1.9104	1.2753	-0.0070	1.07	0.2756	0.9883	-0.0072	1.00
0.06	-0.9018	1.2115	-0.0081	1.14	0.8888	0.9587	-0.0074	1.03
0.08	-0.7548	1.2182	-0.0079	1.12	1.0427	0.9535	-0.0071	1.04
0.1	-0.8250	1.1929	-0.0075	1.05	0.4859	1.0117	-0.0068	0.99
0.2	-2.4394	1.3187	-0.0066	0.77	-1.6079	1.1957	-0.0055	0.86
0.3	-3.7200	1.4183	-0.0047	0.67	-3.2780	1.3628	-0.0039	0.79
0.4	-4.3712	1.4573	-0.0038	0.68	-4.1248	1.4403	-0.0034	0.77
0.5	-5.0664	1.5030	-0.0027	0.70	-5.5705	1.6473	-0.0030	0.75
0.6	-5.6933	1.5746	-0.0027	0.69	-6.4074	1.7271	-0.0023	0.75
0.7	-6.1841	1.6204	-0.0026	0.70	-6.6099	1.7249	-0.0024	0.71
0.8	-6.7908	1.6798	-0.0023	0.73	-7.0916	1.7708	-0.0023	0.71
0.9	-7.2440	1.7291	-0.0022	0.75	-7.4292	1.7927	-0.0023	0.70
1	-7.4932	1.7537	-0.0024	0.77	-8.1831	1.8992	-0.0023	0.68
1.1	-7.8381	1.7911	-0.0025	0.76	-8.5043	1.9452	-0.0026	0.66
1.2	-8.2195	1.8408	-0.0027	0.74	-8.7325	1.9763	-0.0030	0.67
1.3	-8.5256	1.8707	-0.0028	0.76	-9.1991	2.0367	-0.0031	0.69
1.4	-8.7945	1.8908	-0.0027	0.77	-9.6278	2.0958	-0.0031	0.71
1.5	-9.0462	1.9132	-0.0027	0.77	-9.9370	2.1393	-0.0034	0.71
1.6	-9.2658	1.9325	-0.0028	0.74	-10.1650	2.1670	-0.0035	0.71
1.7	-9.5299	1.9576	-0.0027	0.73	-10.3090	2.1700	-0.0034	0.70
1.8	-9.7789	1.9782	-0.0026	0.74	-10.4910	2.1886	-0.0035	0.69
1.9	-10.0690	2.0087	-0.0026	0.75	-10.6570	2.2050	-0.0036	0.70
2	-10.3500	2.0384	-0.0025	0.76	-10.7930	2.2171	-0.0036	0.72
2.1	-10.5730	2.0661	-0.0026	0.77	-10.8310	2.2162	-0.0038	0.72
2.2	-10.6890	2.0764	-0.0026	0.77	-10.8720	2.2093	-0.0038	0.73
2.3	-10.8370	2.0959	-0.0028	0.78	-10.8630	2.1960	-0.0039	0.73
2.4	-11.0080	2.1167	-0.0029	0.79	-10.9130	2.1914	-0.0038	0.73
2.5	-11.1280	2.1300	-0.0029	0.80	-11.0370	2.2001	-0.0038	0.73
2.6	-11.2220	2.1403	-0.0031	0.80	-11.1400	2.2076	-0.0038	0.73
2.7	-11.3120	2.1481	-0.0032	0.80	-11.1990	2.2063	-0.0038	0.73
2.8	-11.3780	2.1511	-0.0032	0.80	-11.3060	2.2163	-0.0039	0.72
2.9	-11.4150	2.1518	-0.0033	0.81	-11.3910	2.2223	-0.0040	0.73
3	-11.4340	2.1479	-0.0034	0.82	-11.4980	2.2325	-0.0040	0.72
4	-12.0980	2.1843	-0.0032	0.80	-12.0520	2.2499	-0.0041	0.70
10	-13.1860	2.1597	-0.0034	0.77	-12.1180	2.0009	-0.0041	0.62
PGA	-2.4043	1.2743	-0.0068	0.94	-0.6286	1.0285	-0.0066	0.92
PGV	-8.4826	1.6581	-0.0045	0.68	-7.5498	1.5644	-0.0047	0.65

**Coefficient α_3 was fixed at -0.50 for the horizontal components.

COMPARISON WITH OTHER STUDIES

To the author's knowledge, there are no GMPEs in the region under study, which makes the outcome more necessary to compute the seismic hazard in the region. For that reason, the Figure 7 compares the attenuation model obtained in this study (for magnitudes Mw of 5.5, 6.5, and 7.5) with those of García *et al.*, (2005), Arroyo *et al.*, (2010) and García-Soto and Jaimes (2017), based on earthquakes located at the Pacific Ocean coasts (discontinuous lines). Attenuation models obtained in this study present a slower decay than previous ones, and models that include site effects (yellow lines) present larger amplitudes than those without site effects (black lines).

Previous attenuation models are clearly different to the attenuation models here presented for southeastern Mexico. These differences could be due to the fact that in southeastern Mexico earthquakes attain depths up to about 243 km, while in the Guerrero coast (southern Mexico) depths are less than 80 km. In general, models by Arroyo *et al.* (2010) and Garcia-Soto and Jaimes (2017) follow a similar pattern in all cases, and for Sa, for T = 0.5 s and 1 s, they decay almost in the same way as the model by Garcia (2005) for Mw 5.5 and 6.5. For PGA, the model by Garcia (2005) present larger amplitudes (for the three magnitudes) than those by the models by Arroyo *et al.* (2010) and Garcia-Soto and Jaimes (2017). In particular, the PGA models corrected for site effects (obtained in this study) have smaller amplitudes than the models by Arroyo *et al.* (2010) and Garcia-Soto and Jaimes (2017) only for distances smaller than 130, 90 and 50 km for Mw 5.5, 6.5 and 7.5, respectively. On the contrary, Sa models corrected for site effects present lower amplitudes than those of the previous models. However, and as it was expected, the corresponding models that include site effects (yellow lines) present the largest amplitudes at all distances. In other words, a model comprising site effects presents overestimated values.

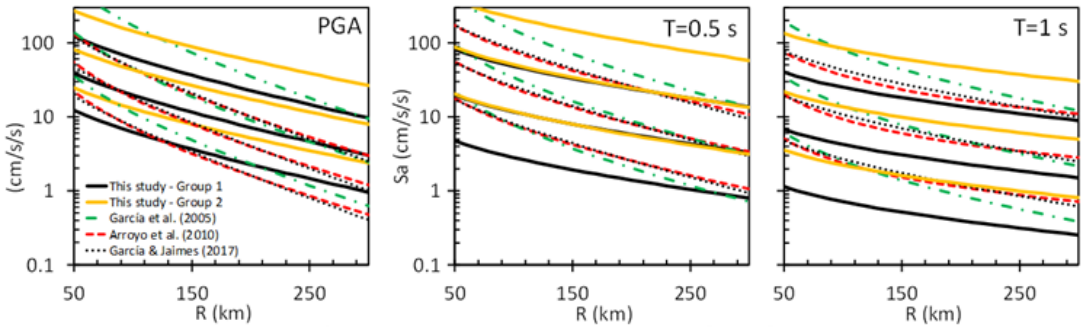

Figure 7. Regression curves for the horizontal component for PGA and spectral pseudo-acceleration, Sa, for periods of 0.5 and 1 s for earthquakes with magnitudes Mw of 5.5, 6.5, and 7.5. Group 1 comprises regression of all records without site effect, while group 2 includes all records with site effect.

CONCLUSIONS

We present an attenuation model for strong motion for southeastern Mexico which is approximately free of local amplification. This means that the GMPE thus obtained can be regarded as appropriate for firm ground. This was accomplished using average EHVSR to construct an empirical transfer function (ETF) for each site to perform a spectral deconvolution on observed records. A statistical regression model was adjusted to construct the corrected GMPE. The model is built as a function of the magnitude and distance from 86 seismic events with magnitudes $5.0 \leq M_w \leq 8.2$, and distances $52 \leq R \leq 618$ km recorded at the states of Chiapas, Oaxaca, Tabasco and Veracruz.

This study shows a practical, approximate approach to remove the site effect in the ground motion attenuation models, the so called GMPE. Otherwise, the seismic intensities could be overestimated. Such is the case in the current values of regulatory norms for the study region. We approximately suppress site effects at the accelerometric stations which provide data to construct attenuation models using the average EHVSR. The aim is to obtain reasonable seismic intensities without the bias induced by local site effects.

ACKNOWLEDGEMENTS

We thank H. Kawase, S. Matsushima and F. Nagashima for the careful reading of the manuscript and many useful suggestions. Help from J. E Plata and G. Sánchez N. and their team from USI–Instituto de Ingeniería, Universidad Nacional Autónoma de México (UNAM) was crucial to locate some references. Our appreciation to all the technicians who manage, analyze, and give maintenance to the accelerometric network of the Instituto de Ingeniería of the Universidad Nacional Autónoma de México (II-UNAM) installed in the states of Chiapas, Oaxaca, Tabasco, and Veracruz, and that from the SSN. A. L. Ruiz-Gordillo, J. A. Martínez-González and R. Vázquez-Rosas helped us in software work. Thanks are given to J. E. Plata and G. Sánchez of USI, II-UNAM for their multifarious help. Partial support by DGAPA-UNAM, México, under Projects IN100917 and IN107720, is greatly appreciated.

REFERENCES

Arciniega-Ceballos, A., 1990, Modelo semi-empírico para estimar espectros de respuesta sísmicos en el valle de México, Thesis, Universidad Nacional Autónoma de México.

Arroyo, D., García, D., Ordaz, M., Mora, M. A. and Singh, S. K., 2010, Strong ground-motion relations for Mexican interplate earthquakes, *J. Seismol*, 14(4), 769–785.

Baena-Rivera, M., Perton, M., and Sánchez-Sesma, F. J., 2016, Surface waves retrieval from Generalized Diffuse Fields in 2D synthetic models of alluvial valleys, *Bulletin of the Seismological Society of America*, 106, 2811–2816, doi: 10.1785/0120160084.

Boore, D. M., 1983, Stochastic simulation of high-frequency ground motions based on seismological models of the radiated spectra, *Bulletin of the Seismological Society of America*, 73, 1865-1894

Boore, D. M., 2005, On pads and filters: Processing strong-ground motion data, Bulletin of the Seismological Society of America, 95(2), 745–750.

Boore, D. M., 2010, Orientation-independent, nongeometric-mean measures of seismic intensity from two horizontal components motion, *Bulletin of the Seismological Society of America*, 100(4), 1830-1835.

Carpenter, N. S., Wang, Z., Woolery, E.W. and Rong, M., 2018, Estimating Site Response with Recordings from Deep Boreholes and HVSR: Examples from the Mississippi Embayment of the Central United States, *Bulletin of the Seismological Society of America*, 108(3A), 1199-1209, doi: 10.1785/0120170156.

Finn, W. D. L., 1991, Geotechnical engineering aspects of microzonation, *Proc, Fourth Int, Conf. on Seismic Zonation*, Stanford, California, I, 199-259.

Figueroa J. A., 1973, Sismicidad en Chiapas, Series del Instituto de Ingeniería, Universidad Nacional Autónoma de México, SID 316, pp. 50.

Figueroa, J., Lomnitz, C., Dawson, A., Meli, R. and Prince, J., 1975, Los sismos de julio-octubre de 1975 en el Municipio de Chiapas de Corzo, Chiapas, Instituto de Ingeniería, Universidad Nacional Autónoma de México, Reporte interno, pp. 40.

García, D., Singh, S.K., Herráiz, M., Ordaz, M. and Pacheco, 2005, Inslab earthquakes of Central Mexico: Peak ground-motion parameters and response spectra, *Bull. Seismol. Soc. Am*, 95(6), 2272–2282.

García, D., 2007, Estimación de parámetros del movimiento fuerte del suelo para terremotos intraplaca e instraslab en México central, Ph D.Thesis, Madrid: Universidad Complutense.

García-Soto, A. D., and Jaimes, M. A., 2017, Ground-Motion Prediction Model for Vertical Response Spectra from Mexican Interplate Earthquakes. *Bulletin of the Seismological Society of America*, 107, 887-900.

Gutiérrez, C. and Singh, S. K., 1992, A site effect study in Acapulco, Guerrero, Mexico: comparison of results, *Bull. Seism. Soc. Am*,78, 42-63.

Hennino, R., Tregoures, N., Shapiro, N.M., Margerin, L., Campillo, M., Van Tiggelen B.A. and Weaver, R. L., 2001, Observation of equipartition of seismic waves, Phys. Rev. Lett., 86, 3447–3450. doi: 279 10.1103/*Phys Rev Lett.* 86.3447.

Hermann, R. B., 1985, An extension of random vibration theory estimates of strong ground motion to large distance, *Bulletin of the Seismological Society of America*, 7, 157-171.

HIC-AL, 2017, Reporte periodístico del 15 de septiembre del 2017, realizado por el Grupo de trabajo sobre producción y gestión social de Hábitat-HIC-AL, 2017.

Hong, H., and Goda, K., 2007, Orientation-dependent ground-motion measure for seismic-hazard assessment, *Bull. Seismol. Soc. Am*, 97(5), 1525 - 1538.

Jaimes, M. A., Reinoso, E., and Ordaz, M., 2006, Comparasion of methods to predict response spectra at instrumented sites given the magnitude and distance of an earthquake, *Journal of Earthquake Engineering*, 10(6), 887-902.

Joyner, W. B., and Boore, D. M., 1993, Methods for regression analysis of strong-motion data, *Bulletin of the Seismological Society of America*, 83**(**2), 469–487.

Kawase, H., Sánchez-Sesma, F. J. and Matsushima, S., 2011, The optimal use of horizontal-to-vertical (H/V) spectral ratios of earthquake motions for velocity structure inversions based on diffuse field theory for plane waves, *Bulletin of the Seismological Society of America*, 101(5), 2001-2014, doi: 10.1785/0120100263.

Kawase, H. Mori, Y. and Nagashima F., 2018, Difference of horizontal-to-vertical spectral ratios of observed earthquakes and microtremors and its application to S-wave velocity inversion based on the diffuse field concept, *Earth, Planets and Space*, 70, 32p, https://doi.org/10.1186/s40623-017-0766-4

Kostoglodov, V., and Pacheco, J., 1999, Cien años de sismicidad en México. Ciudad de México: Instituto de Geofísica, Universidad Nacional Autónoma de México.

Lachet, C. and Bard, P. Y., 1994, Numerical and theoretical investigations on the possibilities and limitations of Nakamura's technique, *J. Phys. Earth*., 42, 377-397.

Lermo, J. and Chávez-García, F. J., 1993, Site effect evaluation using spectral ratios with only one station. *Bulletin of the Seismological Society of America*, 83, 1574-1594.

Lermo, J. and Chávez-García, F. J., 1994a, Site effect evaluation at Mexico City. Dominant period and relative amplification from strong motion and microtremors records, *Soil Dyn. & Earthq. Eng*., 13, 413-423.

Lermo, J. and Chávez-García, F. J., 1994b, Are microtremors useful in site response evaluation? *Bull. Seism. Soc. Am*., 84, 1350-1364.

Margerin, L., 2009, Generalized eigenfunctions of layered elastic media and application to diffuse fields, *J. Acoust. Soc. Am*., 125, 164-174.

Margerin, L., Campillo, M., Van Tiggelen, B. A., and Hennino, R., 2009, Energy partition of seismic coda waves in layered media: Theory and application to Pinyon Flats Observatory, *Geophys. J. Int*., 177, 571–585.

Martínez-González, J.A., Lermo J., Sánchez-Sesma, F.J., Angulo-Carrillo, J., Valle-Orozco, R., Ordoñez-Alfaro, J., Pérez-Rocha L.E., 2012, Effects of the subsidence on the changes of dominant periods of soils within Mexico City Valley. In: 15th World Conference on Earthquake Engineering id.3598.

Martínez-González, J.A., Lermo J., Vergara-Huerta, F., Ramos-Pérez, E., 2015, Avances en la zonificación sísmica de la ciudad de México y zona de Chalco, Edo. de Mex., propuesta de nuevo mapa de periodos dominantes para las NTC para diseño por sismo del reglamento del D.F. In: XX Congreso Nacional de Ingeniería Sísmica, Sociedad Mexicana de Ingeniería Sísmica.

Nakamura, Y., 1989, A method for dynamic characteristics estimation of subsurface using microtremor on ground surface. Quarterly Report of the Railway Technical Research Institute. QR RTRI 30 (1), 25-33.

Ordaz, M., Jara, J. and Singh, K. S., 1989, Riesgo sísmico y espectros de diseño en el EstadodeGuerrero, Memoria del VIII Congreso Nacional de Ingeniería Sísmica, México, D40-D56.

Ordaz, M., Singh, S. K., and Arciniega, A., 1994, Bayesian attenuation regressions: an application to Mexico City. *Geophysical Journal International*, 117(2), 335-344.

Pérez-Yañez, C., Ramírez-Guzmán, L., Ruíz G.A.L., Delgado, D.R., Macias, C.M.A., Sandoval, G. H., Quiróz R. A. (14-19 de Diciembre de 2010), Strong Ground Motion Database System for Mexican Seismic. San Fransisco: AGU Fall Meeting.

Rebollar, C. J., Quintanar, L., Yamamoto, J., and Uribe, A., 1999, Source Process of the Chiapas, Mexico, Intermediate-Depth Earthquake (Mw=7.2) of 21 October 1995, *Bulletin of the Seismological Society of America*, 89, 348-358.

Reinoso, E., and Ordaz, M., 1999, Spectral ratios for Mexico City from free-field recordings, *Earthquake Spectra*, 15, 273-295.

Reyes, C., 1999, El estado límite de servicio en el diseño sísmico de edificios, Ph.D. Tesis, UNAM, México.

Sánchez-Sesma, F. J., and Campillo, M., 2006, Retrieval of the Green's function from cross-correlation: The canonical elastic problem, *Bulletin of the Seismological Society of America*, 96, 1182-1191.

Sánchez-Sesma, F. J., Pérez-Ruiz, J. A., Campillo, M. and Luzón, F., 2006, Elastodynamic 2D green function retrieval from cross-correlation: Canonical inclusion problem, *Geophys. Res. Lett.*, 33, L13305-1-6.

Sánchez-Sesma, F. J., Pérez-Ruiz, J. A., Luzón, F., Campillo, M., and Rodríguez-Castellanos, A., 2008, Diffuse fields in dynamic elasticity, *Wave Motion*, 45, 641-654.

Sánchez-Sesma F.J., Weaver R.L., Kawase H., Matsushima S., Luzón F., and Campillo M., 2011a, Energy Partitions among elastic waves for dynamic surface loads in a semi-infinite solid, *Bulletin of the Seismological Society of America*, 101(4), 1704-1709, doi: 10.1785/0120100196.

Sánchez-Sesma, F. J., Rodríguez, M., Iturrarán-Viveros, U., Luzón, F., Campillo, M., Margerin, L., García-Jerez, A., Suárez, M., Santoyo, M. A. & Rodríguez-Castellanos, A., 2011b, A theory for microtremor H/V spectral ratio: application for a layered medium, *Geophys. J. Int.*, 186, 221-225. doi: 10.1111/j.1365-246X.2011.05064.

SSN, 1993, Reporte de sismo:10 de Septiembre de 1993 (Mw7.2), Servicio Sismologico Nacional (SSN), Instituto de Geofísica, Universidad Nacional Autónoma de México, pp 5.

SSN, 2012, Reporte de sismo: Sismo del día 7 de Noviembre de 2012, Chiapas (Mw7.3), Servicio Sismologico Nacional (SSN), Instituto de Geofísica, Universidad Nacional Autónoma de México, pp 5.

SSN, 2017, Reporte Especial: Sismo de Tehuantepec, 7 de septiembre de 2017 (M 8.2), Servicio Sismologico Nacional (SSN), Instituto de Geofísica, Universidad Nacional Autónoma de México, pp 11.

Weaver, R. L., 1982, On diffuse waves in solid media, *Journal of the Acoustic Society of America*, 71, 1608-1609.

Weaver, R. L., 1985, Diffuse elastic waves at a free surface, *Journal of the Acoustic Society of America*, 78, 131-136.

Weber, B., Schaaf, P., Valencia, V. A., Iriondo, A., and Ortega-Gutierrez, F., 2006, Provenance ages of late Paleozoic sandstones (Santa Rosa Formation) from the Maya Block, SE México: implications on the tectonic evolution of western Pangea, *Revista mexicana de ciencias geológicas*, 23(3), 262-276.

Ye, L., Lay, T., Bai, Y., Cheung, K. F., & Kanamori, H., 2017, The 2017 Mw 8.2 Chiapas, Mexico, earthquake: Energetic slab detachment. *Geophysical Research Letters*, 44, 11,824–11,832. https://doi.org/10.1002/2017GL076085.

Geofísica Internacional (2020) 59-4: 273-284.

Original paper

THE RECOGNITION OF THE REMNANTS OF THE ROYAL ROAD OF THE INTERIOR LAND USING HIGH-RESOLUTION MULTISPECTRAL SATELLITE IMAGES

Jorge Lira*[1] and Pedro López[2]

Received: November 12, 2019; accepted: September 1, 2020: published online: October 1, 2020

RESUMEN

Los españoles construyeron el Camino Real de Tierra Adentro en los tiempos de la colonia de México. Tal camino corría entre la Ciudad de México y Santa Fe, en Nuevo México, USA. Algunos remanentes aun sobreviven en México, pero su localización, longitud y condición no son bien conocidas. Por medio de trabajo de campo y de una investigación de los registros dejados por los españoles, se identificaron tres segmentos del Camino Real. Se adquirieron tres imágenes multiespectrales de alta resolución del satélite Pleiades. Tales imágenes cubren tres zonas donde fueron identificados los segmentos del Camino Real y se llevó a cabo un trabajo de campo. Debido a la degradación, los segmentos del Camino Real muestran bajo contraste con respecto al entorno pero una textura distintiva. Se aplicó un procedimiento de realce y agudizamiento a las imágenes con base al operador Vectorial Laplaciano y al análisis de componentes principales (ACP). Tal procedimiento realza la textura y los bordes de los segmentos del Camino Real. Un compuesto RGB falso color formado por el operador Laplaciano, la primera componente principal y la banda 4, produjo una imagen donde los segmentos del Camino Real son claramente observados. Por medio de trabajo de campo se identificaron las coordenadas y las condiciones de los segmentos del Camino Real.

PALABRAS CLAVE: Camino Real, Arqueología, sensores remotos, procesamiento de imágenes.

ABSTRACT

The Spaniards built the Royal Road of the Interior Land in the colonial times of Mexico. Such a road ranged between Mexico City and Santa Fe, New Mexico, USA. Some remnants still survive in Mexico, but their geographic location, position, length and condition are not well known. By means of fieldwork and a search of historic records left by the Spaniards, three segments of the Royal Road were identified. Three high-resolution multispectral images from the Pleiades satellite were acquired. Such images cover three zones where the Royal Road segments were located, and fieldwork was carried out. Due to degradation, the segments of the Royal Road show a low contrast with respect to the surroundings but a distinctive texture. A procedure of enhancement and sharpening was applied to the images based on the Vector Laplacian operator and Principal Component Analysis (PCA). Such a procedure enhances the texture and the edges of the Royal Road segments. An RGB false color composite formed by the Laplacian operator, the first principal component, and band 4, produced an image where the Royal Road segments are clearly observed. By means of fieldwork, the geographic coordinates and condition of the Royal Road segments were identified.

KEYWORDS: Royal Road, Archaeology, Remote Sensing, Image Processing.

*Corresponding author: jlira@geofisica.unam.mx

[1] Instituto de Geofísica
Universidad Nacional Autónoma de México,
04510, México DF

[2] Escuela Nacional de Antropología e Historia,
14030, México DF

INTRODUCTION

The Royal Road of the Interior Land ranged from Mexico City to Santa Fe, New Mexico, USA. Such a road was a rugged trail and, in some segments, a dangerous route running close to 3,000 kilometers in length. This road was in service for close to three centuries, from 1598 to 1882. In that time, the Royal Road was used for the transit of settlers, to transport goods and information, crops, livestock, and crafts, to several provinces of greater Mexico.

After independence from Spain in 1821, the northern frontier of Mexico was opened up to foreign trade. A new trail from Missouri to Santa Fe was constructed. The City of Santa Fe, New Mexico, quickly became the destination for a steady stream of traders carrying goods. For the next 60 years, the Royal Road, linked to the Santa Fe Trail, became an essential communication path between the growing economies of the United States and Mexico.

The detailed accounts of the expeditionary Juan de Oñate to Santa Fe set the foundations for the determination of the path of the Royal Road (Moorhead, 1995). The city of Santa Fe became the destination of a supply caravan that traversed a journey of 3,000 kilometers that iniciated in Mexico City. The Camino Real was the main trail that supported the displacement of the caravan.

By means of the Royal Road, the foundation of haciendas, bridges, forts and presidios, to protect roads and religious missions, was undertaken. Some segments of the Royal Road were paved, and are associated with churches, missions, farms and bridges. Nevertheless, it should be noted, that much of this heritage has been destroyed by the passage of time and by human intervention. Currently, all prospecting work is based on the registration of traces of some original sections.

In 1972 the Federal Law on Monuments and Archeological Sites, Artistic and Historic, promulgated a law that set an important ground for the identification and preservation of the Royal Road of the Interior Land (Diario Oficial, 1972; Gómez Arriola (eds.), 2012; Comer and Harrower, 2013).

Remote sensing techniques have been used to identify archaeological features. A number of publications account for the research done in archaeology using remote sensing techniques (Staski, 1998; Wiseman and El-Baz (eds.), 2007; Parcak, 2009; Tapete and Cigna, 2016; Hanson and Oltean, 2013).

Jackson (2006) provides a detailed description of the remnants of the Royal Road in New Mexico. Apparently, the Royal Road shows a better preservation in New Mexico than in Mexico. Such a description continues south of the border from El Paso del Norte (Ciudad Juarez) until Mexico City. The description includes the features associated to the Royal Road such as churches chapels, bridges and haciendas.

Preston and co-workers (1998) provide a detailed and colorful account of the exploration of the Royal Road. Preston and co-workers traversed the Royal Road by foot and by horse and provided a beautiful description of the landscapes they encountered.

In this research, it was assumed that the remnants of the Royal Road are observable in high-resolution satellite images and detectable by the use of enhancement and sharpening procedures (Lira and Rodríguez, 2014). A set of high-resolution multispectral images of central Mexico were acquired from the Pleiades Satellite. Efforts were concentrated on the existence of reported tracks in central Mexico, and fieldwork was carried out to confirm the findings of the Royal Road, derived by means of the processing of the high-resolution images.

The objectives of the present research are (i) To show that remote sensing techniques, applied to high-resolution multispectral satellite images, are able to identify segments of the

Royal Road, (ii) to stress the importance of having reliable techniques to help the preservation of this important cultural heritage, (iii) and to identify the actual aspect and level of degradation of such segments. To fulfill the objectives of this research, three tasks were developed. The enhancement of the edges of the Royal Road segments by means of the Principal Component Analysis. In addition, the enhancement of the texture of the segments by means of the Vector Laplacian. The third task was the fieldwork to assess the state of preservation of the segments of the Royal Road.

Materials and Methods

1 Materials

The set of high-resolution images cover three segments of the path of the Royal Road in the State of Aguascalientes and the State of Zacatecas (Moorhead, 1995; Gomez Arriola, 2012; Jackson, 2006; Preston, *et al.*, 1998). Basic technical details of the images are provided in Table 1. By means of fieldwork, information on the known tracks of the Royal Road with geographic coordinates were also acquired (Table 2). A SPOT 6 multispectral image was used to define the three study areas of the Royal Road segments. An RGB false color composite was prepared to show the areas of study where geographic features are identified (Figure 1a, 1b, 1c).

Several satellite platforms acquire high-resolution multispectral images of the Earth surface such as Orbview, GeoEye and Pleiades among others. An analytical task was developed to determine a suitable pixel size required to produce a clear identification of the segments of the Royal Road. The task indicated that a pixel of 30 - 50 cm was needed. Then a thorough search was carried out for images of such a pixel size with cloud-free view. The images of the Pleiades sensor were the only available for the three sites selected in this research.

The high-resolution images from the Pleiades 1A, B Satellite carry a pixel of 1.5 x 1.5 m2 in multispectral mode and a pixel of 0.5 x 0.5 m2 in panchromatic mode (Table 1). The Pleiades images were purchased from Earth Observing System (@CNES (2017)), Distribution Airbus DS).

2 Methods

2.2 Enhancement and sharpening

A selected set of high-resolution images was considered for the recognition of the Royal Road. The criterion for such selection was to consider the images that cover a portion of the Royal Road whose existence in central Mexico is known with certainty. Another criterion was to acquire cloud-free images (Table 1). However, the knowledge about the tracks of the Royal Road is a guess; the exact geographical location of such tracks is not well known. The actual condition of the Royal Road was evaluated by visual inspection of published photos (Jackson, 2006; Moorhead, 1995; Preston *et al.*, 1998; Gómez Arriola (eds.), 2012).

A fusion of the multispectral image with the panchromatic image was applied in a procedure known as pan sharpening. The pan sharpening process produced a multispectral image with a pixel of 0.5×0.5 m^2 (Table 1). The pan sharpening procedure generates a multispectral image with a pixel the size of the panchromatic band. In addition, this procedure preserves the spectral response of the scene enabling further analysis of the multispectral image.

The width of the known segments of the Royal Road is between 3 -10 meters. The contrast between the Royal Road and its surroundings is low. However, the texture of the Royal Road is noticeably different from the adjacent field. The Vector Laplacian operator (Lira and Rodriguez, 2014) was applied to the resulting image generated by the pan sharpening procedure to enhance the texture of the Royal Road. The Principal Component Analysis (PCA) was applied to such images to enhance the edges of the Royal Road. The Laplacian and the first principal component produced images such that the enhancement and definition of the edges of the Royal Road segments were achieved. Therefore, the Royal Road segments were identifiable in the enhanced images. Details of the Laplacian, the PCA and the spectral response of soil and vegetation can be found in Lira (2010; 2011). A block diagram shows the rationale of the enhancement and sharpening process (Figure 2). An RGB false color composite with the Laplacian, the first principal component, and the band 4 was prepared (Figures 3, 5, 7). In this RGB, the Laplacian enhances the texture of the road, the first principal component enhances the edges of the road and band 4 enables the difference between soil and vegetation. The next two sections provide details on the Laplacian and the principal component analysis.

2.3 Vector Laplacian

Let $\mathbf{f}(\mathbf{r})$ be a vector valued function that describes a multispectral image formed by η-bands. The vector $\mathbf{f}(\mathbf{r}) = \{b1(x,y), b2(x,y), \ldots b\eta(x,y)\}$ represents the value of a pixel through the bands, i.e., the image value at a pixel location $\mathbf{r} = (x,y)$. The function $\mathbf{f}(\mathbf{r})$ is a vector field that describes the multispectral image.

The Fourier transform of $\mathbf{f}(\mathbf{r})$ is defined as (Bracewell, 2003; Ebling and Scheuermann, 2005; Lira, 2010)

$$\mathbf{F}(\boldsymbol{\omega}) = \mathrm{F}[\mathbf{f}(\mathbf{r})] = \int_{-\infty}^{+\infty} \ldots \int_{-\infty}^{+\infty} \mathbf{f}(\mathbf{r}) \exp\{-2\pi j \mathbf{r}\cdot\boldsymbol{\omega}\} d\mathbf{r} \tag{1}$$

The Fourier transform of the vector field $\mathbf{f}(\mathbf{r})$ produces a vector valued function in Fourier space, namely, $\mathbf{F}(\boldsymbol{\omega}) = \mathscr{F}[\mathbf{f}(\mathbf{r})]$. The vector $\mathbf{F}(\boldsymbol{\omega}) = \{F1(\omega 1, \omega 2), \ldots F2(\omega 1, \omega 2), F\eta(\omega 1, \omega 2)\}$, represents the spatial frequency content of the image at the location $\omega = (\omega 1, \omega 2)$. In $\mathbb{R}^{\eta}$,the coordinates in the Fourier domain $(\omega 1, \omega 2)$, and spatial domain (x,y), cover the same range, $1 \le (x, \omega 1) \le M$ and $1 \le (y, \omega 2) \le \_N$, but their meaning is different: (x,y) represents spatial coordinates, while $(\omega 1, \omega 2)$ represents spatial frequencies.

In discrete space $\mathbb{Z}^{\eta}$, the coordinates in the Fourier domain $\mathbf{k} = (k_1, k_2)$, and spatial domain $\mathbf{q} = (m,n)$, cover the same range, $1 \le (m, k1) \le M$ and $1 \le (n, k2) \le N$. If $\mathbf{f}(\mathbf{q}) \in \mathbb{Z}^{\eta}$, where $(m,n; k_1, k_2) \in \mathbb{Z}$, then the discrete version of equation (1) is

$$\mathbf{F}(\boldsymbol{k}) = \mathrm{F}[\mathbf{f}(\mathbf{q})] = \sum_{i}^{\eta} \ldots \sum_{m}^{N} \mathbf{f}(\mathbf{q}) \exp\{-2\pi j \mathbf{q}\cdot\mathbf{k}\} \tag{2}$$

where $\mathbf{f}(\mathbf{q}) = \{b_1(x,y), b_2(x,y), \ldots b\eta(x,y)\}$ and $\mathbf{F}(\mathbf{k}) = \{F_1(k_1,k_2), F_2(k_1,k_2), \ldots F\eta(k_1,k_2)\}$. The Laplacian in $\mathbb{Z}^{\eta}$ of the vector field $\mathbf{f}(\mathbf{q})$ is therefore

$$\mathrm{F}[\nabla^2 \mathbf{f}(\mathbf{q})] = -(2\pi)^2 |\mathbf{k}|^2 \mathbf{F}(\mathbf{k}) \tag{3}$$

where $\mathbf{F}(\mathbf{k}) = \mathrm{F}[\mathbf{f}(\mathbf{q})]$. This equation can be applied to a multispectral image to derive the edge content through the bands. Equation (3) is dubbed the Vector Laplacian. The band

average of the output image given by equation (3) enhances the border and texture information of the original image.

2.4 Principal Component Analysis

Let f (**r**) be a multispectral image composed of η-bands, it is proposed to find a transformation of vector type formed as

$$g(s) = \mathbf{A}[f(r)] \tag{4}$$

In such a way, the operation of **A** on the pixels of the multispectral image f(r) produces a multispectral image, g(**s**) whose bands are decorrelated (Lira, 2010).

The eigenvectors of matrix **A** are dubbed principal components. The bands of g(**s**) associated with each eigenvector are also dubbed principal components. The bands of g(**s**) accumulate, in a decreasing way, the information contained in the original image f(**r**). Only the first principal component was retained.

3 FIELD WORK

The fieldwork was conducted in three regional areas. Two areas are located in the State of Zacatecas, known as Palmillas and Veta Grande. The third area is located in the State of Aguascalientes, known as Paso de Mexicanos (Figures 1a, 1b, 1c). As there are no accurate records of the regions where the old Royal Road vestiges can be found, citations of the approximate location of such places, by means of informants and known historical records, must be used (Gómez Arriola (eds.), 2012).

Once potential sites were located, fieldwork was conducted by surface routes, to search the areas of interest and to collect the necessary information. The geographic coordinates of the ground control points of the visited sites were acquired by means of a Global Position System (GPS) (Table 2). The general state of preservation of the visited sites was noted and photos were taken (Figures 4, 6, 8). The segments of the Royal Road were walked through several tens of meters to inspect and assess the state of the road. The next three sections provide details of the visited sites.

3.1 Veta Grande, Zacatecas

Veta Grande is one of the miner's municipalities where the Albarrada mine is located. From this mine, the extraction of gold, zinc and mainly silver was carried out. It is thought that thanks to this Veta Grande mine, discovered in the year of 1548, that the city of Zacatecas was founded. The Veta Grande town is just 8 km north from the city of Zacatecas. The section of the Royal Road ranging from the Veta Grande mine is practically destroyed, most of the road stone cladding is eroded and only some cobbles, with a maximum width of 5 meters, can be observed (Table 2, Figures 3, 4). The coordinates of the path were taken with a GPS. The road borders a brook that flows into the main town of Veta Grande where the mine is located. By the type of paving and its width, it is thought that it was only used as a branch to connect with the other main road.

3.2 Palmillas, Zacatecas

To reach this village it is necessary to move to the municipality of Ojo Caliente in Zacatecas and from there to the community of Palmillas, and finally travel a route of 3.5 kilometers to the Northwest of this town. This section is the best preserved of the three visited and consists of a continuous strip of rocks aligned and composed, in some sections, by cobblestone-like solid and large stones. The road runs in a straight line towards the town of Palmillas. The coordinates of the path were taken with a GPS and the inspection continued until the point where the pavement disappears (Table 2, Figures 5, 6). The extension that was traversed through corresponds to a section with a length of approximately 700 meters. Some sections were completely paved with a maximum width of 10 meters, other parts with only 5 meters.

3.3 Paso de Mexicanos, Aguascalientes

The Paso de Mexicanos village is located towards the community of Villa Garcia, Aguascalientes. This Royal Road section is located in the direction of the forts of Boca, Ojuelos and Cienega, whose location was strategically settled on the route of the silver. To get to this place, it is necessary to move towards the population known as Villa Garcia and then continue in a southeasterly direction for about 3.2 km. The terrain consists of hills that are occasionally bordered by some runoff, which are filled with water during the rainy season.

The inspection of such a section of the Royal Road indicated a construction of aligned rocks used to prevent erosion of the road, corresponding to the shoulder or sidewalls made of large stones. This is the only feature of the Royal Road that survives up to the present day. In the part where the pavement should be, only a kind of coating is observed on the bottom layer. This seems to be a tamping that acted as a binder where the stone was placed in the upper layer. The road was leveled, since the track is quite even, and follows the natural slope with gentle inclinations. The covered walkway extension was 600 meters, the width of which is about 5 meters (Figures 7, 8). The coordinates of the path were taken with a GPS (Table 2). At the site where a portion of the Royal Road experienced a ground a drop, along with a modern dirt road, the line of the old road disappears. It should be noted that in this region, the ground completely lacks any type of vegetation, which promotes erosion and as a result, has had a strong impact on the destruction of the road.

RESULTS

A pattern recognition problem is the basic nature of this research. The observation and identification of the remnants of the Royal Road is the first step to resolve such a problem. The second step is the quantification of the morphologic characteristics of the remnants, such as geographic location, length, orientation, actual path, and state of degradation. The procedure for the recognition of the remnants of the Royal Road can be conducted for the available satellite images and the known tracks from fieldwork. Nonetheless, high-resolution satellite images are required since the Royal Road segments are relatively narrow, with some degree of degradation, and partially covered by vegetation.

There are numerous roads in the three study areas. Some of such roads have similar spectral and spatial characteristics as the segments of the Royal Road. A visual inspection of the high-resolution images does not lead to unambiguous identification of the Royal Road. Therefore, a digital procedure is required combined with fieldwork. The Vector Laplacian has been used successfully to enhance the texture and the first principal component possess a property to enhance the edges and the reflectivity of the roads.

The Vector Laplacian operator was applied to the four bands of the images. The bands of the resulting vector field were averaged (Section 3.2.2). The resulting image provides an enhancement of the texture of the Royal Road segments.

Principal component analysis was applied to the bands of the images (section 3.2.3). Only the first component was retained. This first component shows an enhancement of the contrast between the Royal Road segments and its environs.

An RGB false colour composite was prepared using the image produced by the Vector Laplacian, the first principal component, and band 4. The RGB was formed as RGB = [Laplacian, PC1, B4). The RGB composites are shown in figures 3, 5 and 7. A red arrow points to the location where the geographic coordinates and assessment of the Royal Road segments were acquired in the fieldwork task. A detailed description of the three study sites is provided in the next sections.

1 Veta Grande, Zacatecas

This segment is closed to the small town Veta Grande in the State of Zacatecas; its access is relatively easy. The length of this segment is close to 1,000 meters. This segment belongs to a secondary road to connect an ancient mine. Even though with a major degradation, this segment shows the best visibility due to the contrast and difference in texture with respect to the entourage.

2 Palmillas, Zacatecas

This segment is away from a town or a highway, its access is difficult only by bare foot. The segment shows medium degradation, but it is barely visible due to small brushes growing in the middle and along the stones that form the road. The length of this segment is close to 1,200 meters. The westward part of this segment shows poor visibility, while the eastward is clearly distinguishable in the image.

3 Paso de Mexicanos, Aguascalientes

This segment is not near any town or a highway, therefore its access is only by bare foot. The segment is barely visible due to a major degradation and the vegetation intermingled with the stones that form the road. The length of this segment is close to 2,000 meters. The westward part of this segment is barely visible in the image, while the eastward is easy to appreciate in the image. This segment is formed by to straight roads that change direction in the crossing a mayor geologic feature in the terrain.

Conclusions

The Royal Road of the Interior Land is a valuable archaeological heritage for humankind and in particular, for Mexico and the United States. The recognition of the actual segments of the Royal Road is an important step for its preservation. The use of high-resolution satellite images, and pattern recognition techniques, set the basis for a precise identification of the actual state of the Royal Road. The mapping of the remains of the Royal Road, from Mexico City to Santa Fe, NM, is a major task that requires extensive fieldwork and substantial funding. The enhancement techniques, to produce evidence of the segments of the Royal Road, are well known procedures and need no further analysis.

A possible recommendation for future work on identification and assessment of the Royal Road would be to use multispectral images of a 30 cm pixel with four bands. However, such images are more expensive that the images used in this research with a pixel of 50 cm and four bands. An important aspect to be considered is the availability of cloud-free images of the zones where segments of the Royal Road are known to exist.

The Royal Road of the Interior Land ranged 3,000 kilometers from Mexico City and Santa Fe, NM, USA. Many branches were connected to the main track. The Royal Road was an important element of economic, social and political development during the colonial times of Mexico. The recognition of the surviving segments is required to preserve the cultural heritage of Mexico. The present research is a first step in such a major effort.

ACKNOWLEDGMENT

The authors thank the satellite receiving station ERMEX NG for the free delivery of the SPOT 6 image.

REFERENCES

Bracewell, R.N., 2003, *Fourier Analysis and Imaging*, Kluwer Academic.

Comer, D.C., Harrower, M.J., 2013, *Mapping Archaeological Landscapes from Space*, Springer, New York.

Diario Oficial 1972, *Ley Federal Sobre Monumentos y Zonas Arqueológicas, Artísticos e Históricos*, Cámara de Diputados, Diario Oficial de la Federación, 6 de Mayo de 1972.

Earth Observing System, 2019. eos.com.

Ebling J.,Scheuermann G., 2005, Clifford Fourier Transform on Vector Fields, *IEEE Transactions on Visualization and Computer Graphics*, Vol. 11, pp. 469 – 479.

Gómez Arriola, L.I., (eds.) 2012, *Management Plan of the Camino Real de Tierra Adentro*, México, Instituto Nacional de Antropología e Historia.

Hanson, W.S., Oltean, L.A., (Eds) 2013, *Archaeology from Historical Aerial and Satellite Archives*, Springer, New York.

Jackson, H., 2006, *Following the Royal Road: A Guide to the Historical Camino Real de Tierra Adentro*, University of New Mexico Press.

Lira J., 2010, *Tratamiento Digital de Imágenes Multiespectrales*, www.lulu.com, ISBN 978-1-105-04502-8.

Lira J., 2011. La Percepción Remota, www.lulu.com, ISBN 978-1-105-05199-9.

Lira J., Rodríguez A., 2014, Edge enhancement in multispectral satellite images by means of vector operators, *Geofísica Internacional*. Vol. 53, pp. 289 - 308.

Moorhead, M.L., 1995, *New Mexico's Royal Road: Trade and Travel on the Chihuahua Trail*, University of Oklahoma Press.

Parcak, S.H., 2009, *Satellite Remote Sensing in Archaeology*, Routledge, Taylor and Francis, New York.

Preston, D., Esquibel, J.A., Preston, C., 1998, *The Royal Road: El Camino Real from Mexico City to Santa Fe*, University of New Mexico Press.

Staski E., 1998, Change and inertia on the frontier: archaeology at the paraje de San Diego, Camino Real, in Southern New Mexico, *International Journal of Historical Archaeology*, Vol. 2, pp. 21 - 44.

Tapete D., Cigna F., 2016, Trends and perspectives of space-borne SAR remote sensing in archaeological landscape and cultural heritage applications, *Journal of Archaeological Science: Reports*, in press, doi.org/10.1016/j.jasrep.2016.07.017.

Wiseman, J., El-Baz, F., (eds) 2007, *Remote Sensing in Archaeology*, Springer, New York.

TABLES

Table 1.- Basic technical details of Pleiades Images of study sites

Sensor	Date	Spectral Bands (nm)	Dimension (Pixels)	Pixel (m^2)
Pleiades 1B	November 17, 2017	Pan: 480 - 830	10,849 × 10,549	0.5 × 0.5
		Blue: 430 - 550		1.5 × 1.5
		Green: 490 - 610		1.5 × 1.5
		Red: 600 - 720		1.5 × 1.5
		NIR: 750 - 950		1.5 × 1.5
Pleiades 1A	September 13, 2017	Pan: 480 - 830	9,154 × 9,607	0.5 × 0.5
		Blue: 430 - 550		1.5 × 1.5
		Green: 490 - 610		1.5 × 1.5
		Red: 600 - 720		1.5 × 1.5
		NIR: 750 - 950		1.5 × 1.5
Pleiades 1A	November 23, 2017	Pan: 480 - 830	1,768 × 1,672	0.5 × 0.5
		Blue: 430 - 550		1.5 × 1.5
		Green: 490 - 610		1.5 × 1.5
		Red: 600 - 720		1.5 × 1.5
		NIR: 750 - 950		1.5 × 1.5

Level 1A - Correction of radiometric anomalies. Cartographic projection UTM, WGS84.

Table 2. Location of sites of known segments of the Royal Road.

Location	Coordinates	Description	Figures
Veta Grande	22° 51' 58.158", -102° 32' 42.375"	Major degradation	4
Palmillas	22° 39' 43.022", - 102° 22' 48.874"	Medium degradation	6
Paso de Mexicanos	22° 11' 3.308", - 101° 58' 30.838"	Major degradation	8

FIGURES

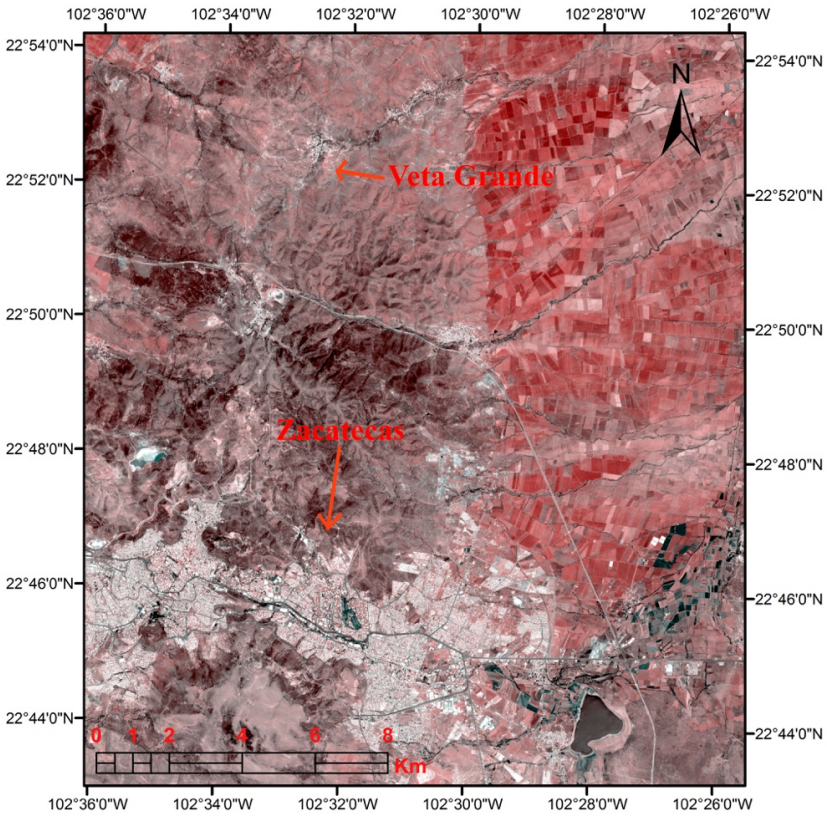

Figure 1a. Location map of Veta Grande segment.

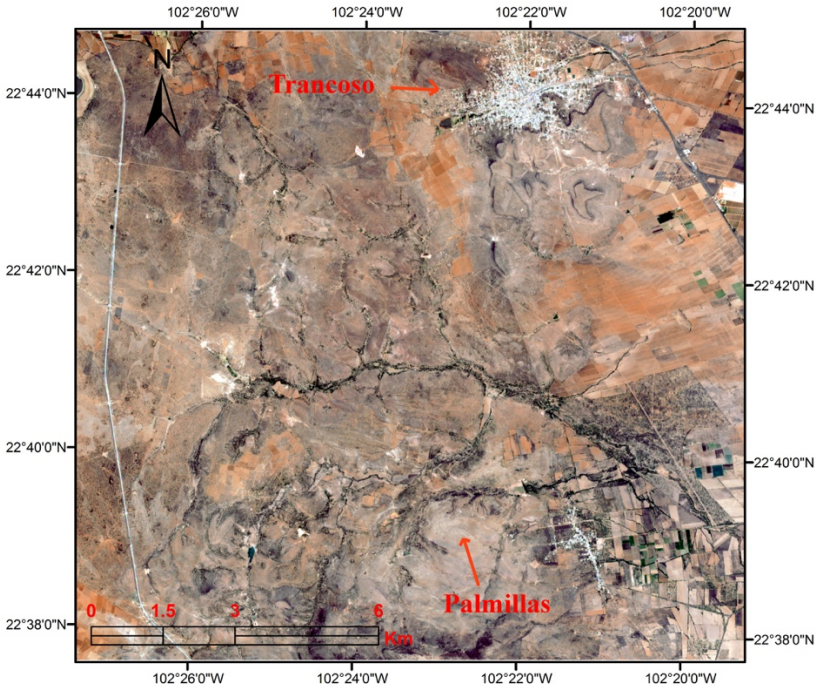

Figure 1b. Location map of Palmillas segment.

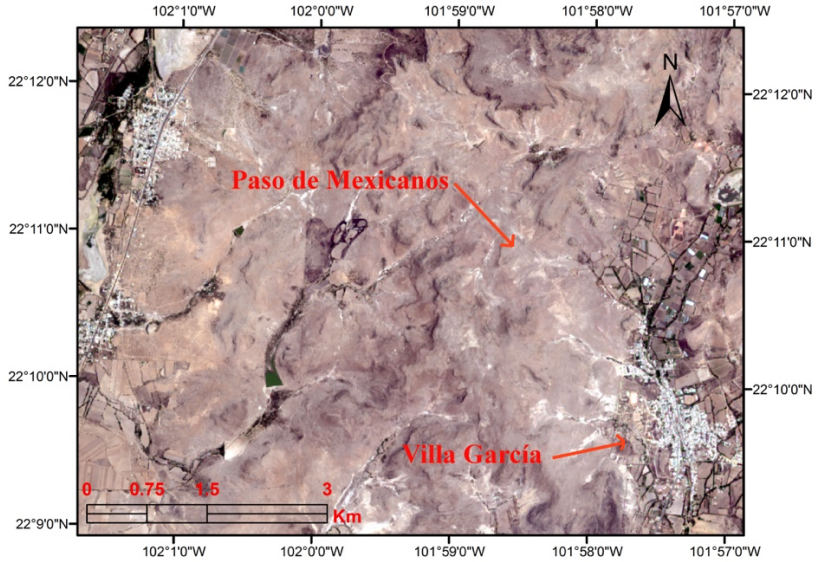

Figure 1c. Location map of Paso de Mexicanos segment.

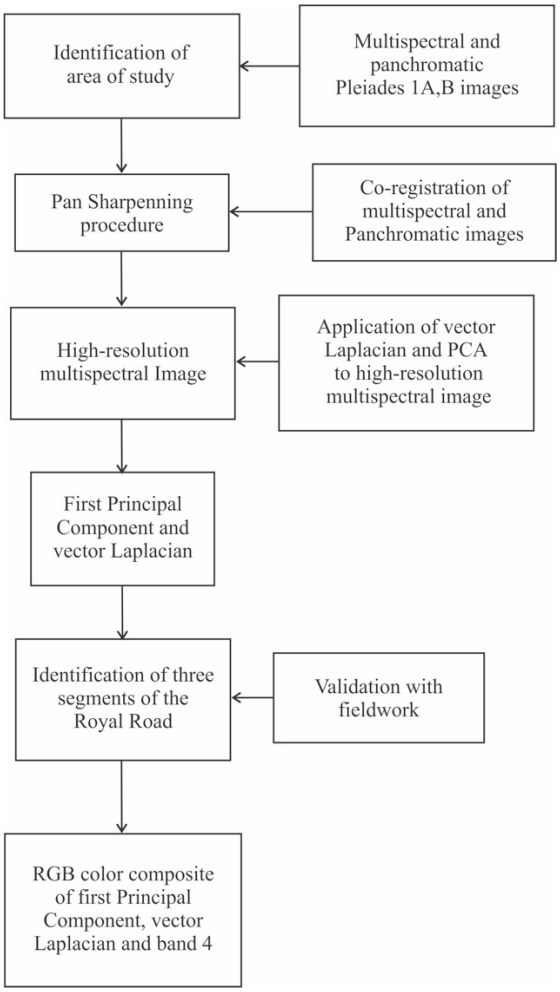

Figure 2. Block diagram of the enhancement and sharpening process.

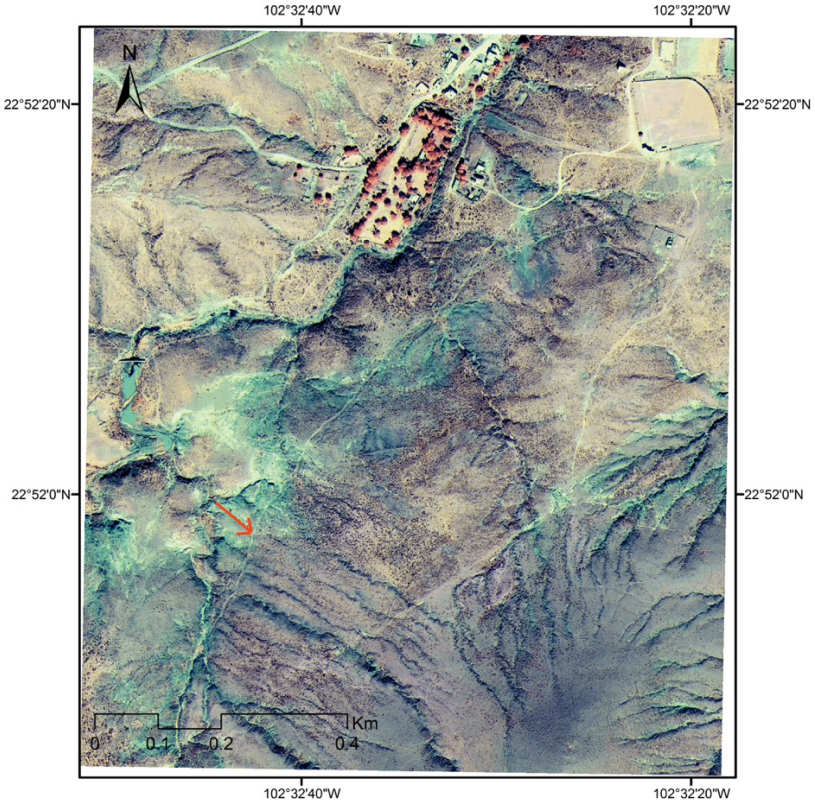

Figure 3. The segment of the Royal Road dubbed Veta Grande, runs from Southwest to Northeast. The RGB = [Laplacian, PC1, B4). The red arrow points to the location of field work and the geographic coordinates shown in table 1

Figure 4. Mosaic of the identification of the segment of the Royal Road in Veta Grande, Zacatecas. Photos of the aspect of the road.

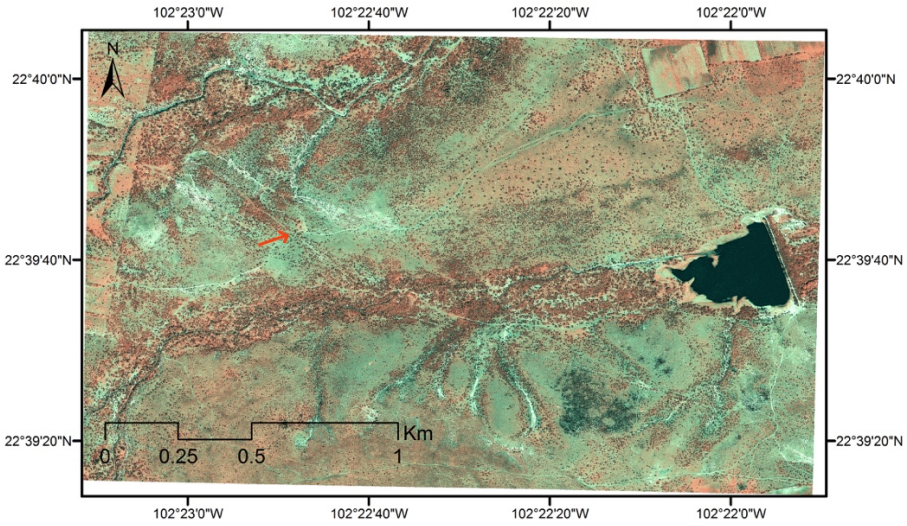

Figure 5. The segment of the Royal Road dubbed Palmillas, runs from Southeast to Northwest. The RGB = [Laplacian, PC1, B4). The red arrow points to the location of field work and the geographic coordinates shown in table 1.

Figure 6. Mosaic of the identification of a segment of the Royal Road in Palmillas, Zacatecas. Photos of the aspect of the road.

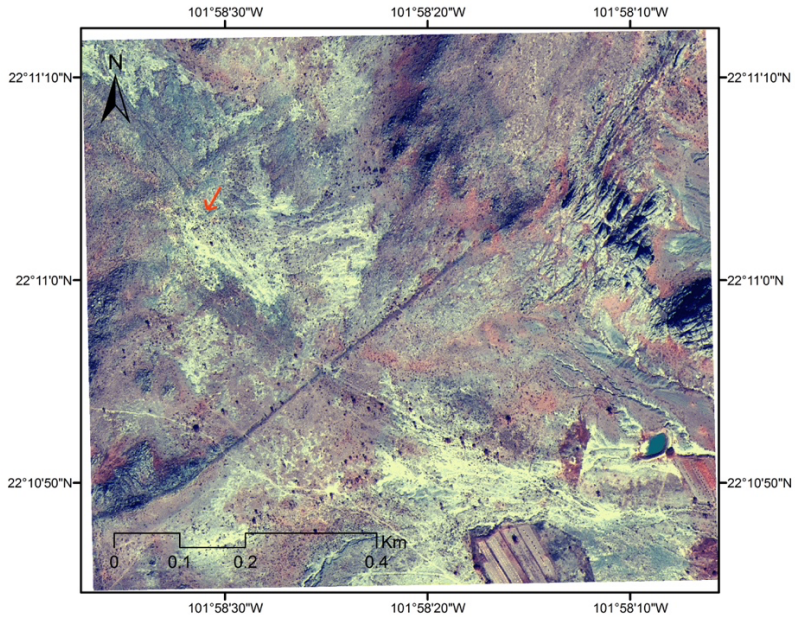

Figure 7. The segment of the Royal Road dubbed Paso de Mexicanos, runs from North West to North East. The RGB = [Laplacian, PC1, B4). The red arrow points to the location of field work and the geographic coordinates shown in table 1.

Figure 8. Mosaic of the identification of a segment of the Royal Road in Paso de Mexicanos, Aguascalientes. Photos of the aspect of the road.

Original paper

Gutenberg-Richter B Value Studies Along the Mexican Subduction Zone and Data Constraints

Lenin Ávila-Barrientos *[1] and F. Alejandro Nava Pichardo[2]

Received: February 24, 2020, accepted: July 7, 2020; online publication: October 1, 2020

Resumen

El valor b de la distribución Gutenberg-Richter es una de las herramientas más importantes para estudios de peligro sísmico; dicho valor es de gran utilidad para estimar razones de ocurrencia de sismos, y está relacionado también con niveles de esfuerzo del medio y presenta cambios precursores a la ocurrencia de grandes sismos. Sin embargo, determinaciones correctas y confiables del valor b dependen críticamente de contar con muestras suficientes. Llevamos a cabo estudios orientados a corroborar si efectivamente ocurren cambios precursores del valor b antes de sismos grandes ($M \geq 7.0$) a lo largo de la zona de subducción de México; estos estudios fueron basados en datos del catálogo del Servicio Sismológico Nacional (SSN) de 1988 a 2018. Lo resultados para cinco grandes sismos sugieren que los cambios precursores efectivamente existen, pero las diferencias entre los valores obtenidos no son estadísticamente significativas debido a las incertidumbres causadas porque el SSN usa diferentes escalas de magnitud para sismos pequeños (bajo M ~4.5) y para medianos a grandes (arriba de M ~4.5). Discutimos algunas limitaciones sobre la aplicabilidad de los datos del SSN.

Palabras clave: Peligro sísmico, Relación Gutenberg-Richter, SSN, Valor b, Zona de subducción Mexicana.

Abstract

The Gutenberg-Richter b value is one of the most important tools for seismic hazard studies; this value is most useful in estimating seismicity rates, and also is related to ambient stress levels and shows changes precursory to the occurrence of large earthquakes. However, correct and reliable determinations of the b value are critically dependent on having enough data samples. Studies oriented to corroborate whether precursory changes in the b value occur before large ($M \geq 7.0$) along the Mexican subduction zone, were done based on data from the Servicio Sismológico Nacional (SSN, Mexico's National Seismological Service) seismic catalog, from 1988 to 2018. Results for five earthquakes are suggestive that precursory changes may occur, but differences between measured values are not statistically significant because of large uncertainties due to the SSN using different magnitude scales for small (below M ~4.5) and medium to large (above M ~4.5) magnitudes. We discuss some limitations about the applicability of SSN data.

Keywords: b value, Gutenberg – Richter relation, Mexican subduction zone, Seismic hazard, SSN.

*Corresponding author: lenavila@cicese.mx

[1]Conacyt-CICESE, 22860, Ensenada, Baja California, México.

[2] CICESE, 22860, Ensenada, Baja California, México.

INTRODUCTION

The most common statistical tool for seismic hazard analysis is the Gutenberg – Richter (G-R) relation (Gutenberg and Richter, 1942, Ishimoto and Ida, 1939, Richter, 1958), that describes the distribution of earthquake magnitudes as

$$\log_{10} N(M) = a_1 - b(M - M_1) \ , \tag{1}$$

where N is the number of earthquakes with magnitude greater than or equal to M. Parameter a_1 is the logarithm of the total number of earthquakes with $M \geq M_1$, and parameter b, the slope of the relation commonly referred to as the b-value, is a measure of the relative quantities of small to large earthquakes and is usually ~1. M_1 (often denoted M_c) is the minimum magnitude for which coverage is complete, so that for smaller magnitudes $\log_{10} N$ and M are not linearly related.

While a_1 depends on the sample time and overall seismicity rate, b is related to the local geology and to the level of ambient stress (Scholz, 1968; Ghosh *et al.*, 2008) and is related to the fractality of fractures (Aki, 1981; Öncel *et al.*, 2001), so that it varies in time and space (Enescu and Ito, 2002). Several authors have found precursory changes in the b-value before the occurrence of major earthquakes (e.g. Shaw *et al.*, 1992; Wyss and Wiemer, 2000; Enescu and Ito, 2001; Márquez-Ramírez, 2012). Hence, b is an extremely important parameter in seismic hazard studies, both for estimating seismicity occurrence rates and as a precursor to large earthquakes.

There is no explicit upper limit to the magnitudes used in (1) and, since there must be a physical limit to how large an earthquake can be, many authors have proposed ways of truncating or modifying the G-R relation to account for a maximum possible magnitude M_{max} (Utsu, 1999). However, for most studies, the G-R relation ceases to be linear for magnitudes way below a maximum possible magnitude; obviously, magnitudes below that corresponding to $\log_{10}(M) < 0$ are either under- or over-sampled, but under- or over-sampling are common for magnitudes corresponding to $\log_{10}(M) < 0.5$ or 0.6. Let us denote by M_2 the magnitude above which over- or under-sampling occur, according to the completeness of the seismic catalog; then the G-R histogram will behave linearly only within the $[M_1, M_2]$ range.

Often the b-value is determined by fitting a straight line to the linear part of the G-R histogram that, since magnitudes are usually rounded to one decimal place, commonly has classes $\Delta M = 0.1$ wide.

Another common way to estimate the b-value is through the Aki-Utsu relation, which is based on the fact that the G-R relation (1) is a reverse cumulative distribution according to which magnitudes are distributed exponentially as

$$f(M) = \beta \, \mathrm{e}^{-\beta(M - M_1)}; \quad M \geq M_1, \tag{2}$$

where $\beta = b \ln(10)$. (c.f. Lomnitz, 1974), and β is related to the mean of the distribution, μ, as $\beta = 1/(\mu - M_1)$ (c.f. Parzen, 1960), so that

$$b = \frac{\log_{10} \mathrm{e}}{\mu - M_1} . \tag{3}$$

Aki (1965) showed that the maximum-likelihood estimate of *b*, b_m, is given by

$$b_m = \frac{\log_{10} \mathrm{e}}{\bar{M} - M_1}, \tag{4}$$

where $\bar{M}$ is the sample mean, and Utsu (1965) pointed out that, since magnitudes are rounded to ΔM, the actual minimum magnitude is $M_1^U = M_1 - \Delta M / 2$, so that

$$b_m = \frac{\log_{10} \mathrm{e}}{\bar{M} - M_1^U}. \tag{5}$$

Formula (5), which we will refer to as the Aki-Utsu estimate, has been widely used as a simple and straightforward way of estimating *b* directly from the magnitude sample mean, with no explicit need for a G-R histogram. However, in too many cases, people do not realize the need for correctly determining M_1^U, and of having a representative sample from the linear part of the histogram that is large enough so that $\bar{M} \cong \mu$, which is an absolute requirement for $b_m \cong b$. In too many cases $\bar{M}$ is estimated from too small samples, either because data are scarce or because no attention is paid to the matter of representativity, and small samples result in estimates with too much scatter to be useful (Kramer, 2014; Nava *et al.*, 2017a).

Whichever the method used to estimate the *b*-value, the data has to fulfill two requirements: first, the number of data in the $[M_1, M_2]$ range and the range itself need to be large enough so that a straight line can be adequately fitted or so that the observed mean magnitude is representative of the distribution mean; second, the data should be homogeneous.

The first requirement is not particularly difficult to meet when considering a large area or a long-time history, but when trying to have a good definition in time and/or space, which requires short time and/or space windows, then having a representative sample may be difficult.

The second requirement can have three aspects. Homogeneity in time: network coverage usually changes in time, but there are sophisticated techniques to deal, at least partially, with this aspect (e.g. Kijko, 2004; Kijko and Smit, 2014); also, *b* can change in time, in which case the measured value will be an average over time. Homogeneity in space: *b* does change from place to place so that a measure using data from a large region will yield a space average of the local values. Homogeneity in magnitude: it is not uncommon to report moment magnitudes for large earthquakes and use some other scale, such as coda or duration, for small and very small earthquakes; unless the small earthquake scale is correctly calibrated so that it measures like the large magnitude scale, then *b*-value determinations will be erroneous.

We next describe the problems encountered with this third requirement, while trying to determine whether changes in the *b*-value were observable before and after large earthquakes in the Mexican subduction zone.

THE MEXICAN SUBDUCTION ZONE

The tectonic activity in the south and southeast of México is governed by the subduction of the Rivera and Cocos plates under the North American plate (Figure 1). It is along this subduction zone where the largest earthquakes in Mexico have occurred. The subduction dip angle of the

Cocos plates changes from sub-horizontal below central México to major dip [25^0-30^0] near Chiapas to the southeast (Pérez-Campos *et al.*, 2008). The convergence velocity also changes, the Cocos plate has a velocity of 4 to 5 cm/yr in its western part, and the eastern part has velocity around 6 to 7 cm/yr relative to the North American plate (Dañobeitia *et al.*, 2016; Nuñez-Cornú *et al.*, 2016; Gutiérrez *et al.*, 2015; Kostoglodov and Bandy, 1995; Kostoglodov and Pacheco, 1999).

International catalogs do not list magnitudes small enough for reliable *b*-value determinations in this region, so that we decided to use data from the *Servicio Sismológico Nacional* (*SSN*, Mexico's National Seismological Service) seismic catalog, from 1988 (Zúñiga *et al.*, 2000) to 2019.

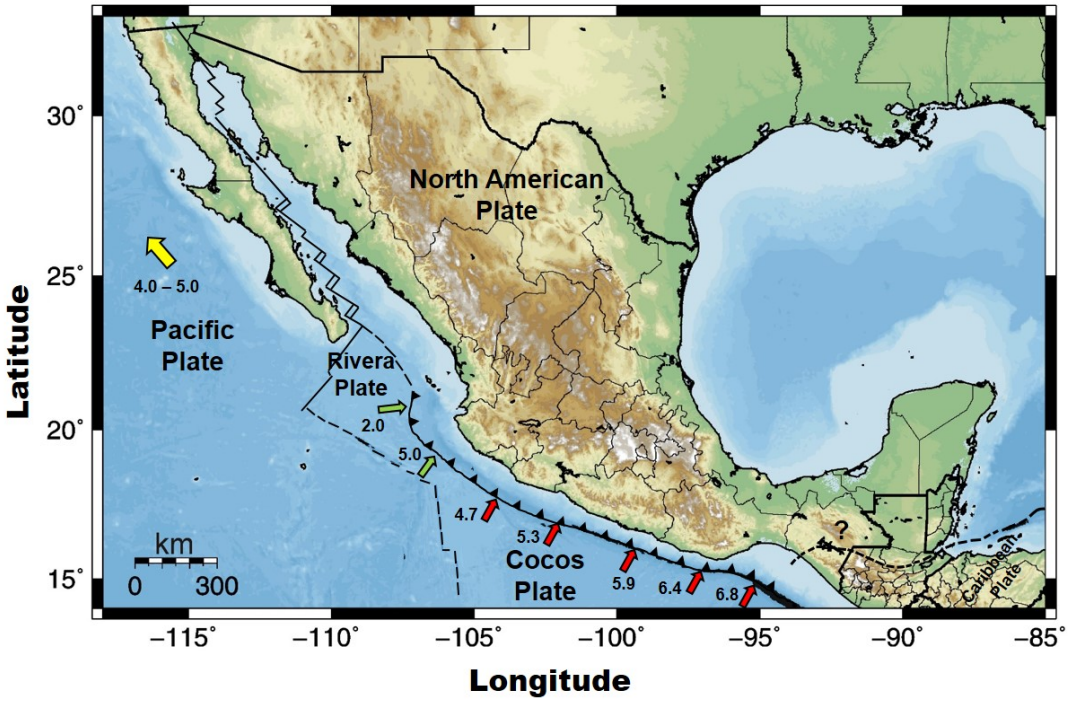

Figure 1. Tectonic plates interaction in México. Numbers indicate the velocity in cm/yr, and arrows show the local direction of the subducting plates relative to the North American plate. Red for the Cocos plate, Green for the Rivera plate, and Yellow for the Pacific plate.

Event Selection

We considered all earthquakes with $M \geq 7.0$ along the subduction zone, and selected a region around each mainshock, according to the spatial distribution of its aftershocks, to sample regions subject to the stresses that would cause the mainshock. Some of the regions were adjusted to avoid including events associated with another mainshock. Only mainshocks with enough data for pre- and post-event time windows were considered for *b* determination; Figure 2 shows the chosen areas, and Table 1 lists their magnitude, occurrence time, location, and the total number of events in window.

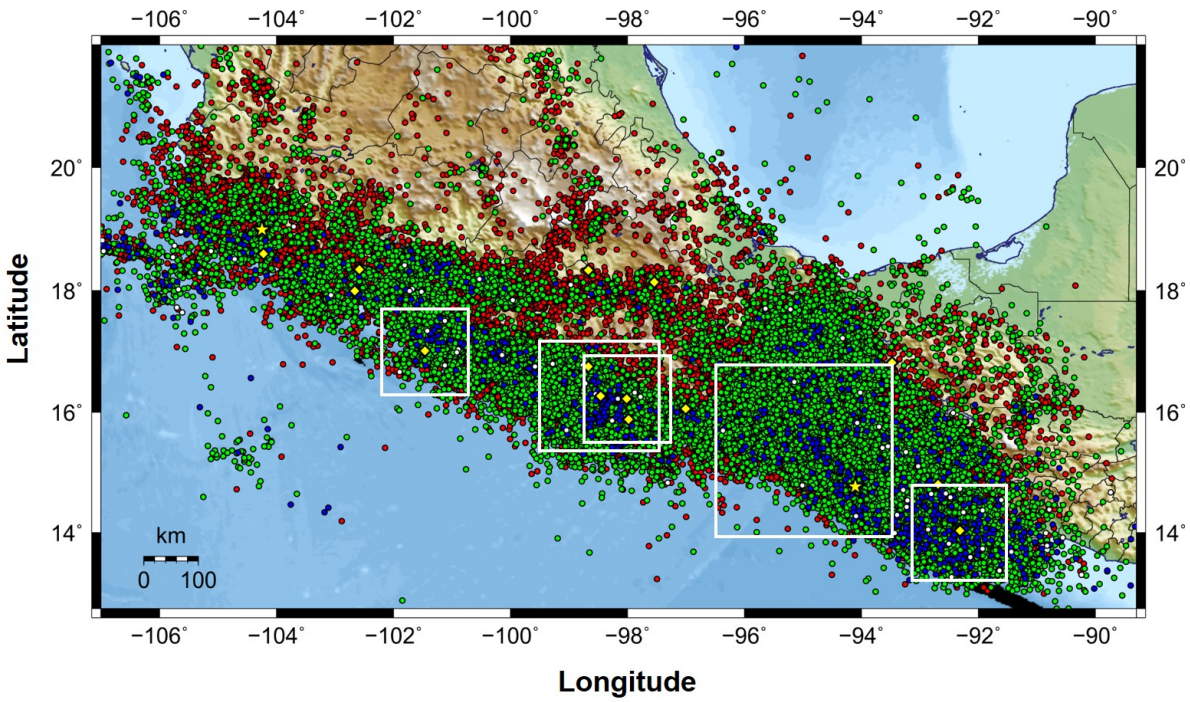

Figure 2. The squares indicate regions used for *b* value determination for large earthquakes along the Mexican subduction zone; from West to East: Guerrero 2014, Oaxaca 2012, Oaxaca 2018, Oaxaca-Chiapas 2017, Chiapas-Guatemala 2012. Dots represent epicenters: red $M < 4.0$, green $4.0 \leq M < 5.0$, blue $5.0 \leq M < 6.0$, grey $6.0 \leq M < 7.0$; Yellow diamond with $7.0 \leq M < 8.0$, and Yellow stars with $M \geq 8.0$.

The cumulative number of earthquakes curve for each region was plotted to determine times and threshold magnitudes for homogeneity; then, the cumulative curves were used to determine time windows. One of the time windows was chosen before the mainshock when stresses are expected to be high, and since the catalog does not extend backwards in time long enough to sample *b*-values before the stress build-up, in order to have a low-stress reference value, a second window was chosen after the mainshock liberated the stored stress and after the significant part of the aftershock activity, when seismicity was back to background level, so that we could sample low-stress *b*-values without aftershock noise.

As an example, Figure 3 shows the selection of pre and post-events for the 2012.85, *M* 7.3 earthquake located at the Mexico (State of Chiapas) — Guatemala border. From the cumulative curve for the whole region (Figure 3-Top), a clear change in the slope, possibly due to changes in the seismic network, is apparent around 2011, so that we used events from this point on to the end of the catalog. The pre- and post-mainshock time windows, which will be referred to as W1 and W2 from now on, are shown in Figure 3 (Bottom).

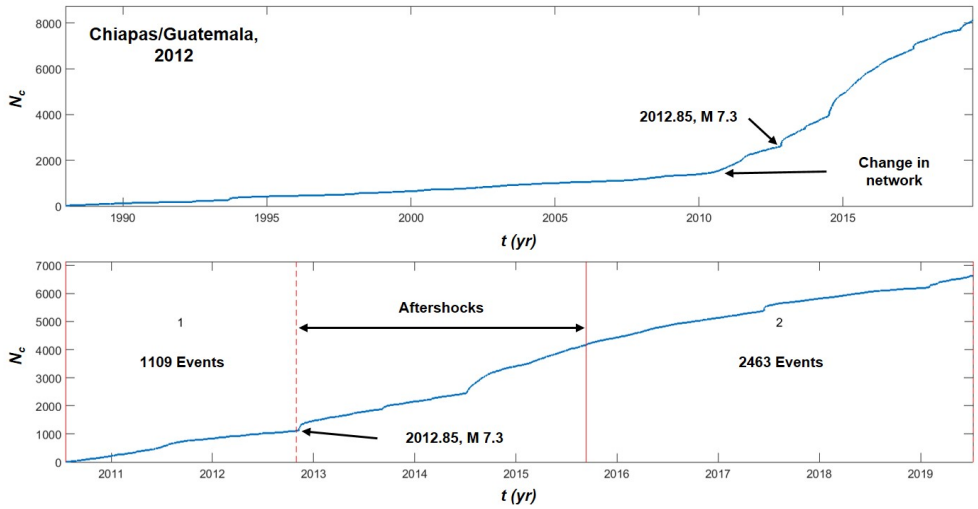

Figure 3. Cumulative curve for the 2012.85 earthquake located in the border of Chiapas/Guatemala. Top: Complete catalog. Bottom: Time windows, pre-earthquake W1 with 1109 events, and post-earthquake W2 with 2463.

B VALUE DETERMINATION METHOD AND DATA

We used the *most likely source b* method proposed by Nava *et al.* (2018). The M_1 and M_2 limits for the linear range of the G-R relation are chosen from the $\Delta M = 0.1$ G-R histogram, with the aid of the non-cumulative version of the histogram, and the Aki-Utsu method is used to estimate a *measured* b_m. Next, considering that the observed magnitudes constitute but one realization of random process having a source (or "true") value *b*, Monte Carlo methods are used to estimate the likelihood $\Pr(b_m \mid M_1, M_2, N, b)$, where N is the number of events in the $[M_1, M_2]$ range, for all different possible "true" *b*-values in a range around b_m which result in non-zero probabilities. For each possible source *b* value, N_r realizations of N events with magnitudes in the $[M_1, M_2]$ range are generated, from each realization a "measured" *b*-value is determined, and the number of times that this value equals b_m (number of "hits") is counted; a histogram of the number of hits for all source *b* values is made and normalized to result in a likelihood distribution. The *b*-value having the highest likelihood, b_x, is chosen as the most likely source *b*-value to have resulted in the observed realization. $N_r = 25{,}000$ Monte Carlo realizations were used here for each source *b* determination.

A further advantage of this method is that it gives the probability distribution for source *b*-values, so that it is possible to estimate bands for given confidence limits and estimate probabilities for two measures being distinct and the difference between them being significant.

RESULTS

Figure 3 shows the time window for the Chiapas-Guatemala 2012 earthquake; Figure 4 shows the windows selected for the rest of the earthquakes listed in Table 1. Because the aftershock sequence of the M_W 8.2 Oaxaca-Chiapas earthquake is not finished yet, it was not possible to have a post-quake window for this event.

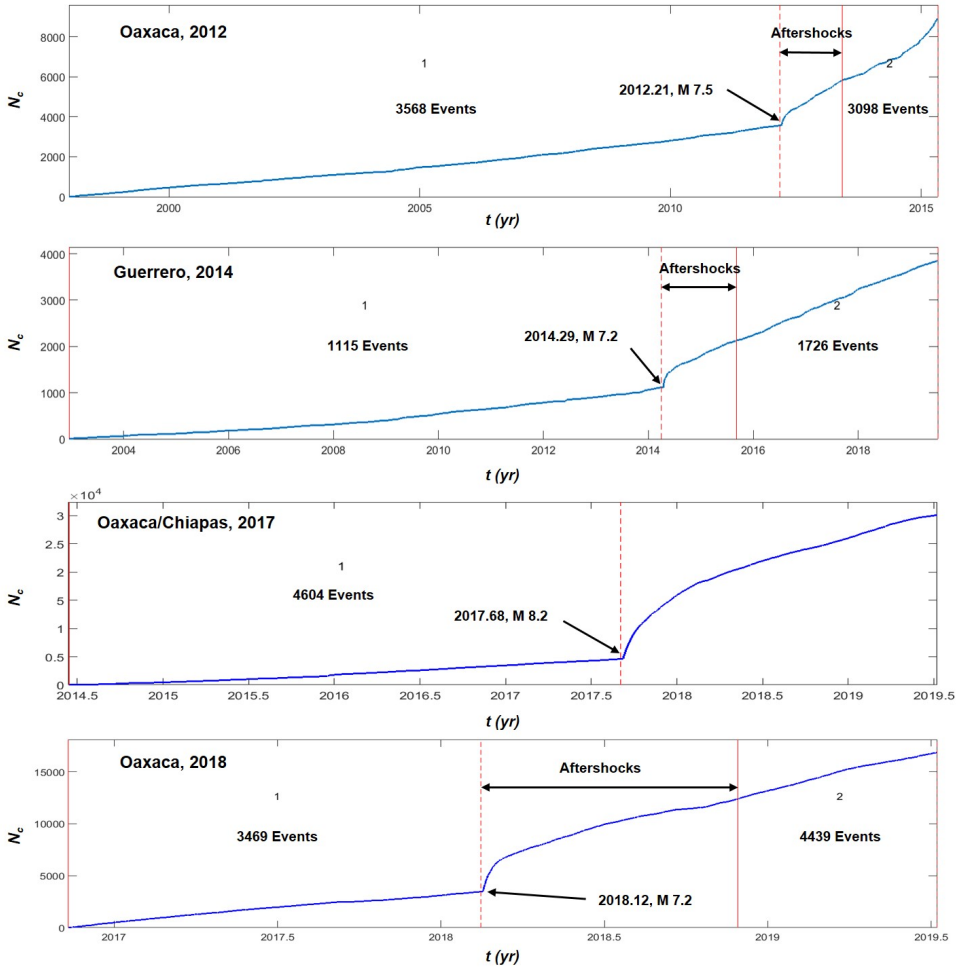

Figure 4. Pre and post-mainshock time windows for the earthquakes listed in Table 1.

Table 1.- Earthquakes with enough data for *b* determination.

M	Time	Lon	Lat	Depth	State Year	Total
7.50	2012.2179	-98.4570	16.2640	18.00	Oaxaca 2012	8927
7.30	2012.8516	-92.3160	14.0270	17.10	Chiapas/Guatemala 2012	6637
7.20	2014.2948	-101.4600	17.0110	18.00	Guerrero 2014	3857
8.20	2017.6855	-94.1030	14.7610	45.90	Oaxaca/Chiapas 2017	30143
7.20	2018.1287	-98.0140	16.2180	16.00	Oaxaca 2018	16833

Figures 5 to 9 show the fit of b_m to the G-R distribution (left), and the likelihood distribution and b_x choice (right) for events listed in Table 1; the b_m and b_x values are listed in Table 2.

Table 2. b-value before and after the large earthquakes.

Region	Time	*M*	Pre-event	Post-event

Event			b_m	b_x	M_1	M_2	N	b_m	b_x	M_1	M_2	N
Guerrero	2014.294	7.2	1.860	1.74	3.8	4.7	586	1.963	1.82	3.7	4.5	872
Oaxaca	2012.217	7.5	1.927	1.78	4.0	4.8	1200	2.550	2.41	3.7	4.3	1117
	2018.128	7.2	2.237	2.18	3.5	4.3	1485	2.437	2.26	3.6	4.2	1039
Oaxaca/ Chiapas	2017.685	8.2	2.388	2.18	3.9	4.5	914					
Chiapas/ Guatemala	2012.851	7.3	2.299	2.18	3.8	4.5	524	2.432	2.24	4.0	4.6	619

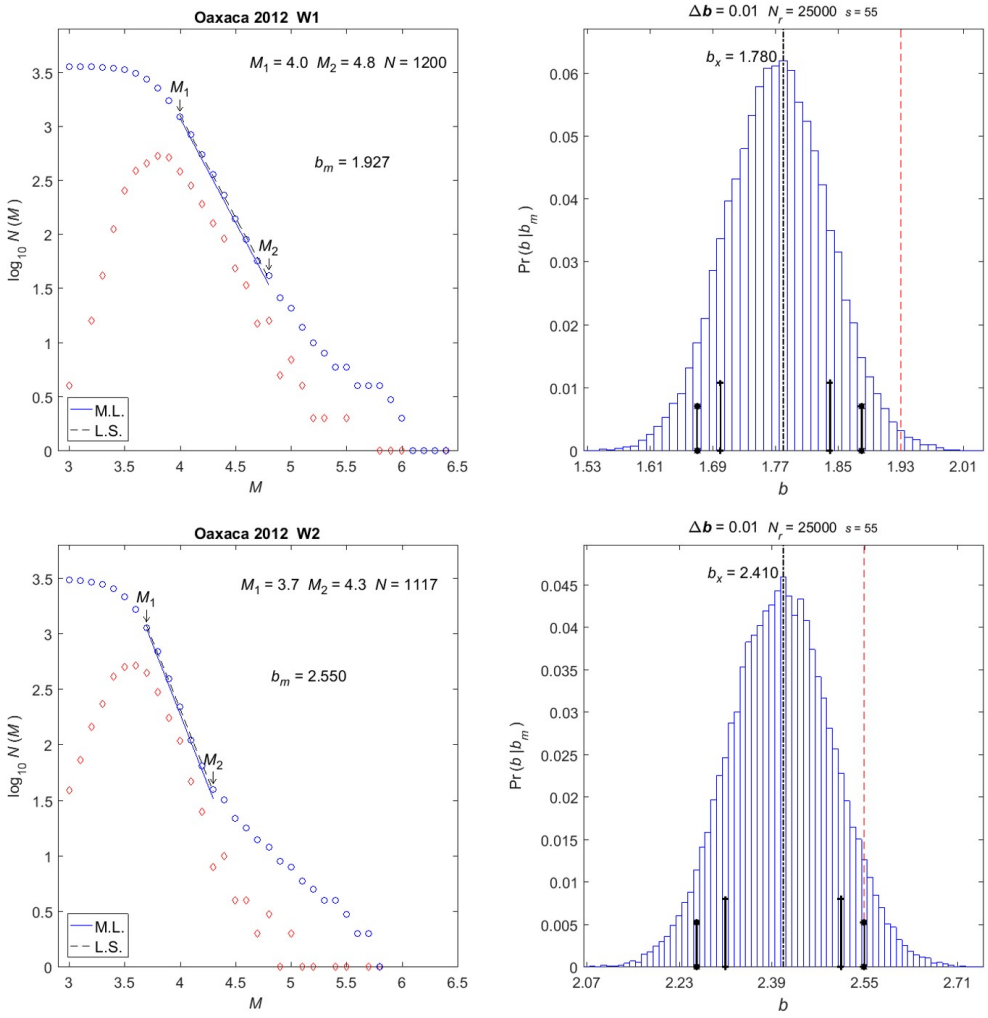

Figure 5. Oaxaca 2012. Left: G-R fit for b_m; (blue) circles are the G-R histogram, and (red) diamonds show the corresponding non-cumulative distribution; N is the number of data in the linear range from M_1 to M_2; M.L. is the straight line corresponding to b_m the maximum likelihood fit; L.S. is the dashed line for the least-squares fit (shown for comparison only). Right: b likelihood distribution; Δb is the class width, N_r is the number of Monte Carlo realizations, s is the pseudo-random number generator seed; the thin dashed red line indicates b_m, the black dash-dot line indicates b_x. Short vertical lines with crosses and asterisks indicate 75% and 90% confidence ranges, respectively. Top: Pre-event W1. Bottom: Post-event W2.

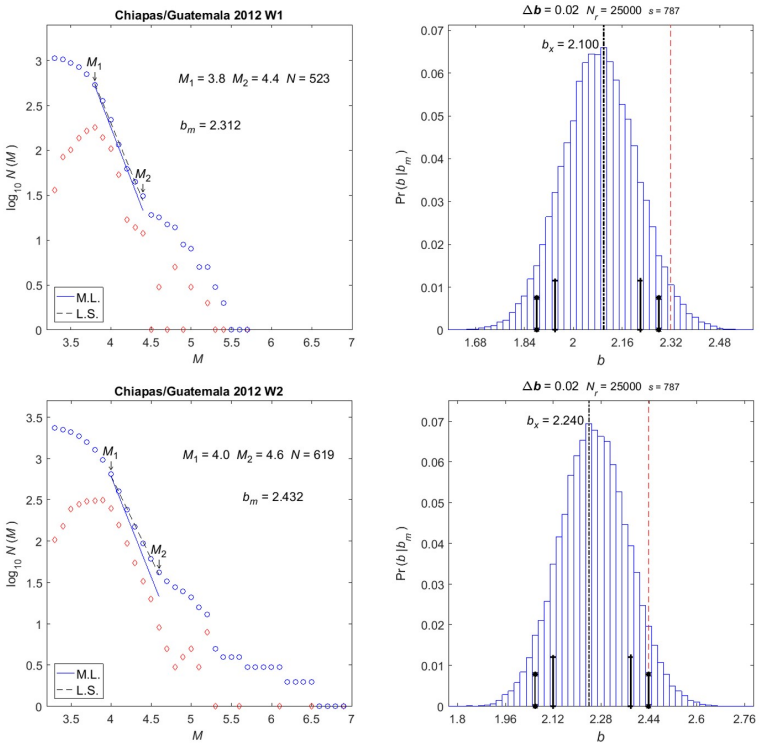

Figure 6. Chiapas-Guatemala 2012. Same conventions as in Figure 5.

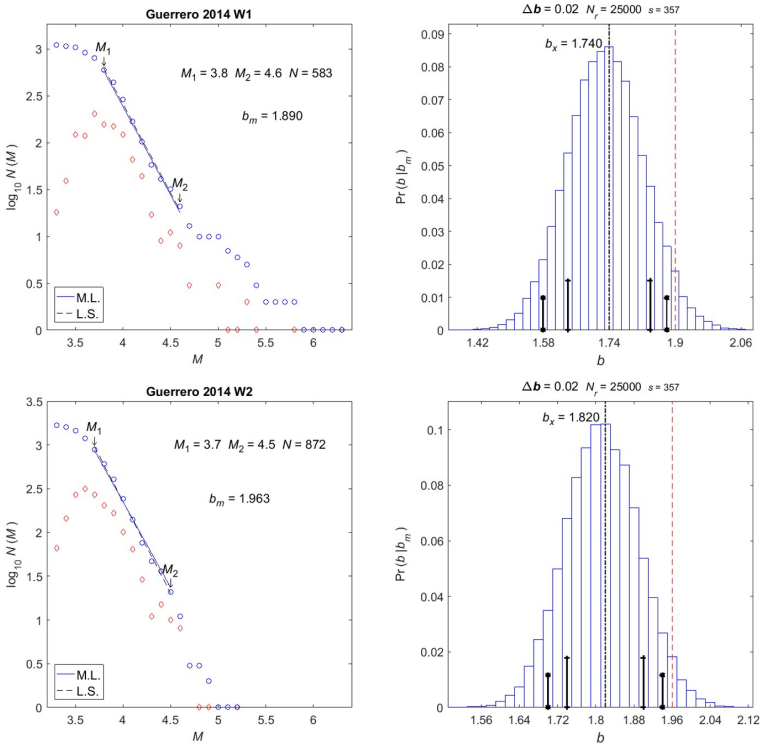

Figure 7. Guerrero 2014. Same conventions as in Figure 5.

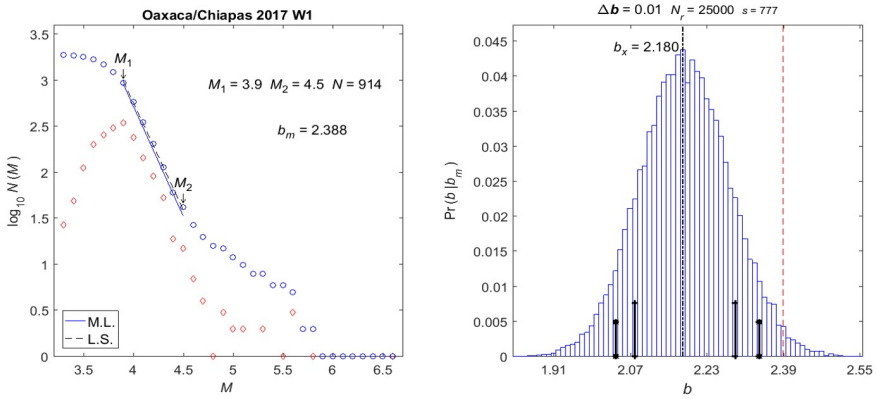

Figure 8. Oaxaca-Chiapas 2017. Same conventions as in Figure 5.

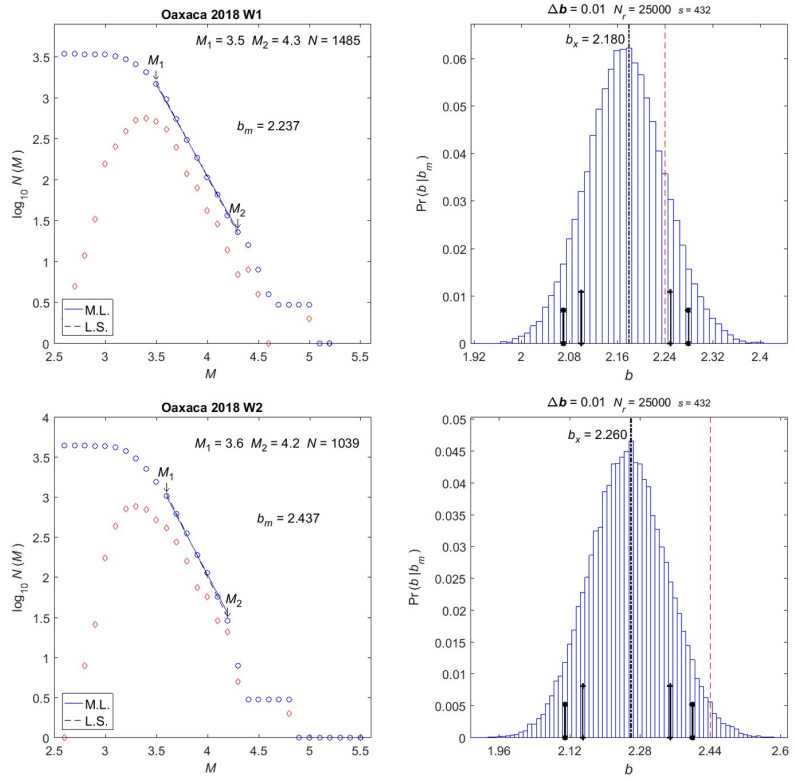

Figure 9. Oaxaca 2018. Same conventions as in Figure 5.

From these figures, it is clear that the G-R distributions do not have a single slope; all of them show a large slope for small magnitudes and a smaller one for larger magnitudes, meeting around magnitude 4.5. This feature is explained when topic *Mitos y Realidades*, in Sismos y Volcanes CDMX, mobile application software (2019), is consulted; the app. states that the SSN employs M_W for events larger than 4.5 and coda magnitude for events smaller than 4.5 (which scale is used for 4.5 magnitude events remains a mystery).

Because of this change in slope, it was not possible to obtain linear ranges over a wide enough magnitude interval; due to space and time limitations of the windows, only the small magnitude range was (barely) adequate for b_m estimation. As evidenced by the non-cumulative histograms

shown in the G-R plots, there were not enough data in the larger magnitudes range to obtain adequate estimates. Thus, we had to base our estimates on short ranges over only the smaller magnitudes.

A characteristic of the most likely source *b*-value method is that when the linear range is wide, some two or more magnitude units, say, and the number of data within the range is larger than about 2,000; the source *b* distributions are narrow and b_m and b_x are equal or differ by little. For the determinations presented here, with narrow ranges and few data, the source *b* distributions are wide.

We will now proceed to describe our results and defer their interpretation and assessment to the next section. The results are summarized in Table 2.

OAXACA 2012

Figure 5 shows that for this earthquake the linear magnitude range is short for both W1 and W2, so that b_x differs from b_m; for W1, the most likely source *b* value is $b_x = 1.78$, and the source *b* 90+% interval is [1.67, 1.88]; for W2, the most likely source *b* value is $b_x = 2.41$, and the source *b* 90+% confidence interval is [2.26, 2.55]; $\Delta b_x = 0.63$.

The number of data is large enough in both windows so that the source *b* distributions do not overlap; hence, we can say with certainty that the *b*-value before the mainshock is indeed smaller than for a low-stress regime, which reflects the stress accumulation leading to the mainshock and is thus an important observable with precursory value.

It may be argued that had a larger number of realizations or a different seed been used, the tails of the distributions could have been more extended; this is true, but since observed distributions have approximate Gaussian shapes, these extended tails will have extremely low probabilities, so that the probabilities on which significance estimates are based will remain essentially the same.

CHIAPAS-GUATEMALA 2012.

Data before and after this earthquake result in short G-R linear magnitude ranges (Figure 6, left), so that measured b_m values differ from the corresponding b_x ones. For W1, the most likely source b value is $b_x = 2.10$, and the source b 90+% interval is [1.88, 2.28]; for W2, the most likely source b value is $b_x = 2.24$, and the source b 90+% confidence interval is [2.06, 2.44].

From window W1 to window W2, there is an increase $\Delta b_x = 0.14$, but since the number of data in each window is rather small, the source b distributions are wide and overlap.

Let us denote the source b values in W1 by b_{W1}, and let the lower and upper limits of the W1 source b distribution by b_{11} and b_{12}, respectively, and let the corresponding values and limits for W2 be b_{W2}, b_{21} and b_{22} (we will use this notation henceforth). From the distribution histograms, the probability that b_{W1} takes values covered by the W2 distribution is $p_1 = \Pr(b_{W1} \geq b_{21})$, in this case $p_1 = 0.995337$; the probability that b_{W2} takes values covered by the W1 distribution is $p_2 = \Pr(b_{W2} \leq b_{12})$, in this case $p_2 = 0.997478$; the total probability that a source b value may belong to either distribution

is $p_{\cup} = p_1 + p_2 - p_1 p_2$, in this case $p_{\cup} = 0.999988$. Hence, we cannot reject the null hypothesis that b does not change with a certainty above $1 - p_{\cup} = 0.000012$.

GUERRERO 2014.

Results for this earthquake are similar to those for Chiapas-Guatemala 2012, with short linear G-R magnitude ranges and small quantities of data. For W1, the most likely source *b* value is $b_x = 1.74$, and the source *b* 90+% interval is [1.58, 1.88]; for W2, the most likely source *b* value is $b_x = 1.82$, and the source *b* 90+% confidence interval is [1.70, 1.94]; $\Delta b_x = 0.08$.

Overlap probabilities are $p_1 = 0.998962$ and $p_2 = 0.999970$ so that the null hypothesis probability is $p_{\cup} = 0.999999$; which means, that the possibility of b_x having the same value in both windows cannot be discarded.

OAXACA-CHIAPAS 2017.

As mentioned before, aftershocks of this M_W 8.2 do not allow for a W2 window; hence, we analyzed only a W1 window to see whether the measured values agreed with those for other earthquakes. Although the linear range was small, the number of data in it was intermediate. For this earthquake $b_x = 2.18$, and the source *b* 90+% confidence interval is [2.04, 2.34].

OAXACA 2018.

For W1, the most likely source *b* value is $b_x = 2.18$, and the source *b* 90+% interval is [2.07, 2.28]; for W2, the most likely source *b* value is $b_x = 2.26$, and the source *b* 90+% confidence interval is [2.11 2.40]; $\Delta b_x = 0.08$.

Overlap probabilities are $p_1 = 1.000000$ and $p_2 = 0.97164$ so that the null hypothesis probability is $p_{\cup} = 1.000000$.

DISCUSSION AND CONCLUSIONS

The change in slope around *M* 4.5 made it necessary to estimate *b* values using the smaller magnitudes only, and the measured *b*-values are larger than the semi-theoretical 1.5 maximum value (Olsson, 1999). These large values and the change in slope indicate that the M_c scale used by the SSN is not consistent with the M_W scale, so that the above mentioned maximum value does not apply to SSN small magnitudes. There were not enough data to obtain Aki-Utsu *b*-value estimates from the larger magnitudes, but least-squares fits (where possible for large magnitudes) yield values smaller than 1.5.

Hence, the *b*-values obtained here are useful only for comparisons among themselves, and cannot be used for comparisons with values obtained from data sets with true moment magnitudes.

The *b*-values for the Oaxaca 2012 earthquake are definitely smaller for the high stress regime before the mainshock than for the low-stress regime after it. Results for other earthquakes

consistently show *b*-values to be smaller before than after the main events, but the spreads in source *b* distributions make it impossible to discard the corresponding null hypotheses with any significant degree of confidence. We consider, however, that these results do strongly suggest smaller *b* values before the mainshocks than in low-stress regimes.

The question whether *b*-values are a useful precursor tool for the Mexican subduction zone remains an open question and will remain so until the SSN scales for small and large magnitudes agree (hopefully both scaling as M_W), so that reliable *b*-value determinations based on an appropriately wide magnitude range are possible. Meanwhile, let these observations be a caveat for researchers planning to work with *b*-values from the Mexican subduction zone.

ACKNOWLEDGMENTS

Many thanks to the SSN for their data, especially to Víctor Hugo Espíndola, and thanks to Antonio Mendoza for technical support. The Conacyt Cátedras program (2602) and project 222795 funded this research.

REFERENCES

Aki K., 1965, Maximum likelihood estimate of *b* in the formula *log(N) = a - bM* and its confidence limits. *Bulletin of the Earthquake Research Institute*, University of Tokyo 43, 237–239.

Aki K., 1981, A probabilistic synthesis of precursory phenomena, in Earthquake Prediction. An International Review, Maurice Ewing, (eds. D. W. Simpson. and P. G. Richards) American Geophysical Union, Washington, D. C. pp. 566–574.

Dañobeitia J., Bartolomé R., Prada M., Nuñez-Cornú F., Córdoba D., Bandy W. L., Estrada F., Cameselle A. L., Nuñez D., Castellón A., Alonso J. L., Mortera C., Ortiz M., 2016, Crustal Architecture at the Collision Zone Between Rivera and North American Plates at the Jalisco Block: Tsujal Project. *Pure and Applied Geophysics*. 173, 3553–3573. DOI 10.1007/s00024-016-1388-7

Enescu B., Ito K., 2001, Some premonitory phenomena of the 1995 Hyogo-Ken Nanbu (Kobe) earthquake: seismicity, b-value and fractal dimension. *Tectonophysics* 338, 297-314.

Enescu B., Ito K., 2002, Spatial analysis of the frequency-magnitude distribution and decay rate of aftershock activity of the 2000 Western Tottori earthquake. *Earth Planets Space* 54, 847-859.

Ghosh A., Newman A., Amanda M., Thomas A., Farmer G., 2008, Interface locking along the subduction megathrust from b value mapping near Nicoya Peninsula, Costa Rica. *Geophysical Research Letters*, 35, L01301. https://doi.org/10.1029/2007GL031617

Gutenberg B., Ritcher, C., 1942, Earthquake magnitude, intensity, energy and acceleration, *Bulletin of the Seismological Society of America*. Vol. 32, No. 3, pp 163-191.

Gutierrez Q. J., Escudero C. R., Núñez-Cornú F. J., 2015, Geometry of the Rivera-Cocos subduction zone inferred from local seismicity. *Bulletin of the Seismological Society of America*, 105(6), 3104–3113. DOI: 10.1785/012010358.

Ishimoto M., Iida K., 1939, Observations sur les seisms enregistrés par le microseismograph construit dernièrement (I), *Bulletin of the Earthquake Research Institute, University of Tokyo*, 17, 443-478.

Kijko A., 2004, Estimation of the maximum magnitude earthquake m_{max}. *Pure and Applied Geophysics*, 161, 1-27. DOI 10.1007/s00024-004-2531-4

Kijko A., Smit A., 2014, Extension of the Aki-Utsu b-value Parameter for incomplete Catalogues. Eurupean Geosciences Union, EGU2014-4959, Extreme events, multi-hazard and disaster risk assessment.

Kostoglodov V., Bandy W., 1995, Seismotectonic constraints on the convergence rate between the Rivera and North American plates. *Journal Geophysical Research*, 100, 17977–17989. DOI:10.1029/95JB01484.

Kostoglodov V., Pacheco J. F., 1999, Cien años de sismicidad en México. Instituto de Geofísica, UNAM.

Kramer Y., 2014, Minimum sample size for detection of Gutenberg-Richter's b-value. arXiv:1410.1815 [physics.geo-ph]

Lomnitz C., 1974, Global tectonics and earthquake risk. *Elsevier Scientific Publishing Company*, 320 pp.

Lomnitz-Adler J., Lomnitz C., 1979, A modified form of the Gutenberg-Richter magnitude-frequency relation. *Bulletin of the Seismological Society of America* 69: 1209-1214.

Márquez Ramírez V., 2012, *Análisis multifractal de la distribución espacial de sismicidad y su posible aplicación premonitora. Exploración de un posible mecanismo para la fractalidad mediante modelado semiestocástico*. PhD Thesis, Programa de Posgrado en Ciencias de la Tierra, Centro de Investigación Científica y de Educación Superior de Ensenada, Baja California, México.

Mitos y realidades, 2019, in Sismos y Volcanes CDMX for Apple IOS [Mobile application software]. Universidad Nacional Autónoma de México. Retrieved from Apple store. Consulted November 15, 2019.

Nava F. A., Márquez-Ramírez V. H., Zúñiga F. R., Ávila-Barrientos L., Quinteros C. B., 2017a, Gutenberg-Richter b-value maximum likelihood estimation and sample size. *Journal of Seismology*, 21, 127-135. https://doi.org/10.1007/s10950-016-9589-1

Nava F., Ávila-Barrientos L., Márquez-Ramírez V., Torres I., Zúñiga F., 2018, Sampling uncertainties and source b likelihood for the Gutenberg-Richter b-value from the Aki-Utsu method. *Journal of Seismology*, 22, 315-324. DOI: 10.1007/s10950-017-9707-8.

Núñez-Cornú J., Córdoba D., Dañobeitia J., Bandy W., Ortiz M., Figueroa B., Núñez D., Zamora-Camacho A., Espíndola J., Castellón A., Escudero C., Trejo-Gómez E., Escalona-Alcázar F., Suárez C., Nava F., Mortera C., TsuJal Working Group; 2016. Geophysical Studies across Rivera Plate and Jalisco Block, Mexico: TsuJal Project, *Seismological Research Letters*, DOI: 10.1785/0220150144

Olsson R., 1999, An estimation of the maximum b-value in the Gutenberg-Richter relation. *Geodynamics* 27, 547-552.

Öncel O. A., Wilson T. H., Nishizawa O., 2001, Size scaling relationships in the active fault networks of Japan and their correlation with Gutemberg-Richter b values. *Journal of Geophysical Research*, Vol. 106, No. B10, Pp. 21,827-21,841.

Pérez-Campos X., Young H. K., Husker A., Davis P., Clayton R., Iglesias A., Pacheco J., Singh S., Manea V., Gurnis M., 2008, Horizontal subduction and truncation of the Cocos Plate beneath central Mexico. *Geophysical Research Letters*, Vol. 35, L18303, DOI:10.1029/2008GL035127

Parzen E., 1960, Modern probability theory and its applications. J Wiley & Sons, Inc, Japan, 464pp.

Richter C., 1958, Elementary seismology. W H Freeman and Co, USA.

Scholz C., 1968, The frequency-magnitude relation of microfracturing in rock and its relation to earthquakes. *Bulletin of the Seismological Society of America*, 58:399–415

Shaw E., Carlson J. M., Langer J., 1992, Patterns of Seismic Activity Preceding Large Earthquakes. *Journal of Geophysical Research*, Vol. 97, No. B1, Pages 479-488.

Utsu T., 1965, A method for determining the value of b in a formula log n = a - bM showing the magnitude-frequency relation for earthquakes, *Geophysical Bulletin of the Hokkaido University*, 13, 99–103.

Utsu T., 1999, Representation and Analysis of the Earthquake Distribution: A Historical Review and Some New Approaches. *Pure and Applied Geophysiscs*, 155, 509-535.

Wyss M., Wiemer S., 2000, Change in the probability for earthquakes in southern California due to the Landers magnitude 7.3 earthquake. *Science*, Vol. 290, 1334

Zúñiga F. R., Reyes M. A., Valdés C. M., 2000, General overview of the catalog of recent seismicity compiled by the Mexican Seismological Survey. *Geofísica Internacional*. 39 (2), 161-170.

Original paper

PRESENT-DAY STRESS STATE IN NORTHWESTERN SYRIA

Mohamad Khir Abdul-Wahed*[1], Mohammed Alissa[2]

Received: September 3, 2018, accepted: July 7, 2020; online publication: October 1, 2020

RESUMEN

Para estudiar la tectónica activa y el patrón de estrés en el límite de placas convergentes de Arabia-Eurasia, el este del Mediterráneo de Siria nororiental es un área clave. Este estudio tiene como objetivo delinear el régimen de estrés actual en esta región, utilizando las soluciones de plano de falla de los eventos más grandes registrados por la Red Sismológica Nacional de Siria, de 1995 a 2011. Se obtuvo un conjunto de datos de soluciones de plano de falla para 48 eventos que tienen al menos 5 polaridades de onda P. El régimen tectónico para la mayoría de estos eventos es extenso y produce mecanismos normales de acuerdo con las configuraciones locales de las fallas sismogénicas en la región. Los mecanismos de deslizamiento son más escasos y están restringidos a ciertas áreas, como la extensión norte del sistema de fallas del Mar Muerto. Los resultados del estudio actual revelan las variaciones espaciales en la orientación de la tensión horizontal máxima (SHmax) en la región noroeste de Siria. Estas variaciones resaltan el papel de las principales zonas de cizallamiento geométricamente complejas en el patrón de tensión actual de esta región. Sin embargo, estos resultados, independientemente de la magnitud relativamente pequeña de los eventos estudiados, proporcionan una imagen de las desviaciones de esfuerzos locales que se han estado produciendo actualmente a lo largo de las fallas activas locales.

PALABRAS CLAVE: soluciones de plano de falla, régimen tectónico, región costera, Siria.

ABSTRACT

Northwestern Syria is a key area in the eastern Mediterranean to study the active tectonics and stress pattern across the Arabia-Eurasia convergent plate boundary. This study aims to outline the present-day stress regime in this region using the fault plane solutions of the largest events recorded by the Syrian National Seismological Network from 1995 to 2011. A dataset of fault-plane solutions was obtained for 48 events having at least 5 P-wave polarities. The tectonic regime for most of these events is extensional and produces normal mechanisms in agreement with the local configurations of the seismogenic faults in the region. Strike-slip mechanisms are more scarce and restricted to certain areas, such as the northern extension of the Dead Sea fault system. The results of the current study reveal the spatial variations in the orientation of maximum horizontal stress (SHmax) across the northwestern Syria region. These variations highlight the role of main geometrically complex shear zones in the present-day stress pattern of

*Corresponding author: cscientific3@aec.org.sy

[1]Dept. of Geology, The Atomic Energy Commission of Syria, Damascus P.O. Box 6091, Syria

[2]Higher Institute of Earthquake studies and Research, Damascus University, Damascus, Syria

This region. However, these results, regardless of the relatively small magnitude of the studied events, provide a picture of the local stress deviations that have currently been taking place along the local active faults. KEYWORDS: fault plane solutions, tectonic regime, coastal region, Syria.

INTRODUCTION

Syria is located in the northern part of the Arabian plate (figure 1). It is bounded from the west by the northern section of the Dead Sea Fault System (DSFS). In northwestern Syria, the DSFS intersects the Eastern Anatolian Fault System (EAFS), both of which comprise the northern border of the Arabian plate. The seismic activity in this area is characterized by a widespread moderate level of seismicity resulting from the complex interaction between the DSFS and the EAFS (Barazangi *et al.*, 1993). Neotectonic map of Syria (Rukieh *et al.*, 2005), illustrates the evolution of the northwestern boundary zone of the Arabian plate.

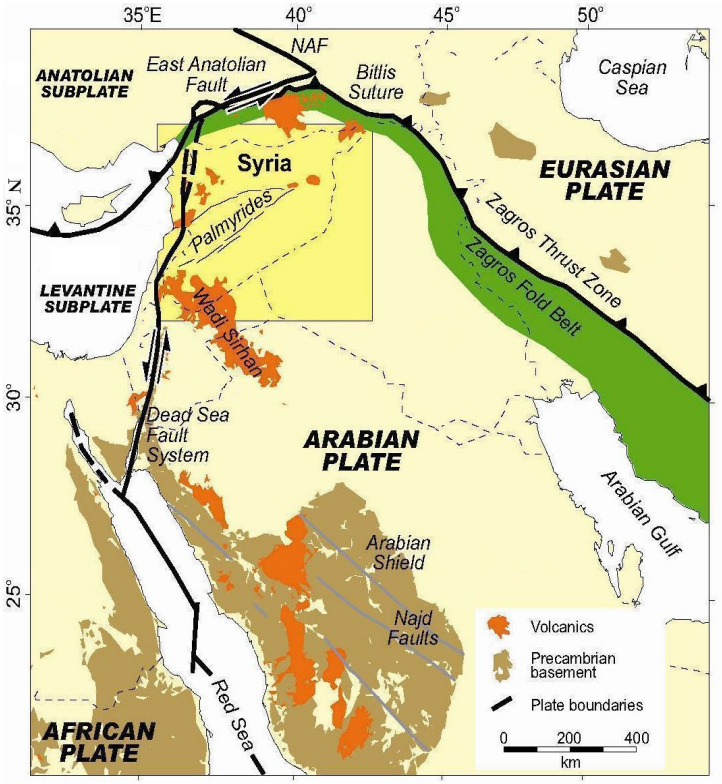

Figure 1. Tectonic regional map of Arabian plate (modified from Brew *et al.* 2001). The rectangle indicates the location of figure 2.

The EAFS delineates the boundary between the Anatolian and Arabian plates. It is a 600 km long SW-NE trending fault zone associated with thrusting and left-lateral faulting (Aktug *et al.*, 2016). Although the EAFS was relatively quiet during the last century, historical seismicity shows that the EAFS is capable of producing devastating earthquakes (Ambraseys, 1989). The observed faulting mechanisms along the EAFS are predominantly left-lateral strike-slip in good correlation with the deformation pattern derived from regional GPS data (Bulut *et al.*, 2012). Kartal *et al.* (2013) have used the fault plan solutions of 127 earthquakes with a magnitude greater than 4.0,

that occurred along the EAFS, to determine principal stress axes. According to their results, the maximum stress axis (σ1= -172.9°/7.5°) and the minimum stress axis (σ3=96.5°/3.2°) are in a horizontal position, which indicates a strike-slip faulting.

The DSFS is an important tectonic feature, which accommodates the relative sinistral motion between the African and Arabian plates (Reilinger and McClusky, 2011). This system has been regarded as an active plate boundary since the late Cenozoic through the present-day (Barazangi *et al.*, 1993). The previous works on the focal mechanisms of the past events in Syria attest the left-lateral pattern of active deformation with a minor component of normal faulting. Abdul-Wahed and Al-tahhan (2010) outline the seismological active zones in Syria using the focal mechanisms of the largest events (MC≥3.5 Mc: coda magnitude, Bulletins of SNSN, 1995-2011) recorded by the Syrian National Seismological Network (SNSN) from 1995 to 2003. Most of these events had strike-slip mechanisms in agreement with the configuration of the seismogenic belts in Syria. Focal mechanisms of moderate-to-large earthquakes show a sinistral motion along the DSFS (Baer et. al., 1999; Klinger et. al., 1999; Salamon *et al.*, 1996). Salamon *et al.* (2003) have calculated the fault plane mechanisms of all ML ≥ 4 (ML: Local magnitude) recorded seismicity in the eastern Mediterranean region during the 20th century. They found anomalous solutions that confirm the complexity of the deformation processes along the DSFS. The state of stress is characterized by the coexistence of a normal faulting stress regime with the primarily strike-slip one (Palano *et al.*, 2013). Kartal *et al.* (2013), have used the fault plane solutions of 16 earthquakes with a magnitude greater than 4.0, that occurred along the DSFS, to determine principal stress axes. According to their results, the maximum stress axis (σ1= -35°/27.9°) and the minimum stress axis (σ3= 61.8°/12.7° are in a horizontal position, which indicates strike-slip faulting with a normal component. Omar and Kiki-Khersy (2016) have calculated the focal mechanism of 35 events that occurred in Syria during the period 2009-2011 with magnitude ML ≥ 2 and determined the maximum stress axis (σ1= 55°/46°) in the north of Syrian coastal range. They found the focal mechanisms and the present-day stress field are highly affected by the complexity of geological structures. Alissa *et al.* (2018) have found most of recorded events (1995-2011) in the Syrian coastal region had normal mechanisms in agreement with the local active faults.

In a review of the slip and seismicity of the DSFS, Garfunkel (2011) concludes that the slip rate is slowing from an average rate of 6–7 mm/year over the last 5 Ma to 4–5.5 mm/year in the Pleistocene together with a slight eastward shift of the Euler pole of rotation between Sinai and Arabia. Aktug *et al.* (2016) found that while the slip rate of the EAFS is nearly constant (~10 mm/yr) to the north of Türkoğlu, it then decreases to 4.5 mm/yr in northwestern Syria and the slip rate on the northern part of DSFS was also found to be 4.2±1.3 mm/yr, consistent with earlier studies.

Although the tectonostratigraphic evolution of the Arabian platform in Syria has been studied using different approaches such as structural geology and stratigraphy, there have been few attempts to analyze the stress regime (Zanchi *et al.*, 2002; Al-Abdalla, 2008). Al-Abdalla *et al.*, 2010 characterize the polyphase tectonic evolution of the northwestern Arabian plate in Syria since Late Cretaceous time. They found this region experienced a NNW–SSE directed regional compression from the end of the Miocene, and until now. They reconstruct the regional palaeostress and tectonic evolution. Overall, the tectonic deformation in the eastern Mediterranean is controlled mainly by episodic collisions,

openings, and movements on the plate boundaries that closely bound the area (Barazangi *et al.*, 1993).

The recent instrumental seismicity revels that northwestern Syria has relatively high levels of seismic activity in addition to the long history of earthquakes (Abdul-Wahed and Asfahani, 2018). Besides, the tomographic inversion at 12 seismic stations distributed in the northwestern Syria, exhibit the crustal structure is highly heterogeneous down to the upper mantle depths (Salah, 2019). Therefore, the northwestern Syria region is a key area in the eastern Mediterranean. The main purpose of this work is to evaluate the tectonic regime and the present-day stress in northwestern Syria by calculating the focal mechanism of the strongest events, and then, create the stress map using the derived maximum horizontal stress (SHmax). This will improve and strengthen our knowledge of the actual seismotectonic deformations taking place now, and the seismic hazard assessment and development of appropriate risk-mitigation strategies.

Recent seismic activity in Syria

The SNSN, operated since 14 January 1995, consists of twenty-seven weak motion short period (1 Sec) stations of ~50 km seismograph spacing. The network configuration has been designed to monitor all discernable earthquake activity along the DSFS and its related branches in Syria and nearby Lebanon. Few years later, the network grew up and now covers all the country. The geographical distribution of the seismic stations of SNSN is shown in figure 2. More details about the SNSN can be found in (Dakkak *et al.*, 2005). During the study period 1995-2011, about 5000 local events have been recorded by the SNSN (Bulletins of SNSN, 1995-2011). The magnitude has been calculated from the coda wave duration via the formula (Bulletin of SNSN, 1995-2012):

$$MC = -3.0 + 2.6 * \log (T) + 0.001 * D \qquad (1)$$

where T is the coda duration (in sec) and D is the epicentral distance (in km). Most of the recorded events are micro-earthquakes (Mc<3.0,), where their average magnitude is approximately 2.0. The fitting of Gutenberg and Richter relation to the observed frequency-magnitude distribution has shown a magnitude completeness about Mc=2.5 (Abdul-Wahed and Asfahani, 2018). The instrumental seismicity, during the period 1995-2011, has shown that the earthquake activity is mostly made up of low magnitude events (Abdul-Wahed and Al-Tahan, 2010; Abdul-Wahed et. al., 2011). Consequently, this may indicate that the seismic activity during that period is passing with a relative quiescence in comparing with the historical earthquakes (Abdul-Wahed and Asfahani, 2018). The epicentral map (figure 2) presents the geographical distribution of the seismic activity, which is clearly concentrated on northwestern Syria. The EAFS, including Lattakia -Killis Faults System (LKFS) (figure 3), could be considered the highest instrumental seismicity in Syria (Abdul-Wahed and Asfahani, 2018).

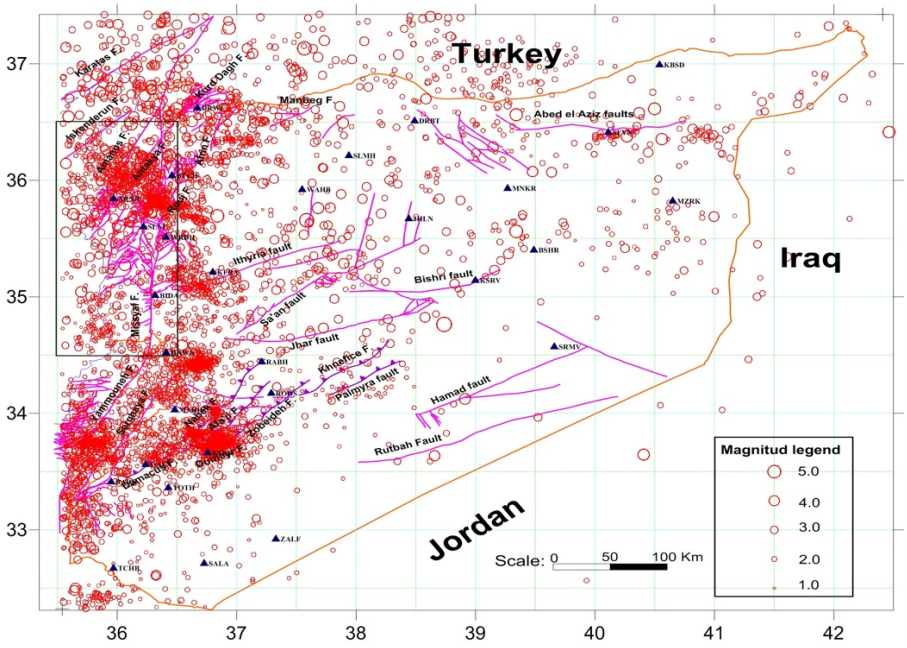

Figure 2. The epicentral map showing geographical distribution of the seismic activity During the study period 1995-2011 (modified from Abdul-Wahed and Asfahani, 2018). The rectangle indicates the study region and the triangles indicate the seismic stations of SNSN.

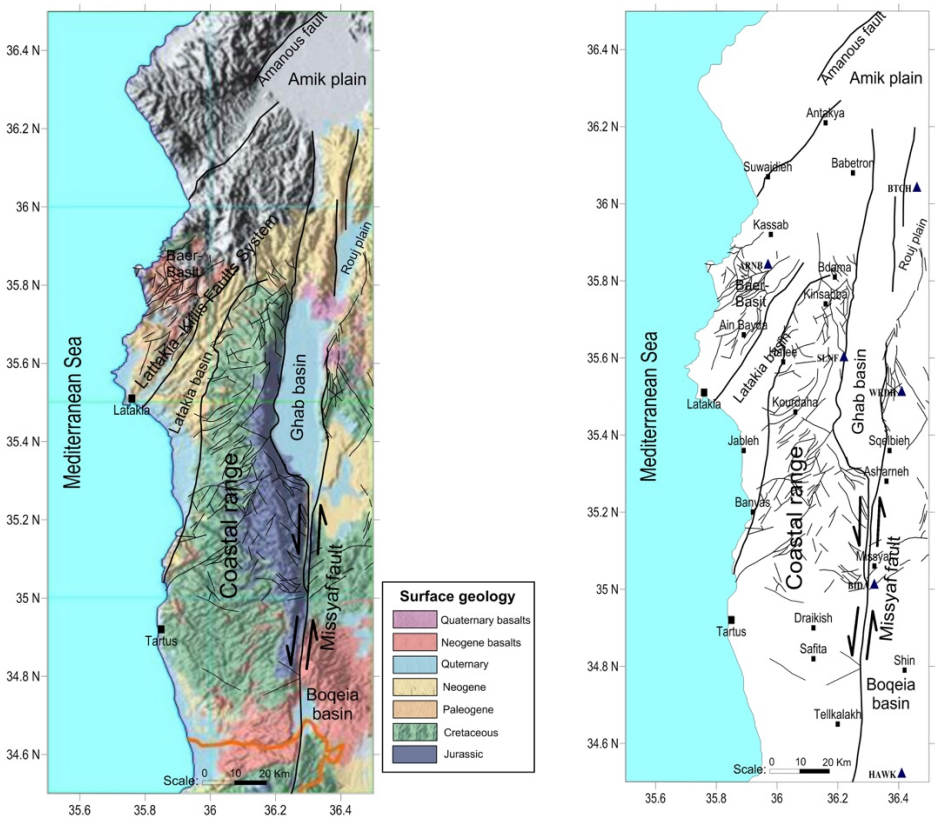

Figure 3. Maps of the study region: surface geology map (left), and map of faults and the main cities. The solid rectangles indicate the cities and the triangles indicate the seismic stations of SNSN.

STUDY REGION

The study region is northwestern Syria and extends between longitudes (35º.30' - 36º.30' E) and latitudes (34º.30' - 36º.30' N) as shown in figure 2. It includes two major fault systems: EAFS and DSFS, two basins: Ghab and Lattakia, and a big anticline uplift: the coastal range (figure 3). In this setting, the main tectonic features consist essentially of three main fault trends: the northeast–southwest EAFS, north-south DSFS, and east-west secondary faults trends. The northwestern boundary zone between Arabian and Anatolian plates is represented by southwestern termination of the EAFS striking to the SW–NE, and, nappes and ophiolites of the Bassit block. The EAFS in study region is a system of oblique (sinistral strike-slip with a reverse component) faults generating structures corresponding to shortening and sinistral slip (Rukieh *et al.*, 2005). The DSFS is a left-lateral strike-slip fault with smaller normal component of motion extending northward from the Red Sea to the EAFS into the Amik Basin, bounding the African and Arabian plates (Brew et. al, 2001). The northern part of the DSFS, oriented N–S on average, is located in the study region and bounds the western side of the Ghab Basin. Examination of the 20th-century earthquakes shows no records of large earthquakes on the northern part of the DSFS. The coastal area includes a big anticline uplift of the Syrian Coastal Range (SCR), which ruptured by several faults. An extensive karst terrain, a gently dipping (about 10º) western limb, and a chaotic, steep, eastern limb where Triassic strata are exposed, characterize the area. The SCR rises dramatically by ~1300 m, exposing Jurassic, and even uppermost Triassic, strata. Clearly, the SCR uplift has been very strongly modified by the propagation of the DSFS through northwest Syria, and the related formation of the Ghab basin. It began in the latest Cretaceous with regional compression causing folding and uplift. The Plio-Quaternary Ghab basin formed near what was presumably the crest of the pre-Pliocene Coastal Range uplift. This created the extremely steep scarp on the eastern face of the SCR alongside the Ghab basin (Brew, 2001). The Ghab basin has been formed as a pull-apart basin on the DSFS since earliest Pliocene time and opened in response to a left-step in the fault, although sinistral motion fails to be fully transferred across the basin (Brew et. al, 2001). The ophiolite zone of the Bassit block had been thrust in the Mastrichtian (Knipper *et al.*, 1988). The nappes are offset by the eastern trending dextral faults (Rukieh *et al.*, 2005). The southeastern boundary of the Bassit block is represented by the LKFS (Trifonov *et al.*, 1991) that limits the Lattakia Neogene basin from the NW. The LKFS is an oblique sinistral-thrust fault system, which is cut and offset by the DSFS, continues to the NE of the Ghab Basin by Aafrin lineament (Trifonov *et al.*, 1991).

DATA AND METHODOLOGY

During the period 1995-2011, the SNSN has recorded about 1800 local events in the study area. Hypocentral locations were determined at the National Earthquake Center (NEC) using the program (Seisan 10.3, 2015). The accuracy of the events' location is a critical factor for reliably identifying the focal mechanism. To improve the accuracy of location, the records were filtered, in order to get the best signal-noise ratio, where all P and S phases are manually picked. As a result, the number of arrival time readings is increased. Events are relocated with the new arrival times using the Seisan program and the last velocity model (Ibrahim *et al.*, 2012). The first motion of P waves (P polarities) are carefully examined and visually inspected in order to get the most out of them. Only 48 events, comprising at least 5 polarities, could be adequate to calculate the focal mechanism. The low seismicity in Syria and the insufficient coverage of seismic stations of SNSN (Dakkak *et al.*, 2005) limit the number of fault plane solutions that can be obtained from the available records. We, therefore, apply a probabilistic method (Zollo & Bernard, 1991), in

addition to Seisan program. In this context, a Visual Fortran program, "Meca3" (Abdul-Wahed, 2018), has been realized in order to evaluate the tectonic regime and the present-day stress in northwestern Syria by calculating the focal mechanism of some strongest events, and then, to derive the maximum horizontal stress (SHmax). The program "Meca3" is based on the following concepts:

1. Focal mechanisms background

Several methods for determining the focal mechanism solution, such as the first motion of P waves (P polarities), are using the radiation pattern of seismic rays that expresses the orientation of the active fault and the slip direction. P-waves radiate relative to the focus with compressive or dilatational initial motion. The observed P polarities are then projected backwards along the ray path onto a focal sphere, which is thought to be a point source. Two angles can identify any P-wave ray path leaving the source toward the recording stations: the azimuth from the source and the angle of emergence (Aki and Richards, 1980). When Seisan program locates a seismic event, it calculates these angles for each recording station using the crustal model and the geographic position of the seismometer. The program "Meca3" imports these angles and the observed P polarities from Seisan program to project the P polarities onto the focal sphere. When all available P polarities are plotted in the lower hemisphere of a stereographic projection, two orthogonal nodal planes separating compressive from dilatational polarities can be drawn by the probabilistic method (Zollo & Bernard, 1991). The axes of maximum shortening and maximum lengthening bisecting the quadrants are known as the P and the T axes, respectively (figure 4). The axis formed by the intersection of the two nodal planes is called the B- or the null axis. It is worth to note these principal strain axes must not necessarily coincide with the principal stress axes. The reliability of calculated fault plane solutions could be evaluated by establishing an adequate quality factor as illustrated later.

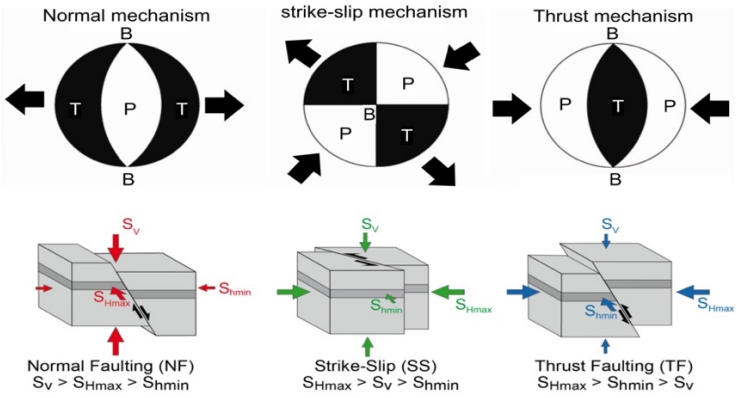

Figure 4: Orientation of the principal strain axes (P, T, and B) of focal mechanism and the corresponding stresses axes (Sv, SHmax, and Shmin) (modified from Heidbach *et al.*, 2016).

2. Faulting type

The program "Meca3" determines the faulting type using Frohlich triangle (Frohlich, 1992). Frohlich triangle is a quantitative graphical method for displaying focal mechanisms using the dip angles of T, B and P axes. This diagram is to characterize earthquake focal mechanisms as

thrust, strike-slip, or normal in terms of the dip angles with respect to horizontal of their T, B, and P axes, where the vertices of triangle represent normal, thrust, and strike-slip focal mechanisms. The Frohlich diagram offers a manageable way to visualize the dominant style of faulting in a given region. Besides this, it also provides a way for determining the proportions of thrust, normal, and strike-slip motion for any earthquake focal mechanism, as a secondary component of faulting.

3. Tectonic regime and stress axes

Stress regime could be inferred from the more numerous focal mechanism and fault slip data (Célérier, 2010). As the focal mechanism gives information on the faulting type, normal faulting (NF); strike-slip (SS); thrust faulting (TF), the relative magnitudes of SHmax, Shmin and SV are known. Following Anderson (1951), these three stress regime categories can be defined on the basis of relative stress magnitudes: extensional stress regime (Sv>SHmax>Shmin) corresponding to normal dip-slip faulting; wrench stress regime (SHmax>Sv> Shmin), corresponding to strike-slip faulting with dominantly horizontal slip; and compressive stress regime (SHmax>Shmin>Sv), corresponding to thrust dip-slip faulting (figure 4). Besides the NF, TF, and SS categories, combinations of NF with SS (transtension (NS)) and TF with SS (transpression (TS)) exist (Zoback, 1992). In these categories, the stress field could be transitional between regimes; where two of the stresses are approximately equal in magnitude. A stress field of the form Sv≈SHmax>>Shmin can produce a combination of both normal and strike-slip faulting, whereas a stress field of the form SHmax>>Shmin≈Sv produces a combination of strike-slip and thrust faulting. NS is appropriate where the maximum stress or P-axis is the steeper plunging of the P- and B-axis. TS is appropriate where the minimum stress or T-axis is the steeper plunging of the B- and T-axis. The plunges (pl) of P-, B-, and T-axis are used to assign the appropriate stress regime (Célérier, 2010).

4. Stress methodology

A focal mechanism describes the geometry and mechanism of the faulting during a given earthquake and is widely used in order to derive stress tensor distribution (Müller *et al.*, 1992; Heidbach *et al.*, 2016; Rajabi *et al.*, 2017). The orientation of the maximum horizontal stress (SHmax) could be derived from the principal strain axes (McKenzie, 1969). The program "Meca3" allows obtaining the true orientations of the horizontal principal stresses (SHmax and Shmin) according to (Frohlich, 1992; Zoback, 1992). The method of determining SHmax azimuth is based on plunges of P, B, and T axes, where these plunges have been used to divide the data into five main stress regime categories. The mechanism is thrust (TF) if it possesses a vertical or near-vertical T axis (figure 4), strike-slip (SS) if it has a vertical or near-vertical B axis, and normal (NF) if it has a vertical or near-vertical P axis (Frohlich, 1992). Moreover, if the P axis is closest to vertical, and the B axis is next closest, the mechanism is (NS) 'normal with a component of strike-slip'. Also, if the T axis is closest to vertical, and the B axis is next closest, the mechanism is (TS) ' thrust with a component of strike-slip.'

The cutoff values for plunges (dip°) of measured P, T, and B axes for these various categories are used to infer the maximum horizontal stress (SHmax) orientation (figure 4). For example, the SHmax orientation is taken as the azimuth of the B axis in case of a pure normal faulting regime (NF), where the P dip> 55° (Frohlich, 1992). While the SHmax orientation is taken as the azimuth of the P axis in case of a pure thrust faulting regime (TF), where the T dip> 55°. It is

taken as the azimuth of the P axis in case of a pure strike-slip faulting regime (SS), where the B dip> 55°.

RESULTS AND DISCUSSIONS

1. EPICENTER MAP

In order to get an accurate location of the 48 events, all P and S phases are carefully inspected and manually picked. Events were relocated with the new arrival times using the Seisan program. As a result of increasing the number of arrival time readings, the errors become less than 5 km in most events. The epicenter map (figure 5) exhibits the majority of the events could be related to EAFS and some few events could be related to the north extensions of DSFS. Regarding the magnitude, the 48 events are nearly of low magnitude, where the average magnitude is about 1.8.

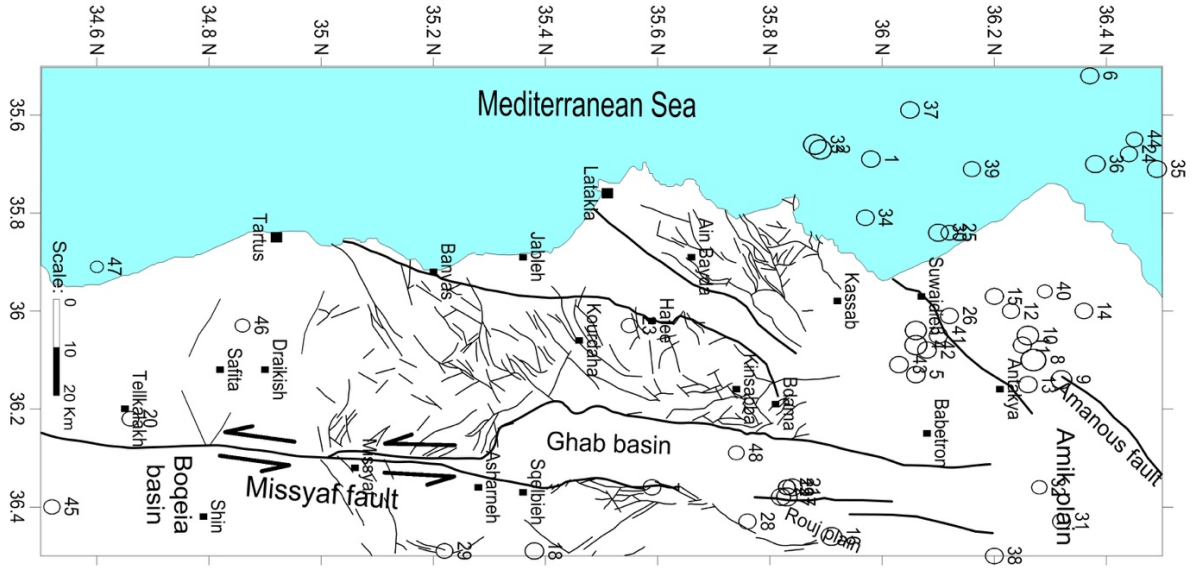

Figure 5. The epicenter map of the 48 events comprising at least 5 polarities. The events are numbered to be referenced in the next figures.

2. FAULT PLANE SOLUTIONS

The P polarities are also carefully inspected in order to get the most out of them. The 48 events, possessing at least 5 polarities, could be adequate to calculate the focal mechanism. The calculated fault plane solutions, depicted in figure 6, revel normal faulting for the majority of events as indicated by Alissa *et al.* (2018). As shown in figure 6, some few events have strike-slip faulting and are located along the north extensions of DSFS and along the EAFS. The thrust faulting is very scarce, where only three events have reverse focal mechanisms. However, it is necessary to evaluate the reliability of fault plane solutions before any further interpretations.

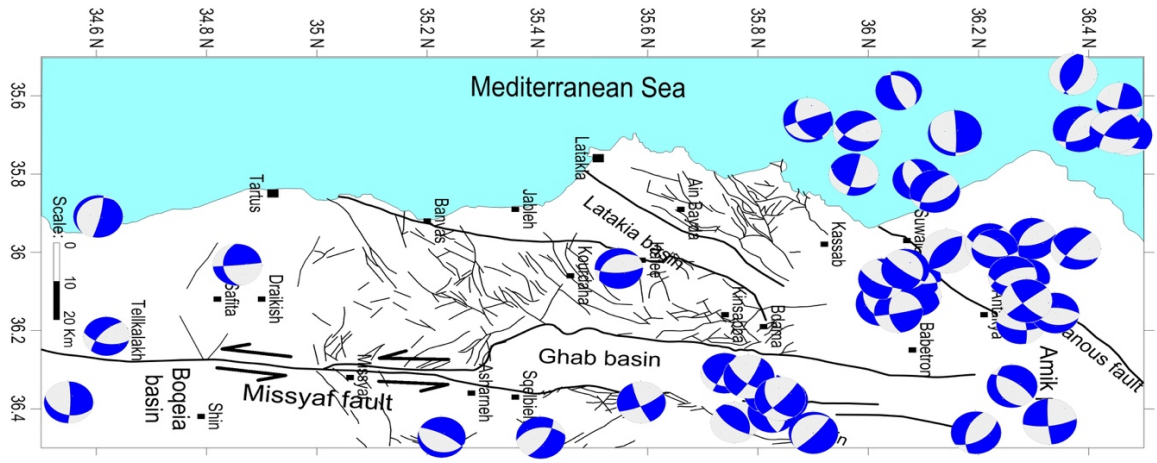

Figure 6. Map of the calculated fault plane solutions of the 48 events comprising at least 5 polarities.

3. Reliability

Using a Quality Factor (QF) is important for evaluating the data and the fault plane solutions, particularly because we mostly dealt with solutions based on few data. This QF is established in this study by by using many criteria known in the literature (Salamon *et al.*, 2003; Kilb and Hardebeck, 2006; Boncio and Bracone, 2009; Abdul-Wahed and Al-tahhan, 2010). For each criterion, we assigned a number of points: 3 for good, 2 for fair, and 1 for poor. The sum of these points then defines the QF. The used criteria are as follows:

location error (0: error>15 km, 1: error=10-15 km, 2: error=5-10 km, 3: error<5 km);

azimuthal distribution of data on the lower-hemisphere projection (0: distributed in one quadrant, 1: in two quadrants, 2: in three quadrants, 3: in four quadrants);

homogeneity of distribution of the data, where the more widely the data are spread, the better the focal sphere is represented (0: concentrated, 1: poor spread, 2: fair spread, 3: good spread);

the total number of P polarities used for the construction of focal mechanism (0: polarities less than 5, 1: polarities 5-10 (poor), 2: polarities 10-15 (fair), 3: polarities more than 15 (good));

the number of reversed P polarities. As this number increases, the reliability of solution decreases (0: reversed polarities more than 30%, 1: reversed polarities 20-30%, 2: reversed polarities 10-20%, 3: reversed polarities less than 10%).

average error in calculating the fault plan solution. It summarizes the range of uncertainties of the strike, dip and rake (0: error>30°, 1: error=20-30°, 2: error=10-20°, 3: error<10°);

Then, the sum of these criteria defines the QF as the reliability of a solution. The longer QF, the reliability of a solution is better, where the maximum of QF can reach 18 points. A solution could be considered: good when QF ranges 12-18 points, fair when QF ranges 6-12 points, and poor when QF ranges 0-6 points. Figure 7 shows the QF of calculated fault plane solutions using the above criteria. The average QF is 12.63 with a standard deviation of 2.39. As a consequence, the calculated fault plane solutions could be reasonable depending on the QF.

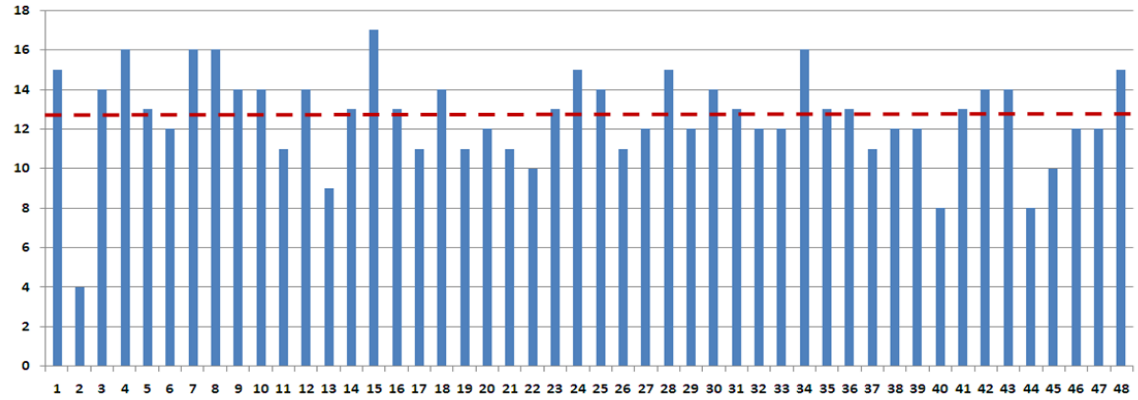

Figure 7. The Quality Factor (QF) of calculated fault plane solutions. The horizontal axis indicates the index of the analyzed event. The vertical axe indicates the corresponding QF from 18. The dashed line indicates the average of QFs.

4. Assessment of Tectonic Regime

Projection the dip angles of T, B and P axes of the processed events onto Frohlich triangle (figure 8) reveals about 54% of events have normal faulting (NF) and about 23% have normal faulting with a component of strike-slip. Thus 77% of events could be corresponding to extensional stress regime (Sv>SHmax>Shmin). In view of this fact, it could be reasonable to plot the tension axes (T) of these events onto the study area map (figure 9). The resulting map shows the tensional strain directions in the seismic focuses under the effect of a dominant extensional stress regime. The verification of dip angles of their T axes points out the horizontality of these axes and thus the tension axes (T) could be in concordance with the minimum horizontal stress (Shmin). We can note many events on the northern extension of DSFS show a T-axis approximately in the N-S direction. These might be produced by a probable local tension in the DSFS margin. On the other side, the triangle diagram shows that only 6% of events have strike-slip faulting, which indicates the wrench stress regime is not a dominant regime in the study area and during the study period (1995-2011).

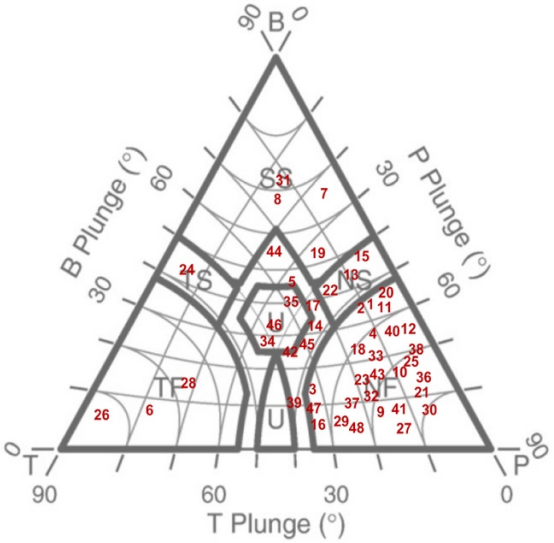

Figure 8. Projection the dip angles of T, B and P axes of the 48 events onto Frohlich triangle. The events are numbered in corresponding to the other figures.

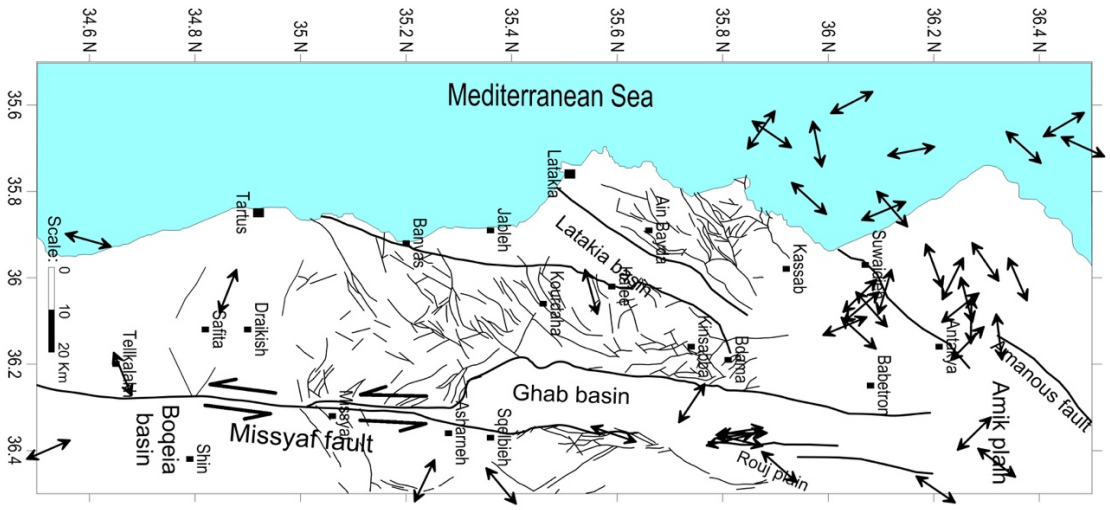

Figure 9. Map showing tension axes (T) according to fault plane solutions of only the extensional events.

5. Stress map

In order to study the pattern of seismotectonic deformation in the study area, a detailed map of stress orientations has been established. The orientations of the maximum horizontal compressional stress SHmax have been obtained according to (Frohlich, 1992; Zoback, 1992). Referring to the concept of the World Stress Map, the stress data is assigned a quality between "A" and "E", with "A" being the highest quality and "E" the lowest (Heidbach *et al.*, 2016). These quality classes are defined through the standard deviation of SHmax. A-quality means that the orientation of SHmax is accurate to within ±15°, B-quality to within ±20°, C-quality to within ±25°, D-quality to within ±40°, and E-quality data have standard deviations greater than 40°. In general, A-, B- and C-quality stress indicators are considered reliable for the use in analyzing stress patterns and the interpretation of geodynamic processes (Heidbach *et al.*, 2016). According to the World Stress Map quality ranking, single focal mechanisms (FMS) of events (M≥2.5) are given a C-quality. However, the low magnitude events (M≤2.5) are given a D-quality. The CASMO, website based software (Heidbach *et al.*, 2016), has been used to create the stress map using the derived maximum horizontal stress (SHmax) from the FMS (figure 10). Different tectonic regimes are characterized by different symbol colors. NF and NS data are shown in red, SS data in green, and TF and TS data in blue. Data with an unknown regime is shown in black. The results reveal large spatial variations of SHmax orientation across northwestern Syria from NE-SW to NW-SE. However, most of results exhibit an extensional stress regime.

6. General discussions

Previous studies of focal mechanisms of moderate-to-large earthquakes show a sinistral motion along the DSFS (Baer et. al. 1999; Klinger et. al. 1999; Salamon et. al. 1996) and along the EAFS (Bulut *et al.*, 2012; Kartal *et al.*, 2013; Aktug *et al.*, 2016). However, the results of the current study demonstrate that the extensional stress regime is dominant in northwestern Syria and the majority of events reflect normal faulting. Some few events have strike-slip faulting and are located along the north extensions of DSFS and along the EAFS. In order to get a better understanding of the local stress regime in the study area, the following notes should be taken into consideration:

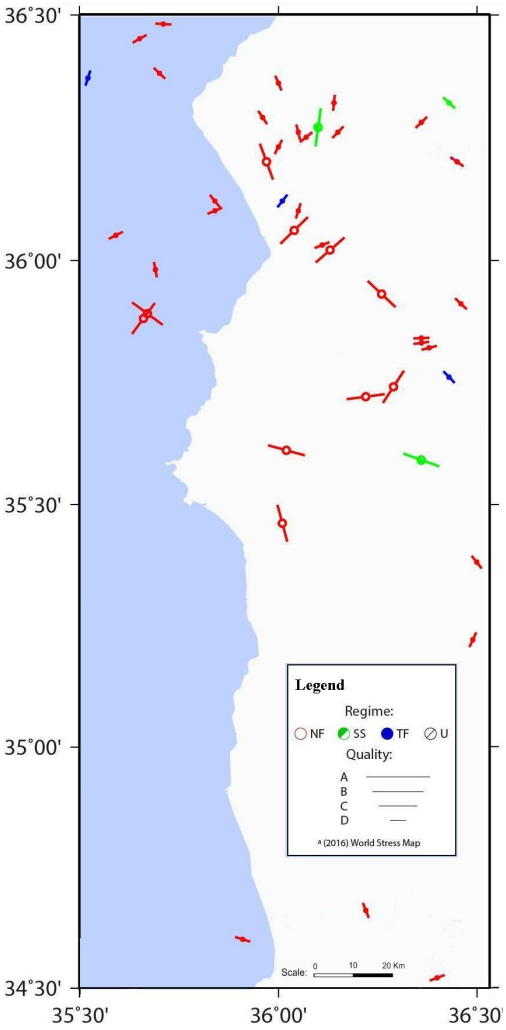

Figure 10. Map showing stress orientations of the maximum horizontal compressional stress SHmax, created using CASMO website based software (Heidbach *et al.*, 2016). The tectonic regimes are indicated by different symbol and colors: NF and NS in red, SS in green, TF and TS in blue, and. an unknown regime in black.

During the period (1995-2011), a seismic gab has been observed along the north extensions of DSFS. In fact, there has been a long-lasting absence of seismicity at northern DSFS, where this section is passing in quiescent status since about 850 years (Megrhaoui *et al.*, 2003). The EAFS was relatively quiet during the last century in comparison with historical seismicity (Aktug *et al.*, 2016). Furthermore, the south-west part of EAFS, which is located in the study region, has been regarded as silent during the instrumental period (Kartal *et al.*, 2013). These reasons could interpret the absence of the sinistral motion characterizing these main tectonic systems, and why the wrench stress regime is not a dominant regime in the study area.

The 48 events are nearly of low magnitude. Therefore, these events could be related to secondary small faults rather than the main regional faults. Consequently, the focal mechanisms of these events reflect the local stress regime. This reason could interpret the spatial variations of SHmax orientation across northwestern Syria.

In the study region, the published fault plan solutions are generally seldom and sparse (Salamon *et al.*, 2003; Abdul-Wahed and Al-tahhan, 2010; Omar and Kiki-Khersy, 2016). Referring to the World Stress Map Database Release 2016 (Heidbach *et al.*, 2016), the stress data are also very

scarce in northwestern Syria and no data found in western Syria (figure 11). While Kartal *et al.* (2013) determine principal stress axes along the EAFS, they have dealt the fault plan solutions of only 2 events with a magnitude greater than 4.0 that occurred in the north of the study region. As a consequence, the results of the current study could be considered as an updated overview of the actual stress regime and the seismotectonic setting in a key area in the eastern Mediterranean.

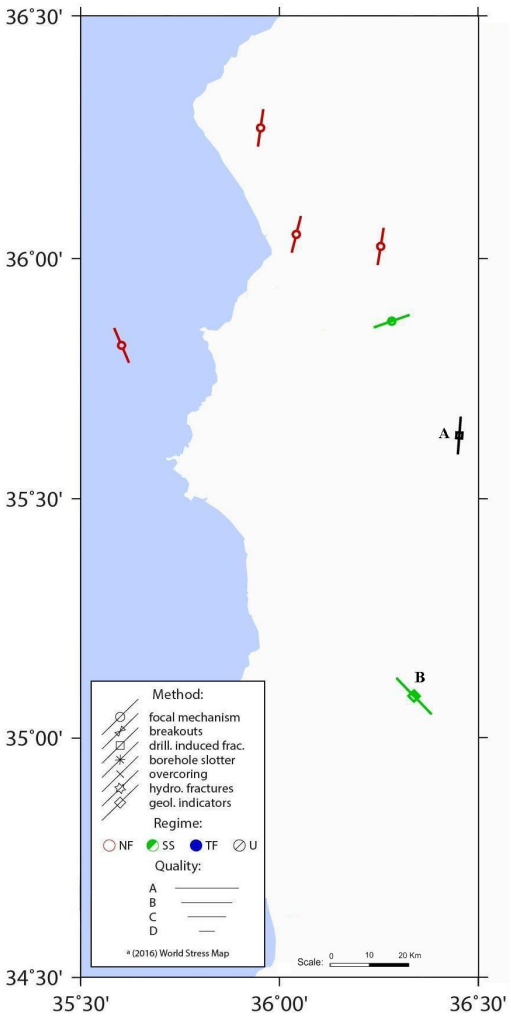

Figure 11. Map showing stress orientations of the maximum horizontal compressional stress SHmax of previous study and published on the World Stress Map (Heidbach *et al.*, 2016). This map has been created using CASMO website software. The stresses indicated by A and B are derived from geological indicators using website based software (Heidbach *et al.*, 2016). The tectonic regimes are indicated by different symbol and colors: NF and NS in red, SS in green, TF and TS in blue, and. an unknown regime in black.

CONCLUSION

Forty-eight seismic events, having at least five P polarities, occurred during the period (1995–2011) in northwestern Syria, have been studied to determine their source mechanisms. The established quality factor denotes the reliability of calculated fault plane solutions. In order to study the pattern of seismotectonic deformation, a detailed map of stress orientations has been established in the study area. Hence, the 48 single focal mechanism solutions are classified based

on the World Stress Map nomenclature and quality ranking. The results of the current study demonstrate that the extensional stress regime is dominant in northwestern Syria and the majority of events reflect normal faulting. The established stress map displays the orientations of the maximum horizontal compressional stress SHmax, which have large spatial variations. We can conclude that seismic activity reflects mostly the local stress regime in the study area rather than the regional regime. Furthermore, the results of the current study represent an updated overview of the actual stress regime and the seismotectonic setting in northwestern and western Syria using recent earthquake data (1995–2011). Our findings could be interesting for the scientific society, especially because of the scarce information available in the area of interest.

ACKNOWLEDGMENTS

The authors thank Dr. Ibrahim Othman for his generous supporting to accomplish this research. They thank the Syrian Earthquake Center (NEC), which provided us with digital seismic waveforms. The authors are grateful to Nazir Alyousef from the NEC for his kind help in data preparing and format conversion. Great thanks to Oliver Heidbach for mapping the maximum horizontal stress (SHmax) using his software (CASMO). They gratefully acknowledge the anonymous reviewers for their valuable comments and suggestions that substantially improved the quality of the manuscript.

REFERENCES

Abdul-Wahed M. K., (2018), Preparation of a computer program for calculating the focal mechanism of the recorded micro-earthquake in Syria. Internal report: AECS-1217, December 2018.

Abdul-Wahed M. K.and Asfahani J., (2018), The recent instrumental seismicity of Syria and its implications, *Geofísica Internacional* (2018) 57-2: 79-92.

Abdul-Wahed M. K., Asfahani J., Al-Tahan I., 2011, A combined methodology of multiplet and composite focal mechanism techniques for the identification of the seismological active zones in Syria. *Acta Geophysica*, 59, 967-992, DOI:10.2478/s11600-011-0024-2.

Abdul-Wahed M. K. & Al-Tahan I., 2010, Preliminary outlining of the seismological active zones in Syria. *Annals of geophysics*, 53, 1-9.

Aki K. & Richards P. G. (1980), Quantitative Seismology, Theory and methode. San Fransisco : W. H. Freeman and Co.

Aktug, B., Ozener, H., Dogru, A., Sabuncu, A., Turgut, B., Halicioglu, K., Yilmaz, O., Havazli, E.,Slip rates and seismic potential on the East Anatolian Fault System using an improved GPS velocity field, *Journal of Geodynamics*, (2016), http://dx.doi.org/10.1016/j.jog.2016.01.001

Al-Abdalla, A. 2008. Evolution tectonique de la plateforme arabe en Syrie depuis le Me´sozoı¨que. PhD thesis, Me´moire de the`se de l'Universite´ de Paris 6, Paris, 302 (in French).

Al Abdalla A., Barrier E., Matar A. & Muller C., (2010), Late Cretaceous to Cenozoic tectonic evolution of the NW Arabian platform in NW Syria, *Geological Society*, London, Special Publications 2010; v. 341; p. 305-327, doi:10.1144/SP341.15.

Alissa M., Abdul-Wahed M. K., Shoukeir N., Zeizafoun S., (2018), Using the seismic focal mechanism to evaluate the neotectonic along the active faults in the coastal region, Syria. Magazine of Albaath-University, Vol. 40, Nb. 54, PP. 129-151.

Ambraseys, N. N., (1989), Temporary seismic quiescence: SE Turkey, *Geophysical Journal International*, 96, 311-331.

Anderson E.M. (1951), The dynamics of faulting. Oliver & Boyd, Edinburgh.

Baer G., Sandwell D., Williams S., Bock Y., Shamir G., 1999, Coseismic deformation associated with the November 1995, Mw=7.1 Nuweiba earthquake, Gulf of Elat (Aqaba), detected by synthetic aperture radar interferometry. *J. Geophys. Res.*, 104, 25221– 25232.

Barazangi, M., Seber, D., Chaimov, T., Best, J. & Sawaf, T., 1993. Tectonic evolution of the northern Arabian plate in western Syria, in: Boschi et. al., (eds.) Recent Evolution and Seimicity of the Mediterranean Region, pp. 117-140, Kluwer Academic Publisher, the Netherlands.

Boncio P. and V. Bracone, (2009), Active stress from earthquake focal mechanisms along the Padan–Adriatic side of the Northern Apennines (Italy), with considerations on stress magnitudes and pore-fluid pressures, Tectonophysics 476 (2009) 180–194, doi:10.1016/j.tecto.2008.09.018.

Brew G., Barazangi M., Al-Maleh A. K., Sawaf T.(2001), Tectonic and geologic evolution of Syria, GeoArabia, Vol. 6, PP 573-616.

Bulletin of the Syrian National Seismological Network (SNSN), 1995-2011, National Earthquake Center, Ministry of Petroleum and mineral resources, Syrian Arab Republic.

Bulut, F., M. Bohnhoff, T. Eken, C. Janssen, T. Kılıç, and G. Dresen (2012), The East Anatolian Fault Zone: Seismotectonic setting and spatiotemporal characteristics of seismicity based on precise earthquake locations, *J. Geophys. Res.*, 117, B07304, doi:10.1029/2011JB008966.

Célérier B., 2010, Remarks on the relationship between the tectonic regime, the rake of the slip vectors, the dip of the nodal planes, and the plunges of the P, B, and T axes of earthquake focal mechanisms, *Tectonophysics* 482 (2010) 42–49.

Dakkak R., Daoud M., Mreish M., Hade G., (2005), The Syrian National Seismological Network (SNSN): Monitoring a major continental transform fault, *Seismological Research Letters*, Vol. 76, PP 437-445.

Frohlich C., 1992, Triangle diagrams: ternary graphs to display similarity and diversity of earthquake focal mechanisms, *Physics of the Earth and Planetary Interiors*, 75 (1992) 193-198.

Garfunkel Z., 2011, The long- and short-term lateral slip and seismicity along the Dead Sea Transform: an interim evaluation. *Isr J Earth Sci*, 58, 217–235.

Heidbach, O., Rajabi, M., Reiter, K., Ziegler, M., & Team, W. S. M. (2016). World stress map database release 2016. GFZ Data Services. https://doi.org/10.5880 /WSM.2016.001

Ibrahim R., Hiroshi T., Daoud M. and Hara T., (2012). 1-D velocity model for Syria from local earthquake data and new seismicity map in syria. *Bulletin of IISEE*, 46, 121-137.

Kartal R. F., Kadirioğlu F. T., Zünbül, S, (2013), Kinematic of east Anatolian fault and Dead sea fault, Conference Paper, October 2013, https://www.researchgate.net /publication/271852091.

Kilb D. and J. L. Hardebeck, (2006), Fault Parameter Constraints Using Relocated Earthquakes: A Validation of First-Motion Focal-Mechanism *Data Bulletin of the Seismological Society of America*, Vol. 96, No. 3, pp. 1140–1158, June 2006, doi: 10.1785/0120040239.

Klinger Y., Rivera L., Haessler H., Maurin J.C., 1999, Active faulting in the Gulf of Aqaba: new knowledge from the Mw7.3 earthquake of 22 November 1995. *Bull. Seismol. Soc. Am.*, 89, 1025– 1036.

Knipper, A.L., Savelyev, A.A., Rukieh, M., 1988. Ophiolitic association of Northwestern Syria. *Geotectonics* 22 (1), 73–82.

McKenzie, D. P. (1969). The relation between fault plane solutions for earthquakes and the directions of the principal stresses. *Bulletin of the Seismological Society of America*, 59(2), 591–601.

Meghraoui M., Gomez F., Sbeinati R., Van der Woerd J., Mouty M., Darkal A. N., Radwan Y., Layyous I., Al-Najjar H., Darawcheh R., Hijazi F. & Barazangi M., (2003), Evidence for 830 years of seismic quiescence from palaeoseismology, archaeo seismology and historical seismicity along the Dead Sea Fault System, *Earth and Planetry Science Letters*, Vol. 210, PP. 35-52.

Müller, B., Zoback, M. L., Fuchs, K., Mastin, L., Gregersen, S., Pavoni, N., *et al.* (1992). Regional patterns of tectonic stress in Europe. *Journal of Geophysical Research*, 97, 11,783–11,803. https://doi.org/10.1029/91JB01096

Palano M., Imprescia P., and Gresta S., 2013, Current stress and strain-rate fields across the Dead Sea Fault System:

Constraints from seismological data and GPS observations. EPSL, 369, 305-316.

Rajabi, M., Tingay, M., Heidbach, O., Hillis, R., & Reynolds, S. (2017). The present-day stress field of Australia. *Earth-Science Reviews*, 168, 165–189. https://doi.org/10.1016/j.earscirev.2017.04.003

Reilinger R., and S. McClusky, 2011, Nubia Arabia Eurasia plate motions and the dynamics of Mediterranean and Middle East tectonics. *Geophys. J. Int.*, 186, 971–979.

Rukieh, M., Trifonov, V. G., Dodonov, A. E., Minini, H., Ammar, O., Ivanova, T. P., Taza, T., Yusef, A., Al-Shara, M., Jobaili, Y., 2005. Neotectonic map of Syria and some aspects of Late Cenozoic evolution of the northwestern boundary zone of the Arabian plate. *Journal of Geodynamics*, 40, 235-256.

Salah M. K., 2019. Seismological Evidence for Lithospheric Low-Velocity Anomalies beneath the Eastern Mediterranean: Impact of Tectonics, *Geotectonics* 53 (5), pp 617-633. https://doi.org/10.1134/S0016852119050054.

Salamon A., Hofstetter, A., Garfunkel Z., Ron H. (2003), Seismotectonics of the Sinai subplate – the eastern Mediterranean region, *Geophys. J. Int.*, Vol. 155, PP 149-173.

Salamon A., Hofstetter A., Garfunkel Z., Ron H., 1996, Seismicity of the eastern Mediterranean region: perspective from the Sinai subplate. *Tectonophysics*, 263, 293–305.

Seisan 10.3, 2015: The earthquake analysis software, Version 10.3, Jens Havskov and Lars Ottemöller, Department of Earth Science, University of Bergen, Allégaten 41, 5007 Bergen, Norway, 2015.

Trifonov V. G. (1991), Levent fault zone in the northwest Syria, *Geotectonics*, Vol. 25, PP 145-154.

Zanchi a., G. B. Crosta, A. N. Darkal, 2002, Paleostress analyses in NW Syria: constraints on the Cenozoic evolution of the northwestern margin of the Arabian plate. *Tectonophysics*, 357, 255–278.

Zoback, M.L., 1992. First- and second-order patterns of stress in the lithosphere: The World Stress Map project. *J. Geophys. Res.*, 97, 11,703-11,728

Zollo A. & Bernard P. (1991), Fault mechanisms from near-source data : joint inversion of S polarization and P polarities, *Geophys. J.Int.*, Vol. 104 PP441-451.